Carnegie Mellon University

CARNEGIE INSTITUTE OF TECHNOLOGY

THESIS

SUBMITTED IN PARTIAL FULFILLMENT OF THE REQUIREMENTS

FOR THE DEGREE OF Doctor of Philosophy

TITLE Single Wall Carbon Nanotube-Protein Complexes and Immune Cells: Uptake, Processing, and Targeted Delivery

PRESENTED BY Patrick Boyer

ACCEPTED BY THE DEPARTMENT OF

Chemical Engineering

KRIS NOEL DAHL

CO-ADVISOR DATE

MOHAMMAD F. ISLAM

CO-ADVISOR DATE

LORENZ BIEGLER

DEPARTMENT HEAD DATE

APPROVED BY THE COLLEGE COUNCIL

VIJAYAKUMAR BHAGAVATULA

DEAN DATE

Single Wall Carbon Nanotube – Protein Complexes and Immune Cells: Uptake, Processing, and Targeted Delivery

Submitted in partial fulfillment of the requirements for

the degree of

Doctor of Philosophy

in

Chemical Engineering

Patrick D. Boyer

B.E., Chemical Engineering, Vanderbilt University

Carnegie Mellon University
Pittsburgh, PA

May, 2015

Acknowledgements

The work comprising this thesis has been a major undertaking and would not be possible without the assistance and support of many extraordinary individuals. First and foremost, I would like to thank my research advisors, Profs. Kris Dahl and Mohammad Islam for their guidance and support, which has enabled the growth of my project and challenged me to develop as a researcher. Additionally, I would like to thank my thesis committee, Profs. Robert Tilton, Kathryn Whitehead, Christopher Bettinger, and Stephen Badylak, for their insightful feedback and discussion on my work from many different perspectives over the years.

I have been fortunate to work with many superb colleagues over the years who, though group meetings and discussions, have helped to shape my perspective and develop my communication of the work. I would like to thank all members of the Dahl and Islam Lab Groups. I would especially like to thank colleagues that I have worked with on the SWCNT-Cell project, Stefanie Baker, Sarah Robb, Alex Short, Dr. Peter Yaron, as well as two talented undergraduate students Gina Lu and Mary Clare McCorry. I am particularly grateful to Dr. Brian Holt for laying the groundwork on the project, thorough equipment training, and our thoughtful scientific discussions.

I would also like to thank the many researchers I have collaborated with outside of Carnegie Mellon who have allowed me to develop the research in new and exciting directions, Prof. Abbe de Vallejo and Josh Michel at Children's

Hospital of Pittsburgh of UPMC, Prof. Mohammad Mofrad and Hengameh Shams at the University of California, Berkeley, and Prof. Stephen Badylak and Dr. Jeremy Kelly at the University of Pittsburgh.

Finally, I would like to sincerely thank all my friends and family who have supported me throughout the years. To Steve Spagnol, John Goldman, and Devin Sullivan: thank you for motivating me to work half as hard on the great weather days, being there when the deadlines got tight, and for the celebrations afterwards.

To my parents David and Diane and my sister Lindsay: thank you for encouraging my relentless pursuit of all things science, from C-MITES to wearing a tam. The work ethic and perseverance instilled in me when I was younger was used every step of the way.

To Sarah Feicht: thank you for unwavering support and believing in me which has given me the confidence to strive towards my goals.

Financial Support:

This research was supported by the Neil and Jo Bushnell Fellowship in Engineering, awarded to Patrick D. Boyer; the National Science Foundation under grant numbers CBET-0708418 and DMR-0619424, awarded to Kris Noel Dahl and Mohammad F. Islam, grant numbers CBET-0954421 and CMMI-1300476, awarded to Kris Noel Dahl, and grant numbers CMMI-1335417 and DMR-0645596, awarded to Mohammad F. Islam; and The Sloan Foundation, awarded to Mohammad F. Islam.

Doctoral Committee:

Kris Noel Dahl, Ph.D., Committee Co-Chair, Associate Professor of Chemical Engineering and Biomedical Engineering, Carnegie Mellon University

Mohammad F. Islam, Ph.D., Committee Co-Chair, Associate Research Professor of Materials Science and Engineering, Carnegie Mellon University

Robert D. Tilton, Ph.D., Professor of Chemical Engineering and Biomedical Engineering, Carnegie Mellon University

Kathryn A. Whitehead, Ph.D., Assistant Professor of Chemical Engineering, Carnegie Mellon University

Christopher J. Bettinger, Ph.D., Assistant Professor of Biomedical Engineering and Materials Science and Engineering, Carnegie Mellon University

Stephen F. Badylak, D.V.M., M.D., Ph.D., Professor of Surgery, University of Pittsburgh

Abstract

The immune system is composed of a network of cells that are precisely regulated to protect the body from infection. Abnormal activity of this cellular network can result in numerous diseases and disorders including chronic inflammation, rheumatoid arthritis, atherosclerosis, and cancer. Modulation of immune cells *via* the targeted delivery of immunologically active compounds has the potential to redirect the immune response and restore health.

The unique nanostructure and properties of single wall carbon nanotubes (SWCNTs) are well-suited for cellular applications particularly in the manipulation of immune cell function. SWCNTs must be properly functionalized to maintain their inherent properties and to provide control over their uptake, processing, and delivery. This thesis focuses on understanding the macrophage cellular response to SWCNT-protein complexes and engineering the SWCNT-protein complex interface to build new functionalities that preserve inherent SWCNT properties while enabling targeting and delivery applications.

Kinetic parameters governing the uptake of SWCNT-protein complexes in macrophages are determined using Raman spectroscopy. The cellular inflammatory activity level is found to contribute more to uptake than different SWCNT interfaces. The subcellular concentrations and distribution of SWCNT-protein complexes processed by macrophages are revealed in the context of aggregation state. Short SWCNTs-protein complexes are found to be concentrated

in highly bundled regions, whereas long SWCNTs-protein complexes and SWCNTs in fibroblasts were not.

Protein structure is further engineered to direct the subcellular localization of SWCNT-protein complexes in cells. A native cellular protein is engineered with a favorable structure for SWCNT dispersion and an exposed nuclear localization sequence for subcellular targeting to the nucleus. Finally, non-covalent SWCNT-protein interactions are tuned to enable SWCNT loading and delivery of molecules within cells. Delivery is achieved with chemotherapeutic and immunosuppressive drugs resulting in enhanced anti-proliferative and anti-inflammatory effects compared to non-complexed drugs.

The scientific discoveries reveal important information about macrophage uptake and processing of SWCNTs that may be used to probe cell behavior or develop delivery approaches for therapeutic applications. The strategies developed to create excellent SWCNT dispersions with tailored functionalities through protein modifications may be used generally by other researchers to initiate new ways to modulate cellular response with nanomaterials.

Table of Contents

List of Figures

1 Introduction

The immune system is composed of a complex and vital network of tissues, cells, and molecules that are precisely regulated to protect the body from infection and disease.[1] Abnormal activity of this cellular network can result in chronic inflammation which contributes significantly to the pathogenesis of numerous diseases and disorders including rheumatoid arthritis, multiple sclerosis, inflammatory bowel disease, diabetes, atherosclerosis, and cancer.[2] Macrophages are an important cellular component of inflammatory diseases. In cancer, for instance, inflammation promotes the recruitment of tumor associated macrophages which stimulate angiogenesis and enable tumor growth.[3] In rheumatoid arthritis, macrophages are fixed in an inflammatory phenotype releasing pro-inflammatory cytokines that perpetuate T-cell activation and destruction of healthy tissue.[4-5] On the other hand, healthy physiological processes, such as macrophage-mediated wound healing and subsequent tissue remodeling, involve controlled transitions between inflammatory and anti-inflammatory phenotypes.[6-7] Studies show the phenotype of macrophages can be reprogrammed *in situ*, suggesting that modulation of immune cells *via* targeted delivery of immunologically active compounds has the potential to redirect the immune response and restore health.[8]

Engineered nanomaterials based therapies that can directly interact with immune cells are highly desirable and currently of great interest to modulate, regulate, and monitor immune cell function in pathological disease states as well

as physiological processes.[9] Single wall carbon nanotubes (SWCNTs) are a recently discovered class of nanostructured material[10] that has flooded the application scene across diverse scientific fields due to their exceptional electrical,[11] optical,[12] mechanical,[13] and thermal[14] properties. SWCNTs fill many basic nanoparticle design qualities for biomedical applications including chemical stability, small size, large surface area, and high cell uptake. SWCNTs possess extremely large surface area-to-volume ratio allowing for substantial functionalization, which can be leveraged for multimodal targeting and molecular loading.[15-16] The distinct nanostructure of SWCNTs results in several inherent imaging modalities including unique Raman scattering modes[17-18] and near-infrared (NIR) fluorescence[12, 19] which can be used to identify SWCNTs without interference from tissues and cells. Further, the sensitivity of SWCNT optical properties to their local environment can be utilized for molecular sensing.[20] The strong optical absorbance of SWCNTs in the NIR combined with their high thermal conductivity can induce significant local heating and may be used to photothermally ablate cells.[21]

The delivery of SWCNTs to immune cells, including macrophages, has tremendous potential for probing and modulating cell function for diagnosis and development of therapies related to inflammation, cancer, and regenerative medicine. The unique optical properties of SWCNTs may be leveraged to label immune cells[19] to visualize pathological regions with large numbers of immune cells or to sense intracellular activation during inflammatory response.[22] The physical properties of SWCNTs promote cell internalization and high molecular

loading, enabling their use as efficient delivery vectors for cytokines or drugs to reprogram local immune cell phenotype and inhibit detrimental immune responses.[23]

SWCNTs are naturally hydrophobic and must be dispersed in water for biomedical applications. Hydrophilic moieties may be attached to the SWCNT surface to promote solubility and stability in aqueous environments through non-covalent or covalent functionalization.[15] Non-covalent approaches are preferred to covalent chemistries which alter inherent SWCNT properties.[24] Thus, the choice of a non-covalent dispersing agent is crucial to maintain SWCNT properties, confer stability, direct interaction with cells, and promote subcellular delivery applications.[25] Non-covalent functionalization of SWCNTs with copolymers,[19] lipids,[26] polysaccharides,[27] and DNA[28] has been used to impart biocompatibility and maintain SWCNT properties. However, these dispersing agents do not promote interactions with cells, nor do they contain inherent functionalities required for specific cellular and subcellular applications.

To impart biofunctionality necessary for delivery applications with immune cells, we consider surfactant-like proteins with structures well-suited for individually dispersing SWCNTs and associating with other biomolecules. Globular albumin proteins produce high yield dispersions of individual SWCNTs with stability in high ionic strength biological solutions.[29] Proteins also cloak SWCNTs with a biological surface facilitating increased biocompatibility and interaction with cells. Further, globular albumin proteins contain internal hydrophobic regions that bind fatty acids and other hydrophobic molecules,

including many drugs.[30-31] We find purified and well-dispersed SWCNTs-protein complexes enter cells by the millions without acute toxicity.[29, 32-33]

However, there remains limited mechanistic understanding of how SWCNT-protein complexes interact with a complex, dynamic cellular state, such as those found in inflammatory immune cells. To engineer effective dispersions for cellular delivery, it is necessary to understand the contributions of protein bioactivity and inflammatory cell activity to SWCNT uptake in macrophages. Insight into the subcellular processing, distribution, and interactions of SWCNT-protein complexes in cells is also critical for designing specific SWCNT-protein complex functionalities for subcellular applications aimed at modulating cell function including subcellular targeting and delivery of bioactive molecules. Thus, the first major focus of this thesis is to determine the role of non-covalent protein functionalization on mechanisms of cellular uptake and processing of SWCNT-protein complexes. The second major focus is the development of multifunctional non-covalent protein dispersions of SWCNTs that preserve inherent SWCNT properties while enabling subcellular targeting and drug delivery within cells through specific protein structure features and cellular processing of SWCNT-protein complexes.

1.1 Thesis Objectives

1.1.1 Determine the effects of SWCNT-protein bioactivity and cell inflammatory activity on SWCNT uptake in macrophages.

Developing a quantitative understanding of SWCNT uptake mechanisms in macrophages is important for tuning macrophage specific delivery for therapeutic applications. In Chapter 3, we quantify the uptake of SWCNTs in macrophages at various exposure concentrations to establish intracellular SWCNT concentration as well as elucidate the key tunable parameters for controlling cellular delivery. To determine the role of surface coating bioactivity in SWCNT uptake, we compared non-covalent bioinert SWCNT-polymer and bioactive SWCNT-protein complexes. We also compared SWCNT uptake in non-inflammatory and inflammatory macrophage phenotypes to determine the role of cell activity in SWCNT uptake. Using Raman spectroscopy, the uptake of SWCNTs is precisely determined, and physical models of the data are generated to extract uptake parameters. We test the hypothesis that the biological nature of protein and the inflammatory response of cells will increase SWCNT uptake.

1.1.2 Establish subcellular distribution and cellular processing of SWCNT-protein complexes in macrophages.

In Chapter 4, we build on the previous cellular level analysis to develop insight into the subcellular underpinnings controlling the processing of internalized SWCNT-protein complexes. Understanding the intracellular

distribution of SWCNTs is important for controlling the rates of accumulation and delivery to specific subcellular compartments, which have direct impacts on toxicity and therapy. Using Raman spectroscopy to quantify and characterize SWCNT-protein complexes within cells, local subcellular concentrations are determined and spatially correlated to measures of SWCNT dispersion state (individual or bundled). For macrophages with size dependent uptake mechanisms, the lengths of SWCNTs are varied to examine the cellular processing resulting from different SWCNT internalization processes. Subcellular processing of SWCNT-protein complexes in macrophages is also compared to other non-immune cell types. We test the hypothesis that distinct highly concentrated subcellular regions of SWCNTs in macrophages arise from bundling of SWCNT-protein complexes.

1.1.3 Engineer protein structure to direct the subcellular localization of SWCNT-protein complexes.

After determining the uptake and cellular processing of non-specific SWCNT-protein complexes, we engineer a low molecular weight globular protein through recombinant protein expression for non-covalent SWCNT dispersion and specific subcellular function in Chapter 5. The protein has a central hydrophobic core for SWCNT association and stabilization as well as an exposed nuclear localization sequence to promote active nuclear import and subcellular targeting. We track the subcellular localization of engineered SWCNT-protein complexes in

cells over time relative to non-specific SWCNT-protein complexes using a combination of Raman spectroscopy, SWCNT NIR fluorescence imaging, and fluorescence lifetime imaging microscopy. We test the hypothesis that the engineered protein possesses a macromolecular structure appropriate to stably disperse and target SWCNTs subcellularly.

1.1.4 Utilize protein structure to load and deliver molecules within cells using SWCNT-protein complexes.

A major barrier to effective immunotherapy is the ability to precisely control intracellular delivery of drugs with broad effects for the prevention of adverse off-target and systemic responses. In Chapter 6, we explore the structural functionality of albumin proteins to bind hydrophobic molecules, including many drugs, to develop multifunctional non-covalent SWCNT-protein-molecule ternary complexes for controlled drug delivery. Molecular docking studies are performed to reveal the binding sites for SWCNTs and molecules within the protein. We quantify the delivery and intracellular release of loaded fluorophore molecules using SWCNT-protein-molecule ternary complexes with a combination of visible and NIR fluorescence imaging and fluorescence lifetime imaging microscopy. Anti-cancer drugs and immunosuppressant corticosteroids are substituted for the fluorophore and measures of anti-proliferative and anti-inflammatory effects are quantified for the SWCNT-protein-drug ternary systems, relative to non-complexed drugs. We test several hypotheses: proteins can non-covalently load

molecules onto SWCNTs resulting in stable dispersions; SWCNT-protein-molecule ternary complexes increase the intracellular delivery of loaded molecules; molecules release from SWCNTs *in vitro* and intracellularly as a result of enzymatic disruption of the SWCNT-protein complex; and fluorophore studies translate to bioactive molecules with cellular response.

1.2 References

1. Murray, P. J.; Wynn, T. A. Protective and pathogenic functions of macrophage subsets. *Nature Reviews Immunology* **2011,** *11*, 723-737.

2. Nathan, C.; Ding, A. Nonresolving Inflammation. *Cell* **2010,** *140*, 871-882.

3. Mantovani, A.; Sozzani, S.; Locati, M.; Allavena, P.; Sica, A. Macrophage polarization: tumor-associated macrophages as a paradigm for polarized M2 mononuclear phagocytes. *Trends in Immunology* **2002,** *23*, 549-555.

4. Choy, E. H. S.; Panayi, G. S. Cytokine Pathways and Joint Inflammation in Rheumatoid Arthritis. *New England Journal of Medicine* **2001,** *344*, 907-916.

5. Firestein, G. S. Evolving concepts of rheumatoid arthritis. *Nature* **2003,** *423*, 356-361.

6. Brown, B. N.; Ratner, B. D.; Goodman, S. B.; Amar, S.; Badylak, S. F. Macrophage polarization: An opportunity for improved outcomes in biomaterials and regenerative medicine. *Biomaterials* **2012,** *33*, 3792-3802.

7. Stout, R. D.; Jiang, C.; Matta, B.; Tietzel, I.; Watkins, S. K.; Suttles, J. Macrophages Sequentially Change Their Functional Phenotype in Response to Changes in Microenvironmental Influences. *The Journal of Immunology* **2005,** *175*, 342-349.

8. Stout, R. D.; Watkins, S. K.; Suttles, J. Functional plasticity of macrophages: in situ reprogramming of tumor-associated macrophages. *Journal of Leukocyte Biology* **2009,** *86*, 1105-1109.

9. Goldberg, M.; Langer, R.; Jia, X. Nanostructured materials for applications in drug delivery and tissue engineering. *Journal of Biomaterials Science, Polymer Edition* **2007,** *18*, 241-268.

10. Iijima, S. Helical microtubules of graphitic carbon. *Nature* **1991,** *354*, 56-58.

11. Thess, A.; Lee, R.; Nikolaev, P.; Dai, H.; Petit, P.; Robert, J.; Xu, C.; Lee, Y. H.; Kim, S. G.; Rinzler, A. G.; Colbert, D. T.; Scuseria, G. E.; Tománek, D.; Fischer, J. E.; Smalley, R. E. Crystalline Ropes of Metallic Carbon Nanotubes. *Science* **1996,** *273*, 483-487.

12. O'Connell, M. J.; Bachilo, S. M.; Huffman, C. B.; Moore, V. C.; Strano, M. S.; Haroz, E. H.; Rialon, K. L.; Boul, P. J.; Noon, W. H.; Kittrell, C.; Ma, J.; Hauge, R. H.; Weisman, R. B.; Smalley, R. E. Band Gap Fluorescence from Individual Single-Walled Carbon Nanotubes. *Science* **2002,** *297*, 593-596.

13. Treacy, M. M. J.; Ebbesen, T. W.; Gibson, J. M. Exceptionally high Young's modulus observed for individual carbon nanotubes. *Nature* **1996,** *381*, 678-680.

14. Berber, S.; Kwon, Y.-K.; Tománek, D. Unusually High Thermal Conductivity of Carbon Nanotubes. *Physical Review Letters* **2000,** *84*, 4613-4616.

15. Battigelli, A.; Ménard-Moyon, C.; Da Ros, T.; Prato, M.; Bianco, A. Endowing carbon nanotubes with biological and biomedical properties by chemical modifications. *Advanced Drug Delivery Reviews* **2013,** *65*, 1899-1920.

16. Wong, B. S.; Yoong, S. L.; Jagusiak, A.; Panczyk, T.; Ho, H. K.; Ang, W. H.; Pastorin, G. Carbon nanotubes for delivery of small molecule drugs. *Advanced Drug Delivery Reviews* **2013,** *65*, 1964-2015.

17. Dresselhaus, M. S.; Dresselhaus, G.; Saito, R.; Jorio, A. Raman spectroscopy of carbon nanotubes. *Physics Reports* **2005,** *409*, 47-99.

18. Kang, J. W.; Nguyen, F. T.; Lue, N.; Dasari, R. R.; Heller, D. A. Measuring Uptake Dynamics of Multiple Identifiable Carbon Nanotube Species via High-Speed Confocal Raman Imaging of Live Cells. *Nano Letters* **2012,** *12*, 6170-6174.

19. Cherukuri, P.; Bachilo, S. M.; Litovsky, S. H.; Weisman, R. B. Near-Infrared Fluorescence Microscopy of Single-Walled Carbon Nanotubes in Phagocytic Cells. *Journal of the American Chemical Society* **2004,** *126*, 15638-15639.

20. Kruss, S.; Hilmer, A. J.; Zhang, J.; Reuel, N. F.; Mu, B.; Strano, M. S. Carbon nanotubes as optical biomedical sensors. *Advanced Drug Delivery Reviews* **2013,** *65*, 1933-1950.

21. Kosuge, H.; Sherlock, S. P.; Kitagawa, T.; Dash, R.; Robinson, J. T.; Dai, H.; McConnell, M. V. Near Infrared Imaging and Photothermal Ablation of Vascular Inflammation Using Single-Walled Carbon Nanotubes. *Journal of the American Heart Association* **2012,** *1*.

22. Kim, J.-H.; Heller, D. A.; Jin, H.; Barone, P. W.; Song, C.; Zhang, J.; Trudel, L. J.; Wogan, G. N.; Tannenbaum, S. R.; Strano, M. S. The rational design of nitric oxide selectivity in single-walled carbon nanotube near-infrared fluorescence sensors for biological detection. *Nature Chemistry* **2009,** *1*, 473-481.

23. Smith, D. M.; Simon, J. K.; Baker Jr, J. R. Applications of nanotechnology for immunology. *Nature Reviews Immunology* **2013,** *13*, 592-605.

24. Bekyarova, E.; Sarkar, S.; Wang, F.; Itkis, M. E.; Kalinina, I.; Tian, X.; Haddon, R. C. Effect of Covalent Chemistry on the Electronic Structure and Properties of Carbon Nanotubes and Graphene. *Accounts of Chemical Research* **2012,** *46*, 65-76.

25. Holt, B. D.; McCorry, M. C.; Boyer, P. D.; Dahl, K. N.; Islam, M. F. Not all protein-mediated single-wall carbon nanotube dispersions are equally bioactive. *Nanoscale* **2012,** *4*, 7425-7434.

26. Kam, N. W. S.; O'Connell, M.; Wisdom, J. A.; Dai, H. Carbon nanotubes as multifunctional biological transporters and near-infrared agents for selective cancer cell destruction. *Proceedings of the National Academy of Sciences of the United States of America* **2005,** *102*, 11600-11605.

27. Bandyopadhyaya, R.; Nativ-Roth, E.; Regev, O.; Yerushalmi-Rozen, R. Stabilization of Individual Carbon Nanotubes in Aqueous Solutions. *Nano Letters* **2002,** *2*, 25-28.

28. Jin, H.; Heller, D. A.; Sharma, R.; Strano, M. S. Size-Dependent Cellular Uptake and Expulsion of Single-Walled Carbon Nanotubes: Single Particle Tracking and a Generic Uptake Model for Nanoparticles. *ACS Nano* **2009,** *3*, 149-158.

29. Holt, B. D.; Dahl, K. N.; Islam, M. F. Quantification of Uptake and Localization of Bovine Serum Albumin-Stabilized Single-Wall Carbon Nanotubes in Different Human Cell Types. *Small* **2011,** *7*, 2348-2355.

30. Ghuman, J.; Zunszain, P. A.; Petitpas, I.; Bhattacharya, A. A.; Otagiri, M.; Curry, S. Structural Basis of the Drug-binding Specificity of Human Serum Albumin. *Journal of Molecular Biology* **2005,** *353*, 38-52.

31. He, X. M.; Carter, D. C. Atomic structure and chemistry of human serum albumin. *Nature* **1992,** *358*, 209-215.

32. Boyer, P. D.; Holt, B. D.; Islam, M. F.; Dahl, K. N. Decoding membrane- versus receptor-mediated delivery of single-walled carbon nanotubes into macrophages using modifications of nanotube surface coatings and cell activity. *Soft Matter* **2013,** *9*, 758-764.

33. Holt, B. D.; Dahl, K. N.; Islam, M. F. Cells Take up and Recover from Protein-Stabilized Single-Wall Carbon Nanotubes with Two Distinct Rates. *ACS Nano* **2012,** *6*, 3481-3490.

2 Background

2.1 SWCNT Structure and Properties

Single wall carbon nanotubes (SWCNTs) are a recently discovered class of nanostructured material with unique chemical and physical characteristics.[1] The atomic arrangement of covalent bonded carbon atoms in SWCNTs results in inherent electrical,[2] optical,[3] thermal,[4] and mechanical[5] properties that have motivated diverse interest in research fields from energy to medicine. Pristine SWCNTs are composed entirely of sp^2-hybridized carbon atoms resulting in structures that are chemically inert, even within the cellular environment. SWCNTs may be conceptualized as a sheet of graphene rolled into a seamless cylinder with closed ends. The angle at which the graphene sheet is rolled imparts chirality to the SWCNT. Thus, unique SWCNT species with different chiralites are given by a pair of indices (n,m) defined by the number of unit vectors ($n\mathbf{a_1}$,$m\mathbf{a_2}$) along the hexagonal lattice contained in the chiral vector ($\mathbf{C_h}$). The particular chirality of SWCNTs affects the electronic character (*i.e.*, n – m = 3j, where j is an integer are metals; the rest are semiconductors with varying gap sizes).

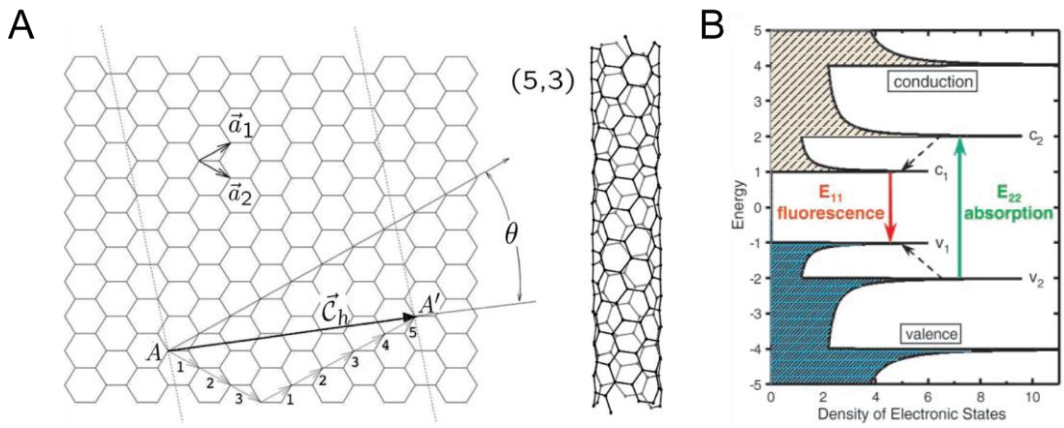

Figure 2.1: SWCNT nomenclature and electronic structure. (A) The chiral vector $\mathbf{C_h} = 5\mathbf{a_1} + 3\mathbf{a_2}$ represents one way the two-dimensional graphene sheet many be rolled into a tube. Lattice vectors $\mathbf{a_1}$ and $\mathbf{a_2}$, shown for the (5,3) nanotube.[6] (B) Density of electronic states of a semiconducting SWCNT. The van Hove singularities arise due to quantum confinement.[7]

SWCNTs have diameters between ~0.7 – 2 nm and lengths ranging from tens of nanometers to microns placing them on a similar size scale as many bio-macromolecules.[8] The ratio of SWCNT length to diameter contributes to large aspect ratios, while their small size gives high surface area-to-volume ratios resulting in a large amount of surface sites for highly specific functionalization compared to similar-sized nanomaterials. SWCNTs also have exceptional mechanical and thermal properties including a Young's modulus over 1 TPa,[5] a persistence length between 26 – 138 μm,[9] and thermal conductivity ~3000 W/mK.[4]

The one-dimensional structure of SWCNTs gives rise to van Hove singularities in the nanotube density of states.[10] At energies associated with the van Hove singularities, sharp transitions between valence and conduction bands result in distinct peaks in optical absorption and fluorescence spectra. The

sharpness of peaks in the optical absorbance of SWCNTs provides a qualitative indicator of dispersion quality.[3] Individually dispersed, semiconducting SWCNTs excited in the visible range exhibit fluorescence in the NIR spectrum (800 – 1600 nm).[3] SWCNTs emit fluorescence at distinct wavelengths in the NIR corresponding to their electronic band-gap set by the van Hove singularities.[7] The excited state is excitonic rather than electronic. SWCNT fluorescence can be quenched by bundles of SWCNTs, which contain metallic SWCNTs.[3] The NIR fluorescence of SWCNTs is also length dependent[11] as fluorescence is quenched by exciton diffusion to quenching sites consisting of SWCNT end caps, sp^3-hybridized defects, and doping.[12-13]

SWCNTs have strong resonance enhanced Raman active vibrational modes resulting in a unique Raman signature that can be utilized to characterize and quantify the presence of SWCNTs.[14] A Raman spectrum results from the partial absorption of incident light due to interactions with surface vibrations. SWCNT Raman signature allows for the imaging of all SWCNTs (metallic and semiconducting) regardless of dispersion status. The radial breathing mode (RBM) features appearing at 100 – 300 cm^{-1} are unique to carbon nanotubes and correspond to atomic vibrations of carbon atoms in the radial direction.[14] RBM signal > 250 cm^{-1} has been associated with van der Waals contact and can be used to infer aggregation or bundling of SWCNTs.[15-16] The tangential mode for graphene, or G-band, appearing at ~1590 cm^{-1} corresponds to atomic displacements along the tube axis and along the circumferential direction. The G-band is quantitative for the amount of sp^2-hybridized carbon in the sample and

can be used to determine the concentration of SWCNTs with the aid of a standard curve. Finally, the disorder mode, or D-band, found at ~1300 cm^{-1} indicates the presence of sp^3 carbon defects. Therefore, the D-band to G-band intensity ratio can be used to determine the structural quality of SWCNTs.

2.2 SWCNT Purification and Length Fractionation

SWCNTs can be produced through several different synthesis methods including pulsed laser deposition, electric arc discharge, catalytic decomposition, and chemical vapor deposition.[17-20] Essentially, all methods involve the conversion of carbon precursors to SWCNTs in the presence of catalyst. While there are subtle differences in the distribution of chiralities and diameters produced, the main impact on cellular systems are the impurities produced including residual metal catalysts (*e.g.*, Fe, Ni, Y, Co) and non-SWCNT carbon phases (*e.g.*, fullerenes, multi-wall carbon nanotubes, and amorphous carbon). Commercial vender purification leaves substantial quantities of residual amorphous carbon and residual metals, much of which is still bioavailable.[21] The presence of toxic metals can result in non-SWCNT induced oxidative stress and other inaccurate toxicity assessments.[22] Further, impurities lower the mass fraction of SWCNT in a prepared sample. To avoid uncertainties introduced by SWCNT synthesis impurities, we highly purified our SWCNTs. RAW high pressure carbon monoxide conversion synthesis (HiPCO) SWCNTs were purified by wet air burn, acid treatment, annealing, and magnetic fractionation.[23-24]

Thermogravimetric analysis and wide-angle X-ray scattering confirmed that the purified sample contained < 5 wt% carbonaceous impurities and ~0.3 wt% metallic impurities, with the rest of the sample being unaltered SWCNTs.[23-24]

SWCNT synthesis also produces samples with varying lengths which can range from tens of nanometers to several microns. For cellular experiments, we performed length fractionation to select SWCNTs with lengths ~145 ± 17 nm which have been shown to promote endocytosis-mediated uptake into cells.[25] Purified SWCNTs were dispersed in water using sodium deoxycholate (DOC) and centrifuged at 21,000×*g* for 2 h to remove remaining SWCNT bundles.[26-27] Individualized SWCNTs were length fractionated using density gradient ultracentrifugation.[28] SWCNTs in the 10^{th}-12^{th} fractions with lengths of 145 ± 17 nm were collected[25] and subsequently pelleted and burned at 300 °C in wet air in the presence of H_2O_2 to remove DOC and then washed in water several times.

2.3 SWCNT Dispersions

SWCNTs are hydrophobic materials that readily aggregate in aqueous environments due to significant van der Waals forces of ~40 kT/nm[29-30] forming large bundles or rope-like structures which are known to diminish their inherent properties.[3, 30] Specifically in a biological context, large bundles of SWCNTs have been associated with a number of deleterious cellular effects, such as changes in focal adhesions, cell shape, proliferation, and differentiation.[31] Thus, for biomedical applications including cellular delivery, SWCNTs need to be

stably dispersed in solution. SWCNTs can be dispersed in solution by covalent or non-covalent functionalization of the hydrophobic surface with water soluble moieties. Chemical modification of the SWCNT sidewall through covalent functionalization changes the bond structure of the carbon backbone and alters intrinsic SWCNT properties desired for biomedical applications.[32] Non-covalent functionalization relies on the hydrophobic domains of amphilphilic molecules, such as surfactants, polymers, or biomolecules, which interact with the hydrophobic SWCNT surface. Functionalization with traditional surfactants such as sodium dodecyl sulfate and sodium dodecylbenzene sulfonate produce excellent dispersions that maintain SWCNT properties,[26] but destroy cell membranes.[33] Biocompatible non-covalent SWCNT dispersions have been created using surfactant-like copolymers,[34-39] lipids,[40-41], peptides,[42-43] DNA,[44] enzymes,[45-46] and proteins.[39, 47-57] Antibodies, RGD peptides, folic acid, and other targeting molecules have since been covalently added to basic non-covalent dispersions creating multi-component systems to target overexpressed receptors on specific types of cells and to promote specific types of endocytic entry.[40, 58-61] Well-dispersed individual SWCNTs can be used in cellular applications without acute toxicity.[36]

Another important consideration for SWCNT dispersions is stability, particularly in the high ionic strength and complex protein environment of cell culture media or even the bloodstream. Dispersions using the protein lysozyme were high quality in water, but flocculated rapidly in cell culture media.[55] Studies have shown displacement of copolymer coating and exchange with serum proteins

in animals.[57] Other work indicates that proteins on the surface of SWCNTs exchange rapidly with free proteins in the bulk.[62]

2.4 SWCNT Properties Leveraged for Biomedical Applications

Individual SWCNTs have been used as NIR fluorophore labels for cells and widely utilized in a variety of imaging applications. Imaging in the NIR spectrum offers high optical transparency and low autofluorescence from biological tissue, allowing for greater penetration depth and higher contrast images.[63] SWCNTs have several other advantages over typical organic fluorophores including no photobleaching,[64] reduced ROS mediated cell toxicity, and large Stokes shift.[65] SWCNT NIR fluorescence has been used to image individual cells,[34] blood vessels in mice,[66] quantify SWCNT concentration in blood over time,[57] and to image tumors. [67] However, while NIR fluorescence has generated much interested on the imaging and detection front, clinical translations is unlike with penetration depths limited to ~1 cm by tissue absorbance and scattering limiting applications to animals. [68]

Along the same lines, SWCNT optical properties have also been developed as sensors as SWCNT NIR fluorescence is highly sensitive to the immediate surrounding environment. Perturbations in NIR fluorescence have been used to detect DNA polymorphism,[69] glucose with implantable sensors,[70] nitric oxide in cells,[71] and many others.[72]

SWCNTs have a large available surface area for functionalization. This has been engineered to deliver a wide variety of cargos into cells through both covalent and non-covalent interactions. Biomacromolecules including DNA,[73-75] small interfering RNA (siRNA),[76-78] and proteins[79-80] have all been transported into cells via SWCNTs. Small molecule drugs including doxorubicin[81] and paclitaxel[82] have been loaded onto SWCNTs through non-covalent π-stacking or cleavable linkages for intracellular delivery and release.[83]

SWCNT thermal properties are currently under investigation for cancer cell hyperthermia. Strong optical absorbance of SWCNTs in the NIR results in molecular vibration energies which can induce significant local heating to cells.[40] Most biological tissue chromophores exhibit low NIR absorbance, thus preventing heat induced damage where SWCNTs are absent.[84] SWCNTs have been used to induce selective photothermal heating and toxicity towards cancer and tumor cells[85-89] and inflammatory macrophages.[90]

2.5 Immune Cells and Inflammation

The immune system contains a diverse group of cells with specialized functions, collectively aimed at maintaining tissue homeostasis. Professional phagocytes such as neutrophils, monocytes, macrophages, and dendritic cells have important functions in the innate immune response and are largely responsible for the ingestion of microorganisms, foreign particles, and dead cells. Cells ingest recognized targets through phagocytosis and subsequently engage in destruction

of the identified pathogen. Neutrophils and monocytes circulate the bloodstream until they are recruited into tissues to respond to inflammation, whereas most macrophages and dendritic cells reside in tissues.

Monocytes comprise a small percentage of circulating white blood cells at just ~5 – 10%, however, they are capable of further differentiation in tissues to macrophages, and other specialized cells such as dendritic cells and osteoclasts.[91] Monocytes circulate the bloodstream for a few days before migrating into tissue to replace resident macrophages. Prior to this natural process, circulating monocytes can be actively recruited to sites of inflammation in the presence of cytokines. Upon migration into tissue and exposure to the inflammatory environment, monocytes typically differentiate into macrophages with enhanced pro-inflammatory activity.[91]

Large populations of macrophages are maintained in tissues, primarily in tissues such as the liver and spleen, as well as other areas prone to infection. While all tissue associated macrophages arise from monocytes in the blood, they typically exist in an immuno-regulatory state until a foreign body invades the tissue. They are the first cells to encounter pathogens in tissues and are responsible the secretion of signaling molecules that alert and recruit neutrophils and monocytes from the bloodstream.

2.6 Uptake Mechanisms in Phagocytes

Neutrophils, monocytes, macrophages, and dendritic cells are capable of a specialized form of uptake known as phagocytosis, in addition to traditional endocytosis pathways.[92-93] Phagocytosis is a multi-step, actin-driven process initiated by particle recognition.[94] Immune cells and macrophages are equipped with a myriad of surface receptors to bind particles directly or indirectly through adsorbed complement proteins. The best studied phagocytic receptors are Fcγ receptors and complement receptors. While Fcγ and complement receptors are thought to bind conserved sequences, other receptors such as scavenger receptors have been reported to bind less specifically. Phagocytosis is a process triggered for the ingestion of larger particles where binding to the phagocyte surface initiates the extension of pseudopods to engulf the particle. Macrophages are also capable of less specific uptake via membrane ruffling in a process referred to as macropinocytosis. Macropinocytosis is a process for the ingestion of larger membrane associated particles and solutes which is accomplished by ingesting parts of the cell membrane and the surrounding fluid. Unlike phagocytosis, which requires a binding event, macropinocytosis occurs continuously. In fact, a macrophage ingests the equivalent of its entire plasma membrane in about a half hour.[95]

2.7 Delivery of Nanomaterials to Immune Cells

Physiochemical properties of synthesized nanomaterials including size, shape, and charge can have large impacts on delivery into cells.[96] Local particle shape has been reported to dictate whether macrophages will engage in phagocytosis of the particle or spreading along the particle surface.[97] Opsonization of nanomaterials with serum proteins can influence the mechanism and efficiency of delivery to phagocytes through surface receptor interactions.[98] Charged particles have been reported to increase phagocytosis, presumably as the result of nonspecific interactions with cells,[99] while coating the particle surface with neutrally charged molecules, such as polyethylene glycol (PEG) helps to avoid macrophage recognition and reduces protein adsorption.[100] In direct comparison, immune cells and macrophages show increased nanoparticle uptake efficiency over epithelial, astrocytes, and endothelial cells.[101]

A wide variety of nanoparticles with inherent imaging properties such as gold nanoparticles, iron oxide nanocrystals, and quantum dots have been targeted to immune cells for medical diagnostic applications.[102] using anionic surface charge,[103] peptides,[104] and monoclonal antibodies.[105] Interesting, the attachment of simple glycine molecules has been demonstrated to increase the selectivity of modified iron oxide nanoparticles for activated macrophages from a library of modifications.[106] The delivery of nanovehicles carrying drugs and imaging agents such as polymeric nanoparticles and liposomes to immune cells has also been widely investigated.[102] Anionic liposomes have been used to target to macrophage scavenger receptors, while incorporation of peptides, mannose, and

immunoglobulins into the structures have resulted in increased macrophage delivery *via* integrins, lectin receptors, and Fcγ receptors, respectively.[107]

2.8 Delivery of SWCNTs to Immune Cells

Primary immune cells and model macrophage cell lines have been routinely exposed to SWCNTs to investigate mechanisms of toxicity[108] and immune cell response.[109] Intracellular delivery of SWCNTs to the cytoplasm of human monocyte derived macrophages has been directly observed *in vitro* using transmission electron microscopy.[110] Pluronic F108 functionalized SWCNTs[34], BSA functionalized SWCNTs,[111] and DNA-wrapped SWCNT-iron oxide complexes[112] have been delivered to model macrophage cell lines for imaging applications.

Targeted delivery of SWCNTs to immune cells has been reported through the use of various covalent chemical modifications. Delivery of multi-wall CNTs (MWCNTs) with small molecule chemical modifications has been reported to target SWCNTs to specific macrophage surface receptors, inducing different downstream immune response.[113] SWCNTs covalently modified with phosphatidylserine were found to increase delivery to immune cells including human monocyte derived macrophages, dendritic cells, and rat brain microglia.[41] SWCNTs used in this study were also reported to deliver apoptosis inducing cytochrome c to immune cells. In other work, SWCNT delivery to human neutrophils was increased by covalent chemical attachment of immunoglobulin

G.[114] Interestingly both human neutrophils and macrophages were observed to digest pre-oxidatively functionalized SWCNTs.[114-115]

2.9 Immune Cell Modulation

Different types of nanoparticles including SWCNTs have been investigated for the potential to interact directly with immune cells to stimulate or suppress cellular response. A polymer-nanotube composite was used to efficiently expand T-cells *in vitro* for immunotherapy.[116] Oxidized MWCNTs were found to up regulate acute inflammatory pathways in monocytes but not T-cells acting as a specific immunostimulators.[117] The most common use of SWCNTs has been for delivery of antigenic molecules to dendritic cells for vaccine production.[118-122]

2.10 References

1. Iijima, S. Helical microtubules of graphitic carbon. *Nature* **1991,** *354*, 56-58.

2. Thess, A.; Lee, R.; Nikolaev, P.; Dai, H.; Petit, P.; Robert, J.; Xu, C.; Lee, Y. H.; Kim, S. G.; Rinzler, A. G.; Colbert, D. T.; Scuseria, G. E.; Tománek, D.; Fischer, J. E.; Smalley, R. E. Crystalline Ropes of Metallic Carbon Nanotubes. *Science* **1996,** *273*, 483-487.

3. O'Connell, M. J.; Bachilo, S. M.; Huffman, C. B.; Moore, V. C.; Strano, M. S.; Haroz, E. H.; Rialon, K. L.; Boul, P. J.; Noon, W. H.; Kittrell, C.; Ma, J.; Hauge, R. H.; Weisman, R. B.; Smalley, R. E. Band Gap Fluorescence from Individual Single-Walled Carbon Nanotubes. *Science* **2002,** *297*, 593-596.

4. Berber, S.; Kwon, Y.-K.; Tománek, D. Unusually High Thermal Conductivity of Carbon Nanotubes. *Physical Review Letters* **2000,** *84*, 4613-4616.

5. Treacy, M. M. J.; Ebbesen, T. W.; Gibson, J. M. Exceptionally high Young's modulus observed for individual carbon nanotubes. *Nature* **1996,** *381*, 678-680.

6. Charlier, J.-C.; Blase, X.; Roche, S. Electronic and transport properties of nanotubes. *Reviews of Modern Physics* **2007,** *79*, 677-732.

7. Bachilo, S. M.; Strano, M. S.; Kittrell, C.; Hauge, R. H.; Smalley, R. E.; Weisman, R. B. Structure-Assigned Optical Spectra of Single-Walled Carbon Nanotubes. *Science* **2002,** *298*, 2361-2366.

8. Dresselhaus, M. S.; Dresselhaus, G.; Eklund, P. C. *Science of Fullerenes and Carbon Nanotubes*. Academic Press: San Diego, 1996.

9. Fakhri, N.; Tsyboulski, D. A.; Cognet, L.; Weisman, R. B.; Pasquali, M. Diameter-dependent bending dynamics of single-walled carbon nanotubes in liquids. *Proceedings of the National Academy of Sciences of the United States of America* **2009,** *106*, 14219-14223.

10. Dresselhaus, M. S.; Dresselhaus, G.; Jorio, A. Unusual Properties and Structure oF Carbon Nanotubes. *Annual Review of Materials Research* **2004,** *34*, 247-278.

11. Rajan, A.; Strano, M. S.; Heller, D. A.; Hertel, T.; Schulten, K. Length-Dependent Optical Effects in Single Walled Carbon Nanotubes†. *The Journal of Physical Chemistry B* **2008,** *112*, 6211-6213.

12. Harrah, D. M.; Swan, A. K. The Role of Length and Defects on Optical Quantum Efficiency and Exciton Decay Dynamics in Single-Walled Carbon Nanotubes. *ACS Nano* **2011,** *5*, 647-655.

13. Hertel, T.; Himmelein, S.; Ackermann, T.; Stich, D.; Crochet, J. Diffusion Limited Photoluminescence Quantum Yields in 1-D Semiconductors: Single-Wall Carbon Nanotubes. *ACS Nano* **2010,** *4*, 7161-7168.

14. Dresselhaus, M. S.; Dresselhaus, G.; Saito, R.; Jorio, A. Raman spectroscopy of carbon nanotubes. *Physics Reports* **2005,** *409*, 47-99.

15. Heller, D. A.; Barone, P. W.; Swanson, J. P.; Mayrhofer, R. M.; Strano, M. S. Using Raman Spectroscopy to Elucidate the Aggregation State of Single-Walled Carbon Nanotubes. *Journal of Physical Chemistry B* **2004,** *108*, 6905-6909.

16. O'Connell, M. J.; Sivaram, S.; Doorn, S. K. Near-infrared resonance Raman excitation profile studies of single-walled carbon nanotube intertube interactions: A direct comparison of bundled and individually dispersed HiPco nanotubes. *Physical Review B* **2004,** *69*, 235415.

17. Rinzler, A. G.; Liu, J.; Dai, H.; Nikolaev, P.; Huffman, C. B.; Rodríguez-Macías, F. J.; Boul, P. J.; Lu, A. H.; Heymann, D.; Colbert, D. T.; Lee, R. S.; Fischer, J. E.; Rao, A. M.; Eklund, P. C.; Smalley, R. E. Large-scale purification of single-wall carbon nanotubes: process, product, and characterization. *Applied Physics A* **1998,** *67*, 29-37.

18. Journet, C.; Maser, W. K.; Bernier, P.; Loiseau, A.; de la Chapelle, M. L.; Lefrant, S.; Deniard, P.; Lee, R.; Fischer, J. E. Large-scale production of single-walled carbon nanotubes by the electric-arc technique. *Nature* **1997,** *388*, 756-758.

19. Nikolaev, P.; Bronikowski, M. J.; Bradley, R. K.; Rohmund, F.; Colbert, D. T.; Smith, K. A.; Smalley, R. E. Gas-phase catalytic growth of single-walled carbon nanotubes from carbon monoxide. *Chemical Physics Letters* **1999,** *313*, 91-97.

20. Cassell, A. M.; Raymakers, J. A.; Kong, J.; Dai, H. Large Scale CVD Synthesis of Single-Walled Carbon Nanotubes. *The Journal of Physical Chemistry B* **1999,** *103*, 6484-6492.

21. Liu, X.; Guo, L.; Morris, D.; Kane, A. B.; Hurt, R. H. Targeted removal of bioavailable metal as a detoxification strategy for carbon nanotubes. *Carbon* **2008,** *46*, 489-500.

22. Pulskamp, K.; Diabaté, S.; Krug, H. F. Carbon nanotubes show no sign of acute toxicity but induce intracellular reactive oxygen species in dependence on contaminants. *Toxicology Letters* **2007,** *168*, 58-74.

23. Islam, M. F.; Milkie, D. E.; Torrens, O. N.; Yodh, A. G.; Kikkawa, J. M. Magnetic heterogeneity and alignment of single wall carbon nanotubes. *Physical Review B* **2005,** *71*, 201401.

24. Johnston, D. E.; Islam, M. F.; Yodh, A. G.; Johnson, A. T. Electronic devices based on purified carbon nanotubes grown by high-pressure decomposition of carbon monoxide. *Nature Materials* **2005,** *4*, 589-592.

25. Becker, M. L.; Fagan, J. A.; Gallant, N. D.; Bauer, B. J.; Bajpai, V.; Hobbie, E. K.; Lacerda, S. H.; Migler, K. B.; Jakupciak, J. P. Length-Dependent Uptake of DNA-Wrapped Single-Walled Carbon Nanotubes. *Advanced Materials* **2007,** *19*, 939-945.

26. Islam, M. F.; Rojas, E.; Bergey, D. M.; Johnson, A. T.; Yodh, A. G. High Weight Fraction Surfactant Solubilization of Single-Wall Carbon Nanotubes in Water. *Nano Letters* **2003,** *3*, 269-273.

27. Arnold, M. S.; Green, A. A.; Hulvat, J. F.; Stupp, S. I.; Hersam, M. C. Sorting carbon nanotubes by electronic structure using density differentiation. *Nature Nanotechnology* **2006,** *1*, 60-65.

28. Fagan, J. A.; Becker, M. L.; Chun, J.; Hobbie, E. K. Length Fractionation of Carbon Nanotubes Using Centrifugation. *Advanced Materials* **2008,** *20*, 1609-1613.

29. Girifalco, L. A.; Hodak, M.; Lee, R. S. Carbon nanotubes, buckyballs, ropes, and a universal graphitic potential. *Physical Review B* **2000,** *62*, 13104-13110.

30. Bandyopadhyaya, R.; Nativ-Roth, E.; Regev, O.; Yerushalmi-Rozen, R. Stabilization of Individual Carbon Nanotubes in Aqueous Solutions. *Nano Letters* **2001,** *2*, 25-28.

31. Kaiser, J.-P.; Wick, P.; Manser, P.; Spohn, P.; Bruinink, A. Single walled carbon nanotubes (SWCNT) affect cell physiology and cell architecture. *Journal of Materials Science: Materials in Medicine* **2008,** *19*, 1523-1527.

32. Bekyarova, E.; Sarkar, S.; Wang, F.; Itkis, M. E.; Kalinina, I.; Tian, X.; Haddon, R. C. Effect of Covalent Chemistry on the Electronic Structure

and Properties of Carbon Nanotubes and Graphene. *Accounts of Chemical Research* **2012,** *46*, 65-76.

33. Ross, B. P.; Braddy, A. C.; McGeary, R. P.; Blanchfield, J. T.; Prokai, L.; Toth, I. Micellar Aggregation and Membrane Partitioning of Bile Salts, Fatty Acids, Sodium Dodecyl Sulfate, and Sugar-Conjugated Fatty Acids: Correlation with Hemolytic Potency and Implications for Drug Delivery. *Molecular Pharmaceutics* **2004,** *1*, 233-245.

34. Cherukuri, P.; Bachilo, S. M.; Litovsky, S. H.; Weisman, R. B. Near-Infrared Fluorescence Microscopy of Single-Walled Carbon Nanotubes in Phagocytic Cells. *Journal of the American Chemical Society* **2004,** *126*, 15638-15639.

35. Mutlu, G. M.; Budinger, G. R. S.; Green, A. A.; Urich, D.; Soberanes, S.; Chiarella, S. E.; Alheid, G. F.; McCrimmon, D. R.; Szleifer, I.; Hersam, M. C. Biocompatible Nanoscale Dispersion of Single-Walled Carbon Nanotubes Minimizes in vivo Pulmonary Toxicity. *Nano Letters* **2010,** *10*, 1664-1670.

36. Holt, B. D.; Short, P. A.; Rape, A. D.; Wang, Y.-l.; Islam, M. F.; Dahl, K. N. Carbon Nanotubes Reorganize Actin Structures in Cells and ex Vivo. *ACS Nano* **2010,** *4*, 4872-4878.

37. Yaron, P.; Holt, B.; Short, P.; Lösche, M.; Islam, M.; Dahl, K. Single wall carbon nanotubes enter cells by endocytosis and not membrane penetration. *Journal of Nanobiotechnology* **2011,** *9*, 45.

38. Holt, B. D.; Shams, H.; Horst, T. A.; Basu, S.; Rape, A. D.; Wang, Y.-L.; Rohde, G. K.; Mofrad, M. R. K.; Islam, M. F.; Dahl, K. N. Altered Cell Mechanics from the Inside: Dispersed Single Wall Carbon Nanotubes Integrate with and Restructure Actin. *Journal of Functional Biomaterials* **2012,** *3*, 398-417.

39. Boyer, P. D.; Holt, B. D.; Islam, M. F.; Dahl, K. N. Decoding membrane- versus receptor-mediated delivery of single-walled carbon nanotubes into macrophages using modifications of nanotube surface coatings and cell activity. *Soft Matter* **2013,** *9*, 758-764.

40. Kam, N. W. S.; O'Connell, M.; Wisdom, J. A.; Dai, H. Carbon nanotubes as multifunctional biological transporters and near-infrared agents for selective cancer cell destruction. *Proceedings of the National Academy of Sciences of the United States of America* **2005,** *102*, 11600-11605.

41. Konduru, N. V.; Tyurina, Y. Y.; Feng, W.; Basova, L. V.; Belikova, N. A.; Bayir, H.; Clark, K.; Rubin, M.; Stolz, D.; Vallhov, H.; Scheynius, A.;

Witasp, E.; Fadeel, B.; Kichambare, P. D.; Star, A.; Kisin, E. R.; Murray, A. R.; Shvedova, A. A.; Kagan, V. E. Phosphatidylserine Targets Single-Walled Carbon Nanotubes to Professional Phagocytes *In Vitro* and *In Vivo*. *PLoS ONE* **2009,** *4*, e4398.

42. Tsyboulski, D. A.; Bakota, E. L.; Witus, L. S.; Rocha, J.-D. R.; Hartgerink, J. D.; Weisman, R. B. Self-Assembling Peptide Coatings Designed for Highly Luminescent Suspension of Single-Walled Carbon Nanotubes. *Journal of the American Chemical Society* **2008,** *130*, 17134-17140.

43. Bakota, E. L.; Aulisa, L.; Tsyboulski, D. A.; Weisman, R. B.; Hartgerink, J. D. Multidomain Peptides as Single-Walled Carbon Nanotube Surfactants in Cell Culture. *Biomacromolecules* **2009,** *10*, 2201-2206.

44. Zheng, M.; Jagota, A.; Semke, E. D.; Diner, B. A.; McLean, R. S.; Lustig, S. R.; Richardson, R. E.; Tassi, N. G. DNA-assisted dispersion and separation of carbon nanotubes. *Nature Materials* **2003,** *2*, 338-342.

45. Karajanagi, S. S.; Vertegel, A. A.; Kane, R. S.; Dordick, J. S. Structure and Function of Enzymes Adsorbed onto Single-Walled Carbon Nanotubes. *Langmuir* **2004,** *20*, 11594-11599.

46. Asuri, P.; Karajanagi, S. S.; Yang, H.; Yim, T.-J.; Kane, R. S.; Dordick, J. S. Increasing Protein Stability through Control of the Nanoscale Environment. *Langmuir* **2006,** *22*, 5833-5836.

47. Karajanagi, S. S.; Yang, H.; Asuri, P.; Sellitto, E.; Dordick, J. S.; Kane, R. S. Protein-Assisted Solubilization of Single-Walled Carbon Nanotubes. *Langmuir* **2006,** *22*, 1392-1395.

48. Matsuura, K.; Saito, T.; Okazaki, T.; Ohshima, S.; Yumura, M.; Iijima, S. Selectivity of water-soluble proteins in single-walled carbon nanotube dispersions. *Chemical Physics Letters* **2006,** *429*, 497-502.

49. Nepal, D.; Geckeler, K. E. Proteins and Carbon Nanotubes: Close Encounter in Water. *Small* **2007,** *3*, 1259-1265.

50. Edri, E.; Regev, O. "Shaken, Not Stable": Dispersion Mechanism and Dynamics of Protein-Dispersed Nanotubes Studied via Spectroscopy. *Langmuir* **2009,** *25*, 10459-10465.

51. Ge, C.; Du, J.; Zhao, L.; Wang, L.; Liu, Y.; Li, D.; Yang, Y.; Zhou, R.; Zhao, Y.; Chai, Z.; Chen, C. Binding of blood proteins to carbon nanotubes reduces cytotoxicity. *Proceedings of the National Academy of Sciences of the United States of America* **2011,** *108*, 16968-16973.

52. Calvaresi, M.; Zerbetto, F. The Devil and Holy Water: Protein and Carbon Nanotube Hybrids. *Accounts of Chemical Research* **2013,** *46*, 2454-2463.

53. Holt, B. D.; Dahl, K. N.; Islam, M. F. Quantification of Uptake and Localization of Bovine Serum Albumin-Stabilized Single-Wall Carbon Nanotubes in Different Human Cell Types. *Small* **2011,** *7*, 2348-2355.

54. Holt, B. D.; Dahl, K. N.; Islam, M. F. Cells Take up and Recover from Protein-Stabilized Single-Wall Carbon Nanotubes with Two Distinct Rates. *ACS Nano* **2012,** *6*, 3481-3490.

55. Holt, B. D.; McCorry, M. C.; Boyer, P. D.; Dahl, K. N.; Islam, M. F. Not all protein-mediated single-wall carbon nanotube dispersions are equally bioactive. *Nanoscale* **2012,** *4*, 7425-7434.

56. Shams, H.; Holt, B. D.; Mahboobi, S. H.; Jahed, Z.; Islam, M. F.; Dahl, K. N.; Mofrad, M. R. K. Actin Reorganization through Dynamic Interactions with Single-Wall Carbon Nanotubes. *ACS Nano* **2013,** *8*, 188-197.

57. Cherukuri, P.; Gannon, C. J.; Leeuw, T. K.; Schmidt, H. K.; Smalley, R. E.; Curley, S. A.; Weisman, R. B. Mammalian pharmacokinetics of carbon nanotubes using intrinsic near-infrared fluorescence. *Proceedings of the National Academy of Sciences of the United States of America* **2006,** *103*, 18882-18886.

58. Shao, N.; Lu, S.; Wickstrom, E.; Panchapakesan, B. Integrated molecular targeting of IGF1R and HER2 surface receptors and destruction of breast cancer cells using single wall carbon nanotubes. *Nanotechnology* **2007,** *18*.

59. Welsher, K.; Liu, Z.; Daranciang, D.; Dai, H. Selective Probing and Imaging of Cells with Single Walled Carbon Nanotubes as Near-Infrared Fluorescent Molecules. *Nano Letters* **2008,** *8*, 586-590.

60. Liu, Z.; Cai, W.; He, L.; Nakayama, N.; Chen, K.; Sun, X.; Chen, X.; Dai, H. In vivo biodistribution and highly efficient tumour targeting of carbon nanotubes in mice. *Nature Nanotechnology* **2007,** *2*, 47-52.

61. Zhang, X.; Meng, L.; Lu, Q.; Fei, Z.; Dyson, P. J. Targeted delivery and controlled release of doxorubicin to cancer cells using modified single wall carbon nanotubes. *Biomaterials* **2009,** *30*, 6041-6047.

62. Frise, A. E.; Edri, E.; Furó, I.; Regev, O. Protein Dispersant Binding on Nanotubes Studied by NMR Self-Diffusion and Cryo-TEM Techniques. *The Journal of Physical Chemistry Letters* **2010,** *1*, 1414-1419.

63. Smith, A. M.; Mancini, M. C.; Nie, S. Bioimaging: Second window for in vivo imaging. *Nature Nanotechnology* **2009,** *4*, 710-711.

64. Welsher, K.; Liu, Z.; Sherlock, S. P.; Robinson, J. T.; Chen, Z.; Daranciang, D.; Dai, H. A route to brightly fluorescent carbon nanotubes for near-infrared imaging in mice. *Nature Nanotechnology* **2009,** *4*, 773-780.

65. Heller, D. A.; Baik, S.; Eurell, T. E.; Strano, M. S. Single-Walled Carbon Nanotube Spectroscopy in Live Cells: Towards Long-Term Labels and Optical Sensors. *Advanced Materials* **2005,** *17*, 2793-2799.

66. Hong, G.; Lee, J. C.; Robinson, J. T.; Raaz, U.; Xie, L.; Huang, N. F.; Cooke, J. P.; Dai, H. Multifunctional in vivo vascular imaging using near-infrared II fluorescence. *Nature Medicine* **2012,** *18*, 1841-1846.

67. Robinson, J. T.; Hong, G.; Liang, Y.; Zhang, B.; Yaghi, O. K.; Dai, H. In Vivo Fluorescence Imaging in the Second Near-Infrared Window with Long Circulating Carbon Nanotubes Capable of Ultrahigh Tumor Uptake. *Journal of the American Chemical Society* **2012,** *134*, 10664-10669.

68. Holt, B. D. Cellular Processing of Single Wall Carbon Nanotubes. PhD Thesis: Carnegie Mellon University, Pittsburgh, PA, 2014.

69. Heller, D. A.; Jeng, E. S.; Yeung, T.-K.; Martinez, B. M.; Moll, A. E.; Gastala, J. B.; Strano, M. S. Optical Detection of DNA Conformational Polymorphism on Single-Walled Carbon Nanotubes. *Science* **2006,** *311*, 508-511.

70. Barone, P. W.; Strano, M. S. Single Walled Carbon Nanotubes as Reporters for the Optical Detection of Glucose. *Journal of Diabetes Science and Technology* **2009,** *3*, 242-252.

71. Kim, J.-H.; Heller, D. A.; Jin, H.; Barone, P. W.; Song, C.; Zhang, J.; Trudel, L. J.; Wogan, G. N.; Tannenbaum, S. R.; Strano, M. S. The rational design of nitric oxide selectivity in single-walled carbon nanotube near-infrared fluorescence sensors for biological detection. *Nature Chemistry* **2009,** *1*, 473-481.

72. Kruss, S.; Hilmer, A. J.; Zhang, J.; Reuel, N. F.; Mu, B.; Strano, M. S. Carbon nanotubes as optical biomedical sensors. *Advanced Drug Delivery Reviews* **2013,** *65*, 1933-1950.

73. Pantarotto, D.; Singh, R.; McCarthy, D.; Erhardt, M.; Briand, J.-P.; Prato, M.; Kostarelos, K.; Bianco, A. Functionalized Carbon Nanotubes for

Plasmid DNA Gene Delivery. *Angewandte Chemie International Edition* **2004,** *43*, 5242-5246.

74. Liu, Y.; Wu, D.-C.; Zhang, W.-D.; Jiang, X.; He, C.-B.; Chung, T. S.; Goh, S. H.; Leong, K. W. Polyethylenimine-Grafted Multiwalled Carbon Nanotubes for Secure Noncovalent Immobilization and Efficient Delivery of DNA. *Angewandte Chemie International Edition* **2005,** *44*, 4782-4785.

75. Singh, R.; Pantarotto, D.; McCarthy, D.; Chaloin, O.; Hoebeke, J.; Partidos, C. D.; Briand, J.-P.; Prato, M.; Bianco, A.; Kostarelos, K. Binding and Condensation of Plasmid DNA onto Functionalized Carbon Nanotubes: Toward the Construction of Nanotube-Based Gene Delivery Vectors. *Journal of the American Chemical Society* **2005,** *127*, 4388-4396.

76. Kam, N. W. S.; Liu, Z.; Dai, H. Functionalization of Carbon Nanotubes via Cleavable Disulfide Bonds for Efficient Intracellular Delivery of siRNA and Potent Gene Silencing. *Journal of the American Chemical Society* **2005,** *127*, 12492-12493.

77. Liu, Z.; Winters, M.; Holodniy, M.; Dai, H. siRNA Delivery into Human T Cells and Primary Cells with Carbon-Nanotube Transporters. *Angewandte Chemie International Edition* **2007,** *46*, 2023-2027.

78. Siu, K. S.; Chen, D.; Zheng, X.; Zhang, X.; Johnston, N.; Liu, Y.; Yuan, K.; Koropatnick, J.; Gillies, E. R.; Min, W.-P. Non-covalently functionalized single-walled carbon nanotube for topical siRNA delivery into melanoma. *Biomaterials* **2014,** *35*, 3435-3442.

79. Shi Kam, N. W.; Jessop, T. C.; Wender, P. A.; Dai, H. Nanotube Molecular Transporters: Internalization of Carbon Nanotube−Protein Conjugates into Mammalian Cells. *Journal of the American Chemical Society* **2004,** *126*, 6850-6851.

80. Kam, N. W. S.; Dai, H. Carbon Nanotubes as Intracellular Protein Transporters: Generality and Biological Functionality. *Journal of the American Chemical Society* **2005,** *127*, 6021-6026.

81. Liu, Z.; Sun, X.; Nakayama-Ratchford, N.; Dai, H. Supramolecular Chemistry on Water-Soluble Carbon Nanotubes for Drug Loading and Delivery. *ACS Nano* **2007,** *1*, 50-56.

82. Liu, Z.; Chen, K.; Davis, C.; Sherlock, S.; Cao, Q.; Chen, X.; Dai, H. Drug Delivery with Carbon Nanotubes for In vivo Cancer Treatment. *Cancer Research* **2008,** *68*, 6652-6660.

83. Wong, B. S.; Yoong, S. L.; Jagusiak, A.; Panczyk, T.; Ho, H. K.; Ang, W. H.; Pastorin, G. Carbon nanotubes for delivery of small molecule drugs. *Advanced Drug Delivery Reviews* **2013,** *65*, 1964-2015.

84. König, K. Multiphoton microscopy in life sciences. *Journal of Microscopy* **2000,** *200*, 83-104.

85. Liang, C.; Diao, S.; Wang, C.; Gong, H.; Liu, T.; Hong, G.; Shi, X.; Dai, H.; Liu, Z. Tumor Metastasis Inhibition by Imaging-Guided Photothermal Therapy with Single-Walled Carbon Nanotubes. *Advanced Materials* **2014,** *26*, 5646-5652.

86. Antaris, A. L.; Robinson, J. T.; Yaghi, O. K.; Hong, G.; Diao, S.; Luong, R.; Dai, H. Ultra-Low Doses of Chirality Sorted (6,5) Carbon Nanotubes for Simultaneous Tumor Imaging and Photothermal Therapy. *ACS Nano* **2013,** *7*, 3644-3652.

87. Robinson, J.; Welsher, K.; Tabakman, S.; Sherlock, S.; Wang, H.; Luong, R.; Dai, H. High performance in vivo near-IR (>1 μm) imaging and photothermal cancer therapy with carbon nanotubes. *Nano Research* **2010,** *3*, 779-793.

88. Zhou, F.; Wu, S.; Song, S.; Chen, W. R.; Resasco, D. E.; Xing, D. Antitumor immunologically modified carbon nanotubes for photothermal therapy. *Biomaterials* **2012,** *33*, 3235-3242.

89. Kang, B.; Yu, D.; Dai, Y.; Chang, S.; Chen, D.; Ding, Y. Cancer-Cell Targeting and Photoacoustic Therapy Using Carbon Nanotubes as "Bomb" Agents. *Small* **2009,** *5*, 1292-1301.

90. Kosuge, H.; Sherlock, S. P.; Kitagawa, T.; Dash, R.; Robinson, J. T.; Dai, H.; McConnell, M. V. Near Infrared Imaging and Photothermal Ablation of Vascular Inflammation Using Single-Walled Carbon Nanotubes. *Journal of the American Heart Association* **2012,** *1*.

91. Gordon, S.; Taylor, P. R. Monocyte and macrophage heterogeneity. *Nature Reviews Immunology* **2005,** *5*, 953-964.

92. Doherty, G. J.; McMahon, H. T. Mechanisms of Endocytosis. *Annual Review of Biochemistry* **2009,** *78*, 857-902.

93. Conner, S. D.; Schmid, S. L. Regulated portals of entry into the cell. *Nature* **2003,** *422*, 37-44.

94. Groves, E.; Dart, A.; Covarelli, V.; Caron, E. Molecular mechanisms of phagocytic uptake in mammalian cells. *Cellular and Molecular Life Sciences* **2008,** *65*, 1957-1976.

95. Alberts, B.; Wilson, J. H.; Hunt, T. *Molecular biology of the cell*. 5th ed.; Garland Science: New York, 2008

96. Moghimi, S. M.; Hunter, A. C.; Murray, J. C. Long-Circulating and Target-Specific Nanoparticles: Theory to Practice. *Pharmacological Reviews* **2001,** *53*, 283-318.

97. Champion, J. A.; Mitragotri, S. Role of target geometry in phagocytosis. *Proceedings of the National Academy of Sciences of the United States of America* **2006,** *103*, 4930-4934.

98. Walkey, C. D.; Olsen, J. B.; Guo, H.; Emili, A.; Chan, W. C. W. Nanoparticle Size and Surface Chemistry Determine Serum Protein Adsorption and Macrophage Uptake. *Journal of the American Chemical Society* **2011,** *134*, 2139-2147.

99. Ahsan, F.; Rivas, I. P.; Khan, M. A.; Torres Suárez, A. I. Targeting to macrophages: role of physicochemical properties of particulate carriers—liposomes and microspheres—on the phagocytosis by macrophages. *Journal of Controlled Release* **2002,** *79*, 29-40.

100. Walkey, C. D.; Chan, W. C. W. Understanding and controlling the interaction of nanomaterials with proteins in a physiological environment. *Chemical Society Reviews* **2012,** *41*, 2780-2799.

101. dos Santos, T.; Varela, J.; Lynch, I.; Salvati, A.; Dawson, K. A. Quantitative Assessment of the Comparative Nanoparticle-Uptake Efficiency of a Range of Cell Lines. *Small* **2011,** *7*, 3341-3349.

102. Moghimi, S. M.; Hunter, A. C.; Murray, J. C. Nanomedicine: current status and future prospects. *The FASEB Journal* **2005,** *19*, 311-330.

103. França, A.; Aggarwal, P.; Barsov, E. V.; Kozlov, S. V.; Dobrovolskaia, M. A.; González-Fernández, Á. Macrophage scavenger receptor A mediates the uptake of gold colloids by macrophages in vitro. *Nanomedicine* **2011,** *6*, 1175-1188.

104. Bastús, N. G.; Sánchez-Tilló, E.; Pujals, S.; Farrera, C.; López, C.; Giralt, E.; Celada, A.; Lloberas, J.; Puntes, V. Homogeneous Conjugation of Peptides onto Gold Nanoparticles Enhances Macrophage Response. *ACS Nano* **2009,** *3*, 1335-1344.

105. Pitsillides, C. M.; Joe, E. K.; Wei, X.; Anderson, R. R.; Lin, C. P. Selective Cell Targeting with Light-Absorbing Microparticles and Nanoparticles. *Biophysical Journal* **2003,** *84*, 4023-4032.

106. Weissleder, R.; Kelly, K.; Sun, E. Y.; Shtatland, T.; Josephson, L. Cell-specific targeting of nanoparticles by multivalent attachment of small molecules. *Nature Biotechnology* **2005,** *23*, 1418-1423.

107. Kelly, C.; Jefferies, C.; Cryan, S.-A. Targeted Liposomal Drug Delivery to Monocytes and Macrophages. *Journal of Drug Delivery* **2011,** *2011*.

108. Kagan, V. E.; Tyurina, Y. Y.; Tyurin, V. A.; Konduru, N. V.; Potapovich, A. I.; Osipov, A. N.; Kisin, E. R.; Schwegler-Berry, D.; Mercer, R.; Castranova, V.; Shvedova, A. A. Direct and indirect effects of single walled carbon nanotubes on RAW 264.7 macrophages: Role of iron. *Toxicology Letters* **2006,** *165*, 88-100.

109. Dumortier, H.; Lacotte, S.; Pastorin, G.; Marega, R.; Wu, W.; Bonifazi, D.; Briand, J.-P.; Prato, M.; Muller, S.; Bianco, A. Functionalized Carbon Nanotubes Are Non-Cytotoxic and Preserve the Functionality of Primary Immune Cells. *Nano Letters* **2006,** *6*, 1522-1528.

110. Porter, A. E.; Gass, M.; Muller, K.; Skepper, J. N.; Midgley, P. A.; Welland, M. Direct imaging of single-walled carbon nanotubes in cells. *Nature Nanotechnology* **2007,** *2*, 713-717.

111. Bertulli, C.; Beeson, H. J.; Hasan, T.; Huang, Y. Y. S. Spectroscopic characterization of protein-wrapped single-wall carbon nanotubes and quantification of their cellular uptake in multiple cell generations. *Nanotechnology* **2013,** *24*.

112. Choi, J. H.; Nguyen, F. T.; Barone, P. W.; Heller, D. A.; Moll, A. E.; Patel, D.; Boppart, S. A.; Strano, M. S. Multimodal Biomedical Imaging with Asymmetric Single-Walled Carbon Nanotube/Iron Oxide Nanoparticle Complexes. *Nano Letters* **2007,** *7*, 861-867.

113. Gao, N.; Zhang, Q.; Mu, Q.; Bai, Y.; Li, L.; Zhou, H.; Butch, E. R.; Powell, T. B.; Snyder, S. E.; Jiang, G.; Yan, B. Steering Carbon Nanotubes to Scavenger Receptor Recognition by Nanotube Surface Chemistry Modification Partially Alleviates NFκB Activation and Reduces Its Immunotoxicity. *ACS Nano* **2011,** *5*, 4581-4591.

114. Kagan, V. E.; Konduru, N. V.; Feng, W.; Allen, B. L.; Conroy, J.; Volkov, Y.; Vlasova, I. I.; Belikova, N. A.; Yanamala, N.; Kapralov, A.; Tyurina, Y. Y.; Shi, J.; Kisin, E. R.; Murray, A. R.; Franks, J.; Stolz, D.; Gou, P.; Klein-Seetharaman, J.; Fadeel, B.; Star, A.; Shvedova, A. A. Carbon nanotubes degraded by neutrophil myeloperoxidase induce less pulmonary inflammation. *Nature Nanotechnology* **2010,** *5*, 354-359.

115. Kagan, V. E.; Kapralov, A. A.; St. Croix, C. M.; Watkins, S. C.; Kisin, E. R.; Kotchey, G. P.; Balasubramanian, K.; Vlasova, I. I.; Yu, J.; Kim, K.; Seo, W.; Mallampalli, R. K.; Star, A.; Shvedova, A. A. Lung Macrophages "Digest" Carbon Nanotubes Using a Superoxide/Peroxynitrite Oxidative Pathway. *ACS Nano* **2014,** *8*, 5610-5621.

116. Fadel, T. R.; Sharp, F. A.; Vudattu, N.; Ragheb, R.; Garyu, J.; Kim, D.; Hong, E.; Li, N.; Haller, G. L.; Pfefferle, L. D.; Justesen, S.; Herold, K. C.; Fahmy, T. M. A carbon nanotube-polymer composite for T-cell therapy. *Nature Nanotechnology* **2014,** *9*, 639-647.

117. Pescatori, M.; Bedognetti, D.; Venturelli, E.; Ménard-Moyon, C.; Bernardini, C.; Muresu, E.; Piana, A.; Maida, G.; Manetti, R.; Sgarrella, F.; Bianco, A.; Delogu, L. G. Functionalized carbon nanotubes as immunomodulator systems. *Biomaterials* **2013,** *34*, 4395-4403.

118. Meng, J.; Duan, J.; Kong, H.; Li, L.; Wang, C.; Xie, S.; Chen, S.; Gu, N.; Xu, H.; Yang, X.-D. Carbon Nanotubes Conjugated to Tumor Lysate Protein Enhance the Efficacy of an Antitumor Immunotherapy. *Small* **2008,** *4*, 1364-1370.

119. Pantarotto, D.; Partidos, C. D.; Hoebeke, J.; Brown, F.; Kramer, E.; Briand, J.-P.; Muller, S.; Prato, M.; Bianco, A. Immunization with Peptide-Functionalized Carbon Nanotubes Enhances Virus-Specific Neutralizing Antibody Responses. *Chemistry & Biology* **2003,** *10*, 961-966.

120. Parra, J.; Abad-Somovilla, A.; Mercader, J. V.; Taton, T. A.; Abad-Fuentes, A. Carbon nanotube-protein carriers enhance size-dependent self-adjuvant antibody response to haptens. *Journal of Controlled Release* **2013,** *170*, 242-251.

121. Villa, C. H.; Dao, T.; Ahearn, I.; Fehrenbacher, N.; Casey, E.; Rey, D. A.; Korontsvit, T.; Zakhaleva, V.; Batt, C. A.; Philips, M. R.; Scheinberg, D. A. Single-Walled Carbon Nanotubes Deliver Peptide Antigen into Dendritic Cells and Enhance IgG Responses to Tumor-Associated Antigens. *ACS Nano* **2011,** *5*, 5300-5311.

122. Zeinali, M.; Jammalan, M.; Ardestani, S. K.; Mosaveri, N. Immunological and cytotoxicological characterization of tuberculin purified protein derivative (PPD) conjugated to single-walled carbon nanotubes. *Immunology Letters* **2009,** *126*, 48-53.

3 Decoding Membrane- *versus* Receptor-Mediated Delivery of Single Wall Carbon Nanotubes into Macrophages using Modifications of Nanotube Surface Coatings and Cell Activity

3.1 Introduction

Understanding the interactions between nanomaterials and immune cells and quantifying uptake precisely are important both for determining toxicity and for developing medical therapeutics related to cancer, inflammation, wound healing, and regenerative medicine. Macrophages from monocytes and resident tissue macrophages are responsible for removing unwanted materials and cellular debris from the body, particularly in the M1 or pro-inflammatory phenotype.[1] These cells would likely be the first to encounter therapeutic materials[2] and thus are largely responsible for dictating the fate, processing, and ultimate effect of those materials. Local macrophage concentration increases in regions of infection, inflammation, and wound healing, as well as in pathological regions including tumor environments and regions of atherosclerosis.[3-4] Targeted delivery of nanomaterials to macrophages could potentially be utilized for more precise imaging of macrophages within the body, as well as drug delivery and thermal ablation of macrophages.[5] Additionally, macrophages loaded with nanomaterials

offer the exciting potential of cell-mediated drug delivery as these cells can cross the blood-brain barrier.[6]

Recent studies have shown the potential for single wall carbon nanotubes (SWCNTs) as drug and gene delivery vectors,[7] imaging probes for cellular labeling,[8-9] tracking agents[10-12] and molecular sensors.[13-14] SWCNTs are hydrophobic materials that aggregate in water leading to diminished optical properties[15] and deleterious cellular effects.[16] SWCNTs have been dispersed through various covalent modifications and non-covalent functionalization with poly(ethylene oxide) (PEO) based copolymers,[8, 17] lipids,[5, 18] DNA,[19] peptides,[20] and proteins.[21-25] Well-dispersed individual SWCNTs have been used in cellular applications without acute toxicity.[17]

Cellular uptake of and response to SWCNTs are also impacted by SWCNT functionalization and cell type. In direct comparisons, macrophages show increased nanoparticle uptake efficiency over epithelial, astrocytes, and endothelial cell types.[26] For targeting to macrophages, it is unclear if nanomaterial surface coating or cell activation state is the dominant factor for cell uptake. Macrophages treated with lipopolysaccharide (LPS) to produce an M1 phenotype[1] show altered immune response after treatment with functionalized nanomaterials.[27] Conversely, some functionalized SWCNTs provoke pro-inflammatory cytokine secretion.[28] However, there has been no quantitative evidence to determine how cellular activity is related to amount of SWCNT uptake.

An understanding of the mechanism of uptake is required both to gauge toxicity and to dose nanomaterials for cellular therapy. Traditionally, cellular uptake mechanisms are determined using either fluorescence labeling of cellular components or blocking cellular pathways with chemical agents. However, these methods are inapplicable with SWCNTs since nanotubes nonlinearly quench fluorescence,[29] which limits or eliminates the ability to precisely track materials within subcellular compartments. Also, the SWCNT–cell interaction is inherently non-specific and determining cellular uptake mechanisms using chemical blocking agents may lead to inconclusive results since chemical agents have broad, overlapping effects on cell processes.

Herein, we extract details of mechanistic uptake and underlying cellular effects by modulating SWCNT surface coating and quantifying associated variations in cellular activity. We employ Raman confocal imaging and spectroscopy to systematically measure nanotube uptake and subcellular localization as functions of nanotube surface coating with bioinert triblock copolymer, Pluronic F127 (PF127), and bioactive bovine serum albumin (BSA). We also quantify nanotube delivery with altered macrophage activity using LPS stimulation. Macrophages show a 100-fold increase in SWCNT uptake and adaptation of cellular size to accommodate SWCNTs, in contrast to fibroblasts. We combine these experimental measurements with models of passive and active cellular uptake[30-31] to estimate membrane- *versus* receptor-mediated uptake of SWCNTs into macrophages.

3.2 Materials and Methods

3.2.1 SWCNT Dispersion Preparation and Characterization

Unpurified SWCNTs (HiPCO (high-pressure carbon monoxide conversion synthesis), Carbon Nanotechnologies, Inc.) were purified according to previous methods, resulting in purified, unaltered SWCNTs (< 5 wt% carbonaceous impurities, ~0.3 wt% metallic impurities).[32-33] As described previously, individual SWCNTs were isolated from bundles[34-35] and length fractionated using a density gradient,[36] resulting in SWCNTs with lengths[37] of 145 ± 17 nm and diameters of 1 ± 0.3 nm. For this work, purified and length fractionated SWCNTs were dispersed in ultrapure water using either Pluronic F127 (PF127; BASF) or bovine serum albumin (BSA; Sigma-Aldrich) at a SWCNT:PF127 or SWCNT:BSA ratio of 1:10 by weight for a final SWCNT concentration of 0.1 wt%. The solutions were probe-tip sonicated in large volumes (~6 mL) for 2 h at 60 W. Solutions were centrifuged (Beckman Coulter Allegra 25R Centrifuge with TA–15–1.5 rotor) at 21,000×g for 30 min (SWCNTs–PF127) or 7 min (SWCNTs–BSA) to remove bundles. The supernatants were collected and examined using UV–vis–NIR absorption spectroscopy (Varian Cary 5000 Spectrophotometer), and concentrations were determined using an extinction coefficient of 2.6 (absorbance mL (mg mm)$^{-1}$) at 930 nm.[36] Characterization of PF127 and BSA dispersed SWCNTs in water has been examined in detail elsewhere.[17, 25] Here we used UV-vis-NIR absorbance spectroscopy and confocal Raman spectroscopy to examine the stability of SWCNTs-PF127 and SWCNTs-BSA in complete cell culture media over the full 48 h exposure time at 50 μg/mL which was the average

experimental concentration tested. For Raman spectroscopy, samples were analyzed on an inverted, inVia confocal Raman microscope (Renishaw) using a 50× dry objective with 0.75 numerical aperture (NA) and a 785 nm laser (100 mW). Spectra were acquired between 100 – 3200 cm^{-1}. Each Raman spectrum was normalized by it graphene band (G-band) intensity. Supernatants were sterilized by ultraviolet light for 1 h before use in cell experiments.

3.2.2 Cell Culture and Treatment

J774A.1 murine macrophage-like cells (ATCC, Catalog #TIB-67) were cultured in Dulbecco's Modified Eagle's Medium (high glucose (4500 mg/L), 4.0 mM L-glutamine and with no sodium pyruvate; Thermo Scientific Hyclone) supplemented with 10% v/v fetal bovine serum (Invitrogen) and 1% v/v penicillin-streptomycin (Invitrogen). NIH-3T3 murine fibroblast cells were cultured in similar media with newborn calf serum, not fetal bovine serum (Invitrogen).

J774A.1 cells were seeded at 2.0×10^4 cells/cm^2 or NIH-3T3 cells were seeded at 3.0×10^4 cells/cm^2 in 96-well plates and maintained for 24 h. SWCNTs–PF127 or SWCNTs–BSA were diluted to the indicated concentrations in fresh cell culture media and added to the cells. Ultrapure, sterile filtered water was diluted in cell culture media for sham experiments to ensure the same total volume and dilution for every well. Each treatment condition was performed in triplicate. For indicated cases with J774A.1 cells, lipopolysaccharide (LPS; Invitrogen, Catalog #L4391) was added with SWCNTs at a concentration of 5

μg/mL. Cells were maintained in culture for 48 h, after which the media was removed. Cells were then gently washed once with phosphate-buffered saline (PBS; Invitrogen).

To determine cells per well, 180 μL of PBS was added to each well, and the cells were quickly imaged using phase contrast on a Nikon Eclipse TS100 with a 20× (0.4 NA) dry objective (n > 5 fields of view with ~ 0.1 mm^2 per field). The total cell count per well was determined by manually counting cells per field of view and extrapolating the density to the entire well area. Projected cell area was measured by tracing cell outlines and quantified using ImageJ. For J774A.1 and NIH-3T3 cells, > 250 and > 80 cells, respectively, per condition were analyzed. Statistical analysis between indicated groups was performed with a Student's t-test of means.

3.2.3 Determination of Proliferation and Viability

J774A.1 cells were seeded at 5.0×10^3 cells/cm^2 in 6-well plates and maintained in culture for 24 h. As in other experiments, SWCNTs were diluted to the indicated concentrations in fresh cell culture media and added to the cells; 1 wt% PF127 or BSA solutions were also investigated for cellular effects. Cells with the indicated treatments were maintained in culture for 48 h. Subsequently, the media with SWCNTs was removed and replaced with fresh media (without phenol red) for imaging. Hoechst 33342, a cell permeable nucleic acid stain, and propidium iodide (PI), a cell impermeable nucleic acid stain, were added for quantification of total cells and dead cells, respectively. Images were taken (n >

10 fields of view with ~ 0.4 mm^2 per field) in phase contrast, blue fluorescence (Hoechst 33342) and red fluorescence (PI) on a Leica DMI 6000B inverted light and fluorescence microscope maintained at 37 °C with a 20× (0.4 NA) dry objective. For each condition, > 10 fields of view with ~2000 cells were analyzed. Nuclei were automatically segmented and enumerated using ImageJ with manual verification for accurate segmentation. Proliferation was measured as a percentage of cells normalized to control cell count. Viability was measured by PI exclusion normalized to total cell count with Hoechst.

3.2.4 Quantification of SWCNT Uptake

After imaging, cells were incubated in lysis buffer (Cell Signaling Technologies) at 4 °C for 1 h and then exposed to probe tip sonication for 10 s at 6 W. To quantify the concentration of SWCNTs per well, the sonicated lysate solutions were pipetted into a 24-well glass (#1.5) bottom plate (MatTek) and subjected to Raman confocal imaging (inVia Raman microscope, Renishaw) with a 785 nm laser (100 mW) and a 50× (0.75 NA) dry objective. SWCNT concentration was determined from the intensity of the G-band at 1590 cm^{-1} using a standard curve previously reported by our group.[24] Precise measurements of G-band intensity relative to the standard curve across multiple days were ensured by calibrating to the same silicon standard before each experiment. Uncertainties in our measurement of SWCNTs per cell reflect the propagation of uncertainties in measurements of total cell count per well and G-band intensity. We calculated an approximate number of SWCNTs from the experimentally measured mass using

the molecular weight of a single SWCNT. Briefly, the molecular weight was determined by considering the number of unit cell repeats along the average 1 nm diameter and an average length of 145 nm for our SWCNTs, using a sp^2 carbon-carbon bond length of 1.421 Å.

3.2.5 Model and Parameter Fitting

The receptor-mediated model was fit to SWCNTs–BSA uptake data using a nonlinear least squares method available in the MATLAB Curve Fitting Toolbox software (MathWorks).

3.2.6 Raman Confocal Imaging and Spectroscopy

For imaging experiments, J774A.1 cells were seeded at 5.0×10^3 cells/cm^2 onto sterilized 22 × 22 mm glass coverslips (Fisher), placed in 35 mm cell culture dishes and maintained for 24 h. SWCNTs–PF127 and SWCNTs–BSA were diluted to 30 μg/mL in fresh cell culture media and added to the cells. After 48 h, the media containing SWCNTs was removed. Cells were then gently washed three times in PBS and subsequently fixed with 3.7% v/v formaldehyde (Sigma-Aldrich) for 15 min. Phase contrast imaging and Raman confocal imaging were performed on an inverted Raman confocal microscope (inVia Raman microscope, Renishaw) with a 785 nm laser (100 mW) and a 100× (1.4 NA) oil immersion phase objective. Static scans for 100 ms around the G-band (1327 – 1819 cm^{-1}) were collected with an acquisition step size of 1 μm over a concatenation of 9

fields of view. Spatial maps of the G-band signal intensity (1590 ± 15 cm^{-1}) above the baseline signal were performed in WiRE software (Renishaw).

3.3 Results and Discussion

3.3.1 SWCNT Dispersion Stability in Media

SWCNTs were well-dispersed at high mass yields in water using either PF127 or BSA.[17, 22] However, cellular applications require SWCNT use in complex solutions with high ionic strength, proteins, lipids, and other biomolecules. Therefore, the stability of SWCNT dispersions in biologically relevant media is critical for determining accurate interaction mechanisms with cells and maintaining SWCNT properties for application. To assess SWCNT dispersion stability, we diluted SWCNTs to 50 μg/mL in water or media supplemented with 10% v/v serum protein and tracked their dispersion state using UV-vis-NIR absorbance spectroscopy and Raman spectroscopy over 48 h. For both SWCNTs-PF127 and SWCNTs-BSA, the absorbance peaks in the NIR showed no significant peak shift, broadening, or loss of intensity upon dilution in complete cell culture media over 48 h (maintained at 37 °C), suggesting dispersions remain stable in the supernatant with little displacement or exchange of the original surface coatings (Figure 3.1). For SWCNTs in media, the difference in absorbance at ~550 nm was due to the background subtraction of the pH sensitive indicator phenol red in the media. We also confirmed that SWCNTs retained their Raman signature with no increase in RBM intensity > 250 cm^{-1}

associated with SWCNT bundles and for SWCNTs-BSA maintained NIR fluorescence at ~2300 cm^{-1} in media (Figure 3.1). The lack of spectroscopic change indicated SWCNT surface coatings were stably covering the surface and limited SWCNT aggregation and settling in solution which was not observed macroscopically.

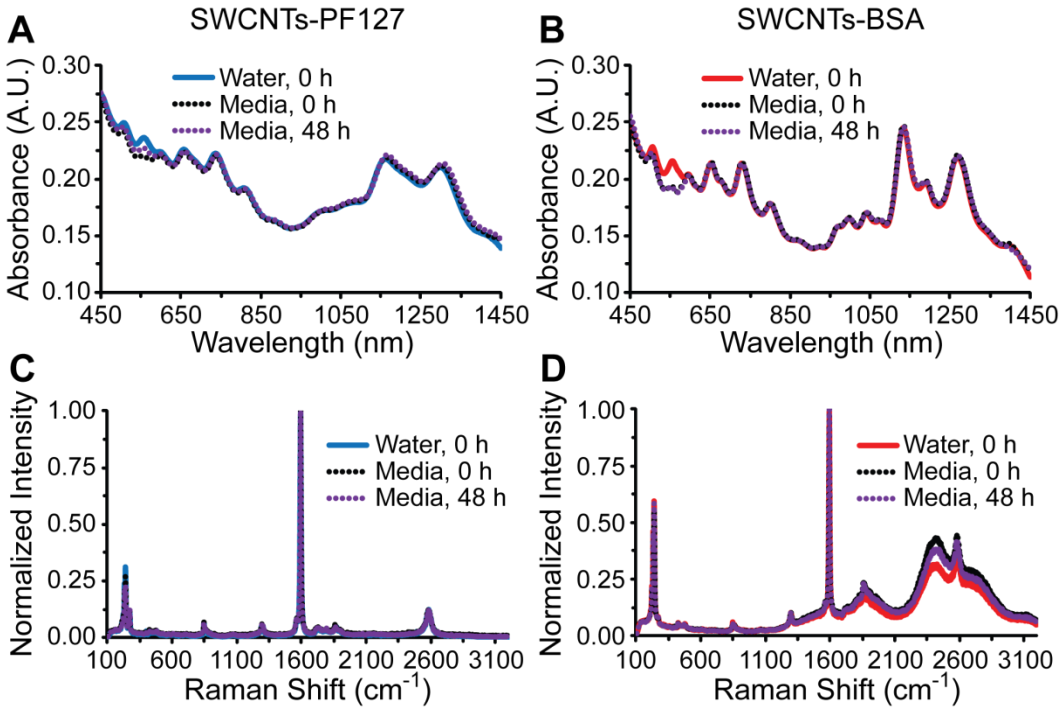

Figure 3.1: Spectroscopic analysis of SWCNT stability in complete cell culture media over 48 h. Absorbance spectra of SWCNTs-PF127 (A) and SWCNTs-BSA (B) diluted in water (solid line) and in complete cell culture media after 0 and 48 h at 37 °C (broken lines). Absorbance spectra show that distinct van Hove peaks were maintained after 48 h in cell culture media. Raman spectra of SWCNTs-PF127 (C) and SWCNTs-BSA (D) diluted in water (solid line) and in complete cell culture media after 0 and 48 h at 37 °C (broken lines), normalized to the intensity of the G-band at ~1590 cm^{-1}. Raman spectra show no change in the intensity of the D-band at ~1300 cm^{-1} associated with sp^3 carbon or RBM above 250 cm^{-1} associated with SWCNT bundles after 48 h in cell culture media.

3.3.2 Subcellular Localization of SWCNTs Inside Macrophages

We investigated the subcellular localization of SWCNTs inside macrophages with high magnification phase contrast imaging superimposed with Raman confocal imaging and spectroscopy. We used Raman spectroscopy for imaging and quantification since the Raman G-band signal of SWCNTs is linear with concentrations over several orders of magnitude[31]. Cells exposed to SWCNTs–PF127 and SWCNTs–BSA at 30 μg/mL for 48 h were fixed and imaged under phase contrast and Raman microscopy. Raman intensity maps of the G-band signal (1590 cm^{-1})[38] were taken at the midline of the cell in the same field of view and co-registered to the phase contrast images to generate a quantitative spatial distribution of SWCNT concentration inside macrophages (Figure 3.2). We observed a relatively homogeneous uptake of SWCNTs within the population of cells for each condition. Cells treated with SWCNTs–PF127 showed small pockets of concentrated subcellular localization. Cells treated with SWCNTs–BSA showed a homogeneous distribution of less concentrated uptake, but larger pockets of highly concentrated SWCNTs were also observed. With both types of surface coating, the majority of concentrated SWCNT intensities were located in the perinuclear space and regions along the cell periphery, consistent with normal cell processing from phagocytosis and pinocytosis accumulation (Figure 3.2).

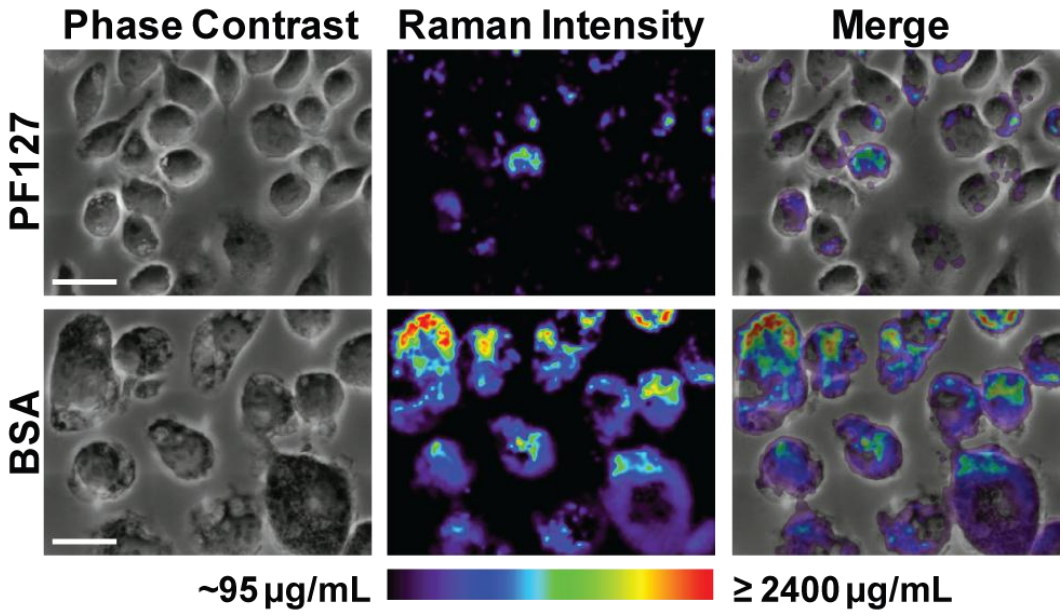

Figure 3.2: High magnification images of SWCNT uptake in macrophages. Phase contrast images were co-registered to quantitative intracellular SWCNT signal (G-band, 1590 cm^{-1}) to generate spatial maps of SWCNT uptake. Cells treated with SWCNTs–PF127 exhibited small pockets of relatively low-level uptake. Cells treated with SWCNTs–BSA showed a homogeneous distribution of low-level uptake, as well as larger pockets of high-level uptake. In both cases, the majority of concentrated SWCNT pockets were located in the perinuclear space and regions along the cell periphery. The color scale bar is the approximate local concentration of SWCNTs in the range of 95–2400 μg/mL. (Scale bar = 20 μm).

3.3.3 SWCNT Dosage and Surface Coating Alters Macrophage Morphology

Since macrophages internalized high levels of SWCNTs, possibly by compartmentalization, we examined gross changes in macrophage morphology. Bioinert SWCNTs–PF127 caused no observable changes in macrophage morphology, but bioactive SWCNTs–BSA dramatically altered cellular morphology with increasing SWCNT concentration (Figure 3.3A). At SWCNTs–BSA concentrations > 30 μg/mL, we observed distinctly phase-dense cytoplasmic

regions. To compare these morphological changes, we measured projected macrophage area with increasing amounts of SWCNTs–BSA. At SWCNTs–BSA concentrations > 30 μg/mL, we observed statistically significant, dose-dependent increases in projected cell area (Figure 2B). These phenotypic changes associated with SWCNTs–BSA were cell-type specific: fibroblasts exposed to the same range of SWCNT concentrations showed neither phase-dense cytoplasm nor dramatic size differences with exposure to SWCNTs–BSA (Figure 3.3C). Note that SWCNT uptake into epithelial and mesenchymal stem cells showed little change in cell morphology at SWCNTs–BSA concentrations up to 30 μg/mL.[22]

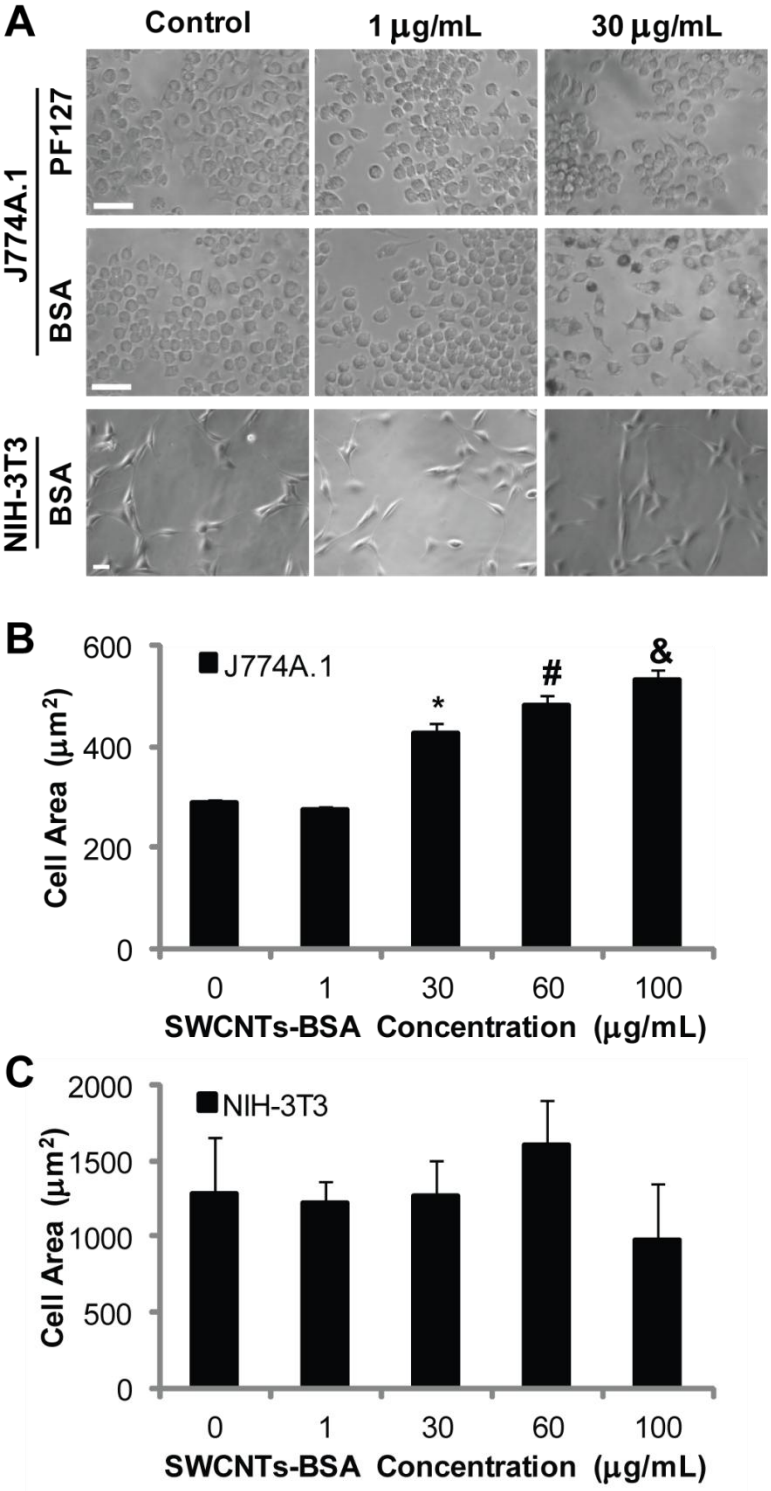

Figure 3.3: SWCNT concentration- and surface coating-dependent effects on macrophage morphology. (A) Low magnification images show a dose-dependent change in morphology with noticeable phase dense regions for

macrophages treated with SWCNTs–BSA but not SWCNTs–PF127. Fibroblasts treated with SWCNTs-BSA did not show morphology changes. (Scale bar = 50 μm). (B) Projected cell area for J774A.1 macrophages treated with SWCNTs–BSA increased with SWCNT concentration (mean ± SD, 40 cells/FOV, 2 FOV/well, 3 wells; *$p < 0.001$ compared to control, $^{\#}p < 0.05$ compared to 30 μg/mL, $^{\&}p < 0.05$ compared to 60 μg/mL). (C) Quantified cell area for NIH-3T3 fibroblasts was found to be independent of treatment with SWCNTs–BSA (mean ± SD, 20 cells/FOV, 4 FOV/well, 1 well).

3.3.4 SWCNT Dosage and Surface Coating Affect Macrophage Proliferation

Since we aim to effectively deliver SWCNTs to macrophages, we examined how SWCNTs impact macrophage viability and proliferation in addition to cell morphology. Previously, we showed that SWCNTs are not acutely toxic but significantly reduce cell proliferation.[17] Similar to morphology, we found that cell viability and proliferation were not significantly impacted at any concentration for SWCNTs–PF127 (Figure 3.4). SWCNTs–BSA statistically reduced macrophage viability, but > 95% of cells remained viable even at extremely high SWCNT concentrations (Figure 3.4A). Despite minimal effects on cell survival, SWCNTs–BSA dramatically reduced cell proliferation in a dose-dependent way at concentrations > 30 μg/mL (Figure 3.4B). The reduction in proliferation also corresponded to the increase in cell size observed for SWCNTs–BSA > 30 μg/mL (Figure 3.4). However, macrophages treated with 30 μg/mL of SWCNTs–BSA showed a much different physical morphology (Figure 3.3) and altered viability and proliferation (Figure 3.4) compared with an equivalent (100 μg/mL treatment) number of internalized SWCNTs–PF127. Macrophages may

be comparatively more sensitive to bioactive SWCNTs–BSA than SWCNTs–PF127 not only because of the greater internalized SWCNT concentration but perhaps also due to preferential receptor based uptake and subsequent cellular processing.

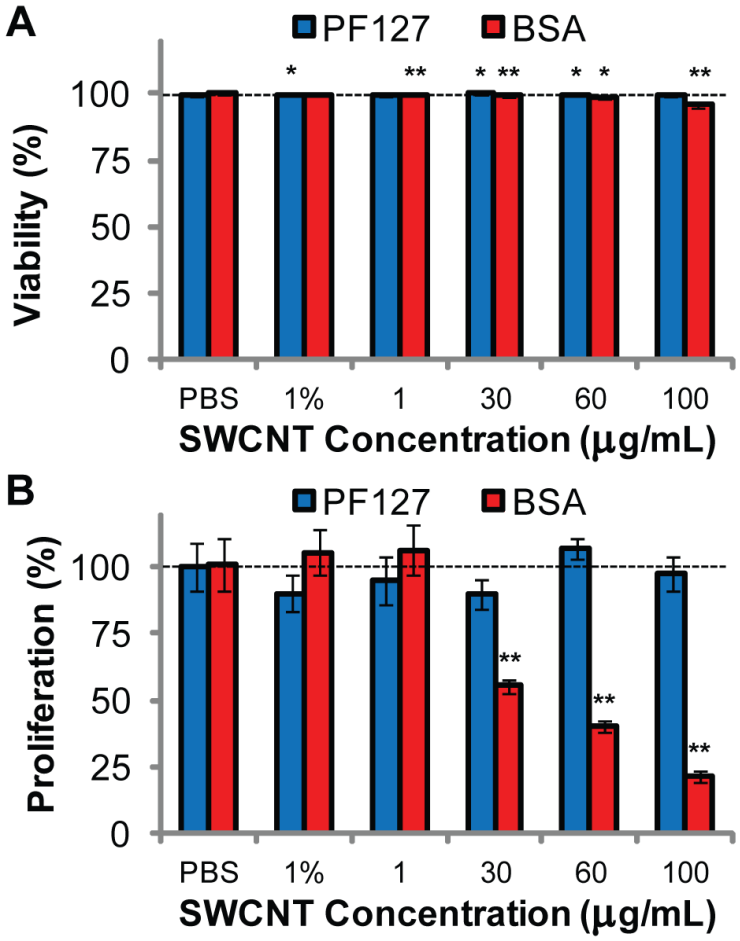

Figure 3.4: Macrophage viability and proliferation with SWCNT concentration and coating. (A) No significant reduction in viability was observed for SWCNTs–PF127, while a minor, yet statistically significant, reduction (to 95%) was observed for SWCNTs–BSA at the highest concentration. Viability was measured as the percentage of propidium iodide (PI) negative cells. (B) Macrophage proliferation remained statistically unaltered for SWCNTs–PF127 but was statistically reduced in a dose-dependent manner for high concentrations of SWCNTs–BSA. Proliferation was measured by cell enumeration and represented relative to control. Data represent mean ± SEM, >

50 cells/FOV, 10 FOV/well, 1 well; *p < 0.05, **p < 0.01 compared to PBS control.

3.3.5 Modeling of Receptor- and Membrane-Mediated Uptake *via* Modulation of SWCNT Surface Coating

We quantified SWCNT concentration inside cells using a calibration curve that relates G-band intensity of the Raman spectra at 1590 cm^{-1} to SWCNT concentration.[24] We treated cells with SWCNTs for 48 h, washed with phosphate buffered saline (PBS), lysed the cells and measured internalized and membrane-associated SWCNTs using Raman spectroscopy of the lysates. Cells treated with SWCNTs–PF127 showed increased uptake with increased exposure concentration, from 0.1 pg per cell at 1 μg/mL SWCNT to 15 pg per cell at 100 μg/mL SWCNT (Figure 3.5). Pluronics are membrane active and we have previously reported that Pluronic F127 coating increases the association of SWCNTs with cell membranes and other cell structures.[39-40] We attribute SWCNTs–PF127 internalization to association with the cell surface and express SWCNT internalization *via* membrane uptake with first order kinetics.

$$[SWCNT]_{\mathrm{int}} = K_{\mathrm{mem}}[SWCNT]_{\mathrm{ext}} \qquad (3.1)$$

$[SWCNT]_{\mathrm{int}}$ and $[SWCNT]_{\mathrm{ext}}$ are the internal and external concentration of SWCNTs, respectively, and K_{mem} has units of (pg $cell^{-1}$)/(μg mL^{-1} SWCNT). K_{mem} represents a superposition of steps including diffusion, membrane association, cell endocytosis, and other cellular processes. From data of $[SWCNT]_{\mathrm{int}}$ *versus*

$[SWCNT]_{ext}$ in Figure 3.5 and Equation 3.1, we determine K_{mem} to be 0.1 (pg cell^{-1})/(μg mL^{-1} SWCNT).

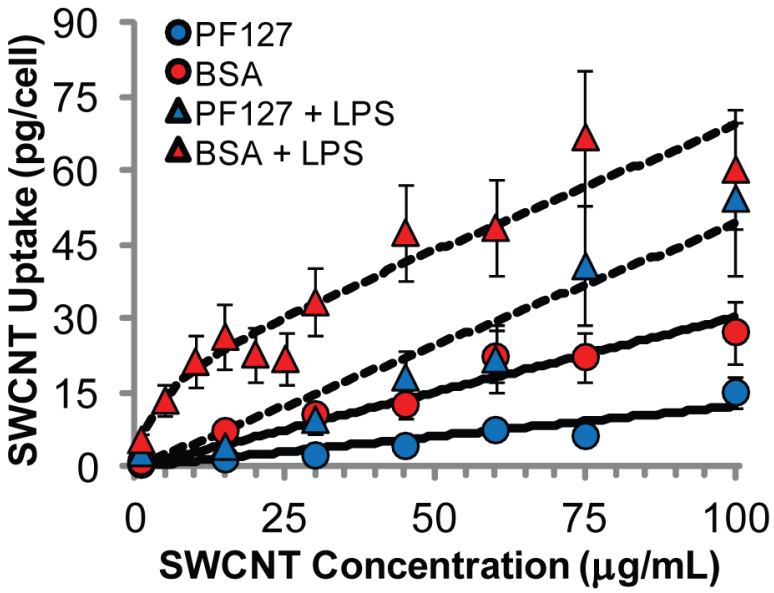

Figure 3.5: Quantified uptake per cell for macrophages with different SWCNT surface coatings and cellular activity levels. SWCNTs–BSA showed enhanced uptake per cell compared to SWCNTs–PF127. For indicated points, cells were pre-stimulated with 5 μg/mL lipopolysaccharide (LPS), which further increased uptake. Treatment of LPS stimulated macrophages with SWCNTs–BSA shows saturated uptake. Lines represent the best linear or nonlinear fits to the data (see Methods). Data represent mean ± SEM obtained through error propagation, ≥ 3 FOV/well, 3 wells.

SWCNTs–BSA showed increased cellular uptake with a maximum uptake of 27 pg per cell at 100 μg/mL (Figure 3.5). Macrophages have surface receptors designed to bind numerous proteins[41] and show affinity for albumins and albumin-coated nanomaterials.[42] We hypothesize that the protein coating on SWCNTs enhanced uptake through stimulation or interaction with cell surface receptors leading to accelerated internalization. Thus, uptake is a function of K_{mem} from above as well as a receptor mediated effect K_{rec}.

$$[SWCNT]_{\text{int}} = (K_{\text{mem}} + K_{\text{rec}})[SWCNT]_{\text{ext}} \quad (3.2)$$

K_{rec} is dependent on receptor concentration. A reasonable form for K_{rec} can be taken as $K_{rec} = K_{rec}^{0}[R]$, but K_{rec}^{0} and receptor concentration, [R], cannot be decoupled experimentally. From the data in Figure 3.5 and Equation 3.2, we determine ($K_{mem} + K_{rec}$) to be 0.3 (pg cell^{-1})/(μg mL^{-1} SWCNT), and K_{rec} = 0.2 (pg cell^{-1})/(μg mL^{-1} SWCNT). The receptor mediated uptake is double the uptake from nonspecific membrane association.

3.3.6 Modeling of Receptor- and Membrane-Mediated Uptake *via* Modulation of Macrophage Activity

Specific targeting of SWCNTs to activated M1 macrophages has many potential uses including treatment of cancer, sensing, and ablation in regions of chronic inflammation. To determine what role cell activity plays in SWCNT uptake, we stimulated macrophages with LPS, an endotoxin that specifically activates macrophages.[43] LPS induced activation of macrophages to an M1 phenotype[1] and increased pinocytosis and phagocytosis.[44-45] Macrophages were pre-stimulated with 5 μg/mL and treated with either SWCNTs–PF127 or SWCNTs–BSA.

With bioinert SWCNTs–PF127, we observed a 4–fold increase in uptake, leading to a maximum uptake of 55 pg per cell at 100 μg/mL (Figure 3.5). We attribute this increased uptake to increased pinocytosis and membrane processing,

K'_{mem}, in Equation 3.3.

$$[SWCNT]_{\mathrm{int}} = K'_{\mathrm{mem}}[SWCNT]_{\mathrm{ext}} \quad (3.3)$$

We found the experimental relation of external and internal concentration to be mostly linear, and K'_{mem} = 0.5 (pg cell^{-1})/(μg mL^{-1} SWCNT). Comparing uptake of SWCNTs–PF127 (K_{mem} versus K'_{mem}), we observed a 5–fold increase in membrane uptake with LPS stimulation. This 5–fold increase in membrane processing is consistent with previous reports of macrophage pinocytosis of small molecules such as with stimulating conditions.[44] Thus, SWCNTs–PF127 provided a good approximation of membrane-mediated uptake.

LPS-enhanced uptake of bioactive SWCNTs–BSA exhibited a substantially different trend compared to previous experiments without cell stimulation. Uptake of SWCNTs–BSA by activated macrophages was impacted by both BSA bioactivity and cell activation state at low concentrations (< 30 μg/mL) showing a 7–fold increase over SWCNTs–BSA in non-stimulated cells. However, at a dosage level > 30 μg/mL, uptake increased linearly with dosage with a similar rate to that of SWCNTs-PF127. With high levels of SWCNTs–BSA we observed a nonlinear response (Figure 3.5). This change in functional form of uptake could arise from receptor saturation. Previously, immune cell uptake of acetylated low density lipoprotein[46] and starch particles[47] also demonstrated saturation at high exposure concentrations. We modeled the receptor mediated portion of SWCNT–BSA uptake with a saturation model.

$$[SWCNT]_{\text{int}} = K'_{\text{mem}}[SWCNT]_{\text{ext}} + \frac{\alpha[SWCNT]_{\text{ext}}}{\beta+[SWCNT]_{\text{ext}}} \quad (3.4)$$

The parameters α and β reflect receptor saturation. When $[SWCNT]_{ext}$ is low, compared with levels of receptors, the $[SWCNT]_{int}$ Equation 3.4 becomes Equation 3.5.

$$[SWCNT]_{\text{int}} = (K'_{\text{mem}} + K'_{\text{rec}})[SWCNT]_{\text{ext}} \quad (3.5)$$

Below 30 μg/mL, we determined that (K'_{mem} + K'_{rec}) = 2.0 (pg cell^{-1})/(μg mL^{-1} SWCNT). From K'_{mem} = (pg cell^{-1})/(μg mL^{-1} SWCNT), we approximate K'_{rec} = 1.5 (pg cell^{-1})/(μg mL^{-1} SWCNT). Thus, in the limiting case of low SWCNT exposure concentration, the receptor-mediated processes contribute three times as much as membrane-mediated processes to overall macrophage uptake of SWCNTs, before losing effectiveness at high SWCNT exposure concentration as receptors begin to saturate. Providing these comparable quantitative parameters of cell uptake is not possible with traditional methods, such as chemical blocking of cellular processes (*e.g.*, endocytosis blocking with dynamin inhibitors). Since (i) the equilibrium coefficients are less than an order of magnitude different from one another, and (ii) SWCNTs enter cells by both non-specific membrane turnover and receptor-mediated processes, it would have been nearly impossible to decouple the quantitative effects of both with blocking.

We found that protein-coated SWCNTs entered cells using both non-specific and receptor-mediated processes; ~25 pg per cell SWCNTs–BSA was

delivered to activated macrophages with as little as 10 μg/mL extracellular concentration. When considering SWCNT size (~145 nm long), this mass correlates to more than 50 million SWCNTs per cell.[22] This same level of delivery would require ≥ 100 μg/mL SWCNTs–BSA in non-stimulated macrophages. This suggests that SWCNTs can be preferentially delivered to activated macrophages (10:1) at 10 μg/mL. Further, the apparent saturation of receptor-mediated uptake over 30 μg/mL suggests that additional SWCNTs–BSA would have little added benefit. Previous studies of SWCNT delivery to macrophages examined conditions of 5–20 μg/mL,[8,18,26] which was below the receptor threshold that we have observed.

3.3.7 Comparison of SWCNT Uptake in Fibroblasts *versus* Macrophages

We are able to show an optimal SWCNT concentration for targeting activated macrophages. Another common cell type found in niches associated with macrophages – in wound healing, inflammation, and repair – is a fibroblast. Therefore, we examined SWCNT uptake by fibroblasts using similar conditions to macrophages. The results followed the same trend observed for SWCNT uptake in macrophages; SWCNTs–BSA increased uptake 5–fold compared to SWCNTs–PF127 with maximum uptake of 3 and 14 pg per cell for SWCNTs–PF127 and SWCNTs–BSA, respectively (Figure 3.6). Generally, macrophage uptake was 5 – 10 times greater than fibroblast uptake for comparable SWCNT

dispersions. Since fibroblasts have intrinsically different sizes than macrophages, and macrophage size varies with SWCNT uptake, we considered the SWCNT uptake data with respect to projected cell area. The uptake of SWCNTs–BSA per unit area for macrophages showed a stronger concentration dependence than SWCNTs–BSA uptake for fibroblasts (~6 times greater). Taken together with the intracellular Raman maps (Figure 3.2), macrophages appear to concentrate SWCNTs–BSA within their intracellular space compared to fibroblasts. As macrophages increase their uptake per cell, not only do they become larger in size, but the larger macrophages are packed more densely with SWCNTs.

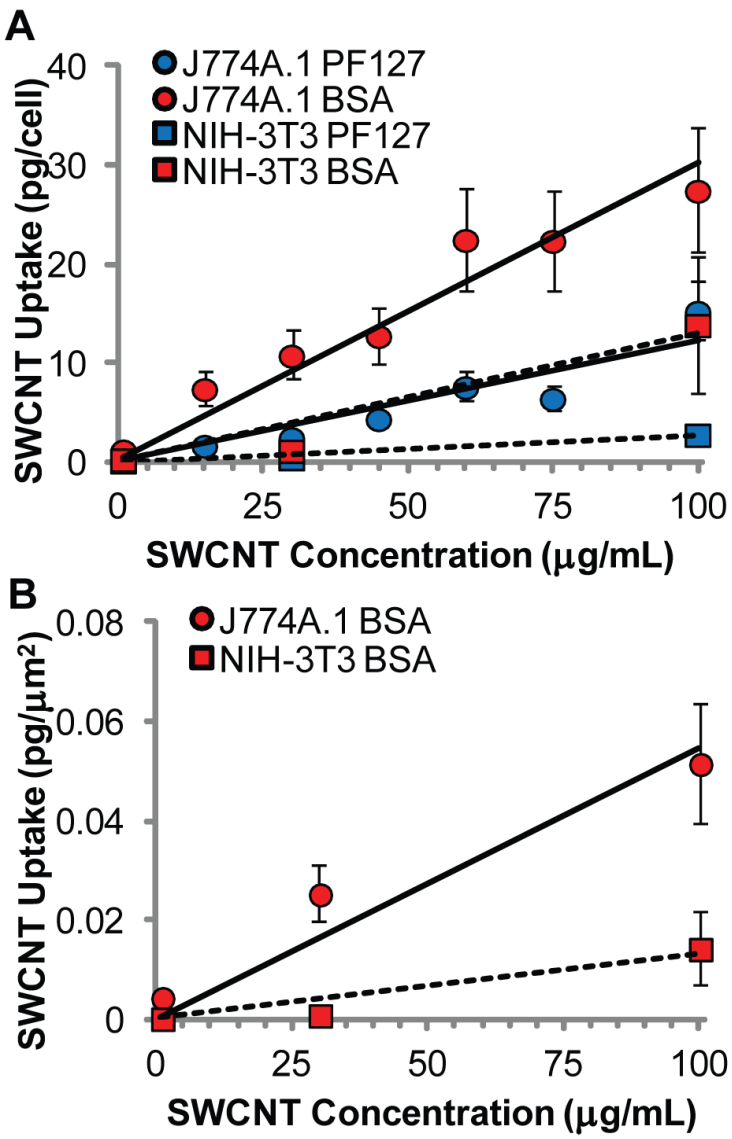

Figure 3.6: Differential surface coating mediated SWCNT uptake in J774A.1 macrophages and NIH-3T3 fibroblasts. (A) Similar to macrophages, SWCNTs–BSA showed enhanced uptake per cell compared to SWCNTs–PF127 in fibroblasts. For comparable surface coatings, macrophages showed increased uptake trends compared to fibroblasts for both PF127 and BSA coatings. (B) Concentration-dependent uptake of SWCNTs–BSA per projected cell area was enhanced for macrophages, which is more than the 2–fold enhancement observed on a per cell basis. Data represent mean ± SEM obtained through error propagation, ≥ 3 FOV/well, 3 wells.

In comparison to other published results of SWCNT uptake by

macrophage cell lines, we observe 2– to 40–fold higher uptake. While no direct comparison exists, RAW 264.7 macrophages showed slightly reduced uptake (~2–fold less) of lipid-functionalized SWCNTs than observed here.[18] Extremely long, dispersed SWCNTs (10 times longer than the ones studied here) show a 40–fold reduced uptake by J774A.1.[8] However, most studies do agree that professional phagocytes have increased nanoparticle uptake over other cells.

3.4 Conclusions

Bioactivity of the SWCNT coating and macrophage activity are both important for SWCNT uptake, but macrophage activity contributed more to levels of uptake. Even non-activated macrophages were able to internalize an order of magnitude more SWCNTs–BSA than fibroblasts, possibly by cell adaptation to engulfed materials. However, treatment concentrations > 30 μg/mL are limited, likely since cell surface receptors were saturated. At these high exposure levels, macrophages also showed altered morphology and proliferation. Thus, we suggest a high potential for selective delivery of SWCNTs to M1 activated macrophages for imaging, sensing, drug delivery and ablation.

3.5 References

1. Mantovani, A.; Sica, A.; Sozzani, S.; Allavena, P.; Vecchi, A.; Locati, M. The chemokine system in diverse forms of macrophage activation and polarization. *Trends in Immunology* **2004,** *25,* 677-686.

2. Ulbrich, W.; Lamprecht, A. Targeted drug-delivery approaches by nanoparticulate carriers in the therapy of inflammatory diseases. *Journal of the Royal Society Interface* **2010,** *7,* S55-S66.

3. Chellat, F.; Merhi, Y.; Moreau, A.; Yahia, L. H. Therapeutic potential of nanoparticulate systems for macrophage targeting. *Biomaterials* **2005,** *26,* 7260-7275.

4. Mosser, D. M.; Edwards, J. P. Exploring the full spectrum of macrophage activation. *Nature Reviews Immunology* **2008,** *8,* 958-969.

5. Kam, N. W. S.; O'Connell, M.; Wisdom, J. A.; Dai, H. Carbon nanotubes as multifunctional biological transporters and near-infrared agents for selective cancer cell destruction. *Proceedings of the National Academy of Sciences of the United States of America* **2005,** *102,* 11600-11605.

6. Madsen, S.; Baek, S.-K.; Makkouk, A.; Krasieva, T.; Hirschberg, H. Macrophages as Cell-Based Delivery Systems for Nanoshells in Photothermal Therapy. *Annals of Biomedical Engineering* **2012,** *40,* 507-515

.

7. Bianco, A.; Kostarelos, K.; Prato, M. Applications of carbon nanotubes in drug delivery. *Current Opinion in Chemical Biology* **2005,** *9,* 674-679.

8. Cherukuri, P.; Bachilo, S. M.; Litovsky, S. H.; Weisman, R. B. Near-Infrared Fluorescence Microscopy of Single-Walled Carbon Nanotubes in Phagocytic Cells. *Journal of the American Chemical Society* **2004,** *126,* 15638-15639.

9. Heller, D. A.; Baik, S.; Eurell, T. E.; Strano, M. S. Single-Walled Carbon Nanotube Spectroscopy in Live Cells: Towards Long-Term Labels and Optical Sensors. *Advanced Materials* **2005,** *17,* 2793-2799.

10. Jin, H.; Heller, D. A.; Strano, M. S. Single-Particle Tracking of Endocytosis and Exocytosis of Single-Walled Carbon Nanotubes in NIH-3T3 Cells. *Nano Letters* **2008,** *8,* 1577-1585.

11. Jin, H.; Heller, D. A.; Sharma, R.; Strano, M. S. Size-Dependent Cellular

Uptake and Expulsion of Single-Walled Carbon Nanotubes: Single Particle Tracking and a Generic Uptake Model for Nanoparticles. *ACS Nano* **2009,** *3,* 149-158.

12. Reuel, N. F.; Dupont, A.; Thouvenin, O.; Lamb, D. C.; Strano, M. S. Three-Dimensional Tracking of Carbon Nanotubes within Living Cells. *ACS Nano* **2012,** *6,* 5420-5428.

13. Heller, I.; Smaal, W. T. T.; Lemay, S. G.; Dekker, C. Probing Macrophage Activity with Carbon-Nanotube Sensors. *Small* **2009,** *5,* 2528-2532.

14. Kim, J.-H.; Heller, D. A.; Jin, H.; Barone, P. W.; Song, C.; Zhang, J.; Trudel, L. J.; Wogan, G. N.; Tannenbaum, S. R.; Strano, M. S. The rational design of nitric oxide selectivity in single-walled carbon nanotube near-infrared fluorescence sensors for biological detection. *Nature Chemistry* **2009,** *1,* 473-481.

15. O'Connell, M. J.; Bachilo, S. M.; Huffman, C. B.; Moore, V. C.; Strano, M. S.; Haroz, E. H.; Rialon, K. L.; Boul, P. J.; Noon, W. H.; Kittrell, C.; Ma, J.; Hauge, R. H.; Weisman, R. B.; Smalley, R. E. Band Gap Fluorescence from Individual Single-Walled Carbon Nanotubes. *Science* **2002,** *297,* 593-596.

16. Kaiser, J.-P.; Wick, P.; Manser, P.; Spohn, P.; Bruinink, A. Single walled carbon nanotubes (SWCNT) affect cell physiology and cell architecture. *Journal of Materials Science: Materials in Medicine* **2008,** *19,* 1523-1527.

17. Holt, B. D.; Short, P. A.; Rape, A. D.; Wang, Y.-l.; Islam, M. F.; Dahl, K. N. Carbon Nanotubes Reorganize Actin Structures in Cells and ex Vivo. *ACS Nano* **2010,** *4,* 4872-4878.

18. Konduru, N. V.; Tyurina, Y. Y.; Feng, W.; Basova, L. V.; Belikova, N. A.; Bayir, H.; Clark, K.; Rubin, M.; Stolz, D.; Vallhov, H.; Scheynius, A.; Witasp, E.; Fadeel, B.; Kichambare, P. D.; Star, A.; Kisin, E. R.; Murray, A. R.; Shvedova, A. A.; Kagan, V. E. Phosphatidylserine Targets Single-Walled Carbon Nanotubes to Professional Phagocytes in Vitro and in Vivo. *PLoS One* **2009,** *4,* e4398.

19. Zheng, M.; Jagota, A.; Semke, E. D.; Diner, B. A.; McLean, R. S.; Lustig, S. R.; Richardson, R. E.; Tassi, N. G. DNA-assisted dispersion and separation of carbon nanotubes. *Nature Materials* **2003,** *2,* 338-342.

20. Tsyboulski, D. A.; Bakota, E. L.; Witus, L. S.; Rocha, J.-D. R.; Hartgerink, J. D.; Weisman, R. B. Self-Assembling Peptide Coatings Designed for Highly Luminescent Suspension of Single-Walled Carbon

Nanotubes. *Journal of the American Chemical Society* **2008,** *130,* 17134-17140.

21. Nepal, D.; Geckeler, K. E. Proteins and Carbon Nanotubes: Close Encounter in Water. *Small* **2007,** *3,* 1259-1265.

22. Holt, B. D.; Dahl, K. N.; Islam, M. F. Quantification of Uptake and Localization of Bovine Serum Albumin-Stabilized Single-Wall Carbon Nanotubes in Different Human Cell Types. *Small* **2011,** *7,* 2348-2355.

23. Ge, C.; Du, J.; Zhao, L.; Wang, L.; Liu, Y.; Li, D.; Yang, Y.; Zhou, R.; Zhao, Y.; Chai, Z.; Chen, C. Binding of blood proteins to carbon nanotubes reduces cytotoxicity. *Proceedings of the National Academy of Sciences of the United States of America* **2011,** *108,* 16968-16973.

24. Holt, B. D.; Dahl, K. N.; Islam, M. F. Cells Take up and Recover from Protein-Stabilized Single-Wall Carbon Nanotubes with Two Distinct Rates. *ACS Nano* **2012,** *6,* 3481-3490.

25. Holt, B. D.; McCorry, M. C.; Boyer, P. D.; Dahl, K. N.; Islam, M. F. Not all protein-mediated single-wall carbon nanotube dispersions are equally bioactive. *Nanoscale* **2012,** *4,* 7425-7434.

26. dos Santos, T.; Varela, J.; Lynch, I.; Salvati, A.; Dawson, K. A. Quantitative Assessment of the Comparative Nanoparticle-Uptake Efficiency of a Range of Cell Lines. *Small* **2011,** *7,* 3341-3349.

27. Dutta, D.; Sundaram, S. K.; Teeguarden, J. G.; Riley, B. J.; Fifield, L. S.; Jacobs, J. M.; Addleman, S. R.; Kaysen, G. A.; Moudgil, B. M.; Weber, T. J. Adsorbed Proteins Influence the Biological Activity and Molecular Targeting of Nanomaterials. *Toxicological Sciences* **2007,** *100,* 303-315.

28. Dumortier, H.; Lacotte, S.; Pastorin, G.; Marega, R.; Wu, W.; Bonifazi, D.; Briand, J.-P.; Prato, M.; Muller, S.; Bianco, A. Functionalized Carbon Nanotubes Are Non-Cytotoxic and Preserve the Functionality of Primary Immune Cells. *Nano Letters* **2006,** *6,* 1522-1528.

29. Wörle-Knirsch, J. M.; Pulskamp, K.; Krug, H. F. Oops They Did It Again! Carbon Nanotubes Hoax Scientists in Viability Assays. *Nano Letters* **2006,** *6,* 1261-1268.

30. Birtwistle, M. R.; Kholodenko, B. N. Endocytosis and signalling: A meeting with mathematics. *Molecular Oncology* **2009,** *3,* 308-320.

31. Lauffenburger, D. A.; Linderman, J. J. *Receptors: Models for Binding,*

Trafficking, and Signaling. Oxford University Press: New York, 1993.

32. Johnston, D. E.; Islam, M. F.; Yodh, A. G.; Johnson, A. T. Electronic devices based on purified carbon nanotubes grown by high-pressure decomposition of carbon monoxide. *Nature Materials* **2005,** *4,* 589-592.

33. Islam, M. F.; Milkie, D. E.; Torrens, O. N.; Yodh, A. G.; Kikkawa, J. M. Magnetic heterogeneity and alignment of single wall carbon nanotubes. *Physical Review B* **2005,** *71,* 201401.

34. Islam, M. F.; Rojas, E.; Bergey, D. M.; Johnson, A. T.; Yodh, A. G. High Weight Fraction Surfactant Solubilization of Single-Wall Carbon Nanotubes in Water. *Nano Letters* **2003,** *3,* 269-273.

35. Arnold, M. S.; Green, A. A.; Hulvat, J. F.; Stupp, S. I.; Hersam, M. C. Sorting carbon nanotubes by electronic structure using density differentiation. *Nature Nanotechnology* **2006,** *1,* 60-65.

36. Fagan, J. A.; Becker, M. L.; Chun, J.; Hobbie, E. K. Length Fractionation of Carbon Nanotubes Using Centrifugation. *Advanced Materials* **2008,** *20,* 1609-1613.

37. Becker, M. L.; Fagan, J. A.; Gallant, N. D.; Bauer, B. J.; Bajpai, V.; Hobbie, E. K.; Lacerda, S. H.; Migler, K. B.; Jakupciak, J. P. Length-Dependent Uptake of DNA-Wrapped Single-Walled Carbon Nanotubes. *Advanced Materials* **2007,** *19,* 939-945.

38. Dresselhaus, M. S.; Dresselhaus, G.; Saito, R.; Jorio, A. Raman spectroscopy of carbon nanotubes. *Physics Reports* **2005,** *409,* 47-99.

39. Yaron, P. N.; Holt, B. D.; Short, P. A.; Losche, M.; Islam, M. F.; Dahl, K. N. Single wall carbon nanotubes enter cells by endocytosis and not membrane penetration. *Journal of Nanobiotechnology* **2011,** *9,* 45.

40. Holt, B. D.; Shams, H.; Horst, T. A.; Basu, S.; Rape, A. D.; Wang, Y. L.; Rohde, G. K.; Mofrad, M. R. K.; Islam, M. F.; Dahl, K. N. Altered Cell Mechanics from the Inside: Dispersed Single Wall Carbon Nanotubes Integrate with and Restructure Actin. *Journal of Functional Biomaterials* **2012,** *3,* 398-417.

41. Aderem, A.; Underhill, D. M. Mechanisms of Phagocytosis in Macrophages. *Annual Review of Immunology* **1999,** *17,* 593-623.

42. Walkey, C. D.; Chan, W. C. W. Understanding and controlling the interaction of nanomaterials with proteins in a physiological environment.

Chemical Society Reviews **2012,** *41*, 2780-2799.

43. Raetz, C. R. H.; Whitfield, C. Lipopolysaccharide Endotoxins. *Annual Review of Biochemistry* **2002,** *71,* 635-700.

44. Edelson, P. J.; Zwiebel, R.; Cohn, Z. A. The pinocytic rate of activated macrophages. *Journal of Experimental Medicine* **1975,** *142,* 1150-64.

45. Karnovsky, M. L.; Lazdins, J.; Drath, D.; Harper, A. Biochemical Characteristics of Activated Macrophages. *Annals of the New York Academy of Sciences* **1975,** *256,* 266-274.

46. Buono, C.; Anzinger, J. J.; Amar, M.; Kruth, H. S. Fluorescent pegylated nanoparticles demonstrate fluid-phase pinocytosis by macrophages in mouse atherosclerotic lesions. *Journal of Clinical Investigation* **2009,** *119,* 1373-1381.

47. Michell, R. H.; Pancake, S. J.; Noseworthy, J.; Karnovsky, M. L. Measurement of Rates of Phagocytosis. *Journal of Cell Biology* **1969,** *40,* 216-224.

4 Length Selective Delivery and Altered Subcellular Processing of Protein Stabilized Single Wall Carbon Nanotubes in Macrophages

4.1 Introduction

Understanding the uptake and intracellular distribution of nanoparticles within cells is important for controlling the rates of accumulation and delivery to specific subcellular compartments, which have direct impacts on toxicity and therapy. Various therapeutic molecules require site specific delivery within the cell, including delivery of DNA to the nucleus, trafficking to lysosomes for drug release, or escape from endosomes for protein based therapeutics.[1] Diagnostic and sensing applications not only require specific compartment delivery but also appropriate concentrations that enable detection without inducing toxicity.[2] Single wall carbon nanotubes (SWCNTs) have received much attention as subcellular nanoparticles due to their low toxicity, small size, and ability to easily cross cellular membranes. SWCNTs also have high specific surface area for delivery as well as unique electrical, optical, thermal, and mechanical properties[3] which have motivated their use as subcellular sensors,[4] cellular labels,[5] and in photothermal ablation.[6]

Immune cells, in particular macrophages, have emerged as attractive targets for subcellular nanoparticle and SWCNT delivery. Macrophages are involved in many physiological and pathological conditions including wound

healing, inflammation, and cancer, thus motivating a broad interest in modulating and tracking macrophages for therapy and diagnosis.[7-8] As such, the subcellular distribution, functional state, and residence time of SWCNTs in macrophages are important parameters to establish. For other cell types including fibroblasts, individual SWCNTs of varying lengths have been observed to enter cells and were subsequently expelled at later times.[9-10] Aggregated SWCNTs, on the other hand, were observed to remain in murine myoblast stem cells after 3 months.[11] However for macrophages, which take up significantly more SWCNTs than other cell types,[12] it is unclear how the physical properties of SWCNTs or the cell specific processing of macrophages affect the subcellular distribution, and importantly the aggregation state of SWCNTs within the cell.

The specific subcellular trafficking and ultimate fate of internalized nanoparticles is largely determined by the mechanism of cellular entry.[13-14] In addition to specific associations with cell membrane components, uptake mechanisms are highly size dependent.[15] Macrophages are capable of two size dependent entry mechanisms: endocytosis of small (< 200 nm) material and specialized phagocytosis of large (> 500 nm) particles. To investigate the subcellular distribution and aggregation state of SWCNTs in macrophages internalized through these mechanisms, we prepared dispersions of two different length SWCNTs. In order to maintain SWCNT optical properties and promote cellular uptake into macrophages, we non-covalently dispersed SWCNTs with bovine serum albumin (BSA).[9, 12, 16-17] We also compared the subcellular

distribution in macrophages to fibroblasts to determine the effects of immune cell specific processes.

Using Raman spectroscopy, we quantify cellular uptake as well as track the intracellular state of SWCNTs as a function of length in macrophages. We find that bulk uptake in cells decreases with increasing SWCNT length, but selectivity for macrophages enhances. For macrophages, short SWCNTs were highly bundled and located in concentrated phase dense regions, whereas longer SWCNTs forced to enter through phagocytosis remained relatively isolated with preserved SWCNT properties. Macrophages also showed increased SWCNT bundling compared to fibroblasts, which were found to release a larger percentage of their internalized SWCNTs over time compared to macrophages. Taken together, the results suggest both macrophage cellular processes and the short length of SWCNTs facilitate high subcellular concentrations in macrophages that are more bundled and less likely to release from macrophages than from fibroblasts. This differential cellular processing further suggests that macrophages may be used in novel applications such as live cell carriers of SWCNTs into tumors and regions of inflammation for therapy and imaging.

4.2 Materials and Methods

4.2.1 SWCNT Dispersions

Long length SWCNTs-BSA dispersions were prepared from unpurified high pressure carbon monoxide conversion synthesis (HiPCO) SWCNTs (Carbon Nanotechnologies, Inc.) with diameters of 1 ± 0.3 nm and polydisperse lengths.

As produced HiPCO SWCNTs contain a wide distribution of lengths with many SWCNTs > 500 nm. Dispersions of individual SWCNTs preserving longer lengths were produced following similar methods previously reported for other surfactant dispersing agents that resulted in SWCNTs > 1 μm in length.[18] ~87 mg of hydrated SWCNT powder (~2.2 mg dry mass equivalent) was dissolved in 2.2 mL of 10 wt% BSA (Sigma-Aldrich) solution in ultrapure deionized water and exposed to 30 min of low power, high frequency (12 W, 55 kHz) bath sonication (Cole-Parmer Ultrasonic Cleaner). Long SWCNTs-BSA suspensions were mildly centrifuged for 30 min at 10,000×*g* to remove large SWCNT aggregates.

Short length SWCNTs-BSA dispersions were prepared using purified and length fractionated SWCNTs from the same synthesis batch. The purification and length fractionation procedures, described previously in greater detail,[19-24] resulted in a SWCNT sample containing < 5 wt% carbonaceous impurities and ~0.3 wt% metallic impurities[19-20] with lengths of 145 ± 17 nm.[21-24] Short SWCNTs were dispersed at 0.1 wt% in 1.0 wt% BSA *via* high power, low frequency probe-tip sonication (Fisher Scientific, Model 100; 3 mm tip diameter) at 6 W for 2 hours. Under these conditions, the ~150 nm SWCNTs were not shortened from sonication induced scission.[25] To separate bundles from isolated SWCNTs, suspensions were centrifuged at 21,000×*g* for 7 minutes (Beckman Coulter Allegra 25R Centrifuge with a TA-15-1.5 rotor). For both long and short SWCNTs-BSA, the supernatant after centrifugation was collected and sterilized under UV light for 1 h prior to cell experiments.

4.2.2 SWCNT Dispersion Characterization

UV-vis-NIR absorbance spectroscopy: To quantitatively determine SWCNT concentration and qualitatively assess dispersion quality, SWCNT dispersions were examined using UV-vis-NIR absorbance spectroscopy (Varian Cary 5000 UV-vis-NIR spectrophotometer). Concentration was determined using an extinction coefficient of 2.6 (absorbance mL)/(mg mm) at 930 nm.[24] The stability of long SWCNTs-BSA dispersion in ultrapure deionized water was monitored over 3 months using absorbance spectroscopy by quantifying the peak width at half max of the van Hove peaks in the NIR region.

Raman spectroscopy: SWCNT structure after dispersion and initial aggregation state in solution were characterized with Raman spectroscopy. Samples diluted to ~0.1 absorbance/cm in water were analyzed on an inverted, inVia confocal Raman microscope (Renishaw) using a 50× air objective with 0.75 numerical aperture (NA) and a 785 nm laser (100 mW). Spectra were acquired between 100 – 3200 cm^{-1}. Each Raman spectrum was normalized to the G-band intensity. The D-band-to-G-band intensity ratio (I_D:I_G) was calculated by dividing the D-band intensity at ~1300 cm^{-1} by the G-band intensity.

NIR fluorescence spectroscopy: SWCNT dispersion quality was characterized with NIR fluorescence spectroscopy (Horiba Jobin Yvon Nanolog spectrofluorometer). SWCNT samples were diluted to ~0.1 absorbance/cm in water and NIR fluorescence spectra were collected at 60 s integration time with excitation and emission slit widths of 10 nm using a liquid nitrogen cooled detector (Symphony InGaAs-1700). The excitation grating was 1200 grooves/mm

and blazed at 500 nm and the emission grating was 150 grooves/mm and blazed at 1200 nm. A NIR fluorescence heat map of corrected fluorescence intensity normalized to excitation intensity was constructed using FluorEscence and Nanosizer software with chirality peak fits generated using a Voight 2D model. SWCNT quantum yield (QY) was determined at 785 nm. The total corrected SWCNT NIR fluorescence signal per absorbance was normalized to fluorescence per absorbance of NIR dye indocyanine green with known quantum efficiency and the same system parameters.

4.2.3 Cell Culture and Treatment

J774A.1 mouse macrophage-like cells (ATCC) were cultured in Dulbecco's Modified Eagle's Medium (DMEM; 4500 mg/L glucose, 4.0 mM L-glutamine, without sodium pyruvate; Thermo Scientific Hyclone), supplemented with 10% v/v fetal bovine serum (FBS; Invitrogen) and 1% v/v penicillin-streptomycin (P/S; Invitrogen). NIH-3T3 mouse fibroblast cells were cultured in similar medium, except with newborn calf serum (CS; Invitrogen) instead of FBS. HeLa cells were cultured in DMEM (1000 mg/L glucose, 4.0 mM L-glutamine, with 110 mg/L sodium pyruvate; Thermo Scientific Hyclone), supplemented with 10% v/v FBS (Invitrogen) and 1% v/v P/S (Invitrogen). Cells were maintained at 37 °C and 5% CO_2.

SWCNT Uptake per Cell: For bulk uptake measurements, J774A.1 cells were seeded at 2×10^4 cell/cm^2 or HeLa and NIH-3T3 cells were seeded at 3×10^4 cells/cm^2 into 24-well plates and maintained in culture for 24 h. Short or long

SWCNTs-BSA were diluted to a final concentration of 1 μg/mL in fresh media and cells were exposed for 48 h. Each treatment was performed in duplicate. Exposure media was removed and cells were gently washed once in PBS. Fresh pH independent media without phenol red was added, and cells were labeled with Hoechst 33342 and propidium iodide (PI) for quantification of proliferation and viability. Images were taken for ≥ 5 fields of view of ~0.4 mm^2 each on a Leica DMI 6000B inverted light and fluorescence microscope maintained at 37 °C with a 20× (0.4 NA) air objective. Nuclei were segmented and counted in ImageJ and the average cell density was extrapolated to determine the cells per well for uptake normalization.

SWCNT Subcellular Imaging: For subcellular Raman mapping measurements J774A.1 cells were seeded at 1×10^4 cell/cm^2 or NIH-3T3 cells were seeded at 3×10^4 cells/cm^2 onto sterilized #1.5 coverslips and maintained in culture for 24 h. For length dependent processing comparisons in macrophages, short or long SWCNTs-BSA were diluted to a final concentration of 10 μg/mL in fresh media, and cells were exposed for 48 h. For cell type dependent processing comparisons in fibroblasts and macrophages, short SWCNTs-BSA were diluted to a final concentration of 30 μg/mL in fresh media, and cells were exposed for 24 h. For recovery conditions, fibroblasts were subcultured and re-seeded in fresh media for 24 h. For macrophage recovery, treatment media was removed, exchanged for fresh media, and cells were maintained in culture for an additional 24 h. At the completion of cell exposure or recovery, media was removed and

cells were washed 3 times in PBS and fixed with 3.7% v/v formaldehyde (Sigma-Aldrich) for 15 min and mounted onto glass slides.

4.2.4 Quantification of SWCNT Uptake

Cells were lysed using a combination of Triton X-100 and one freeze thaw cycle and were probe-tip sonicated for ~10 seconds at 6 W (Fisher Scientific, Model 100; 3 mm tip diameter). Cellular lysate solutions were then pipette into 24-well MatTek #1.5 glass bottom plates and subjected to confocal Raman spectroscopy (inVia Raman microscope, Renishaw) using a 785 nm laser with a 50× (0.75 NA), air immersion objective. SWCNT concentration was determined from the height of the G-band above baseline using a standard concentration curve relating G-band intensity to SWCNT concentration determined *via* UV-vis-NIR absorbance spectroscopy for either short or long SWCNTs-BSA (Figure 4.1).

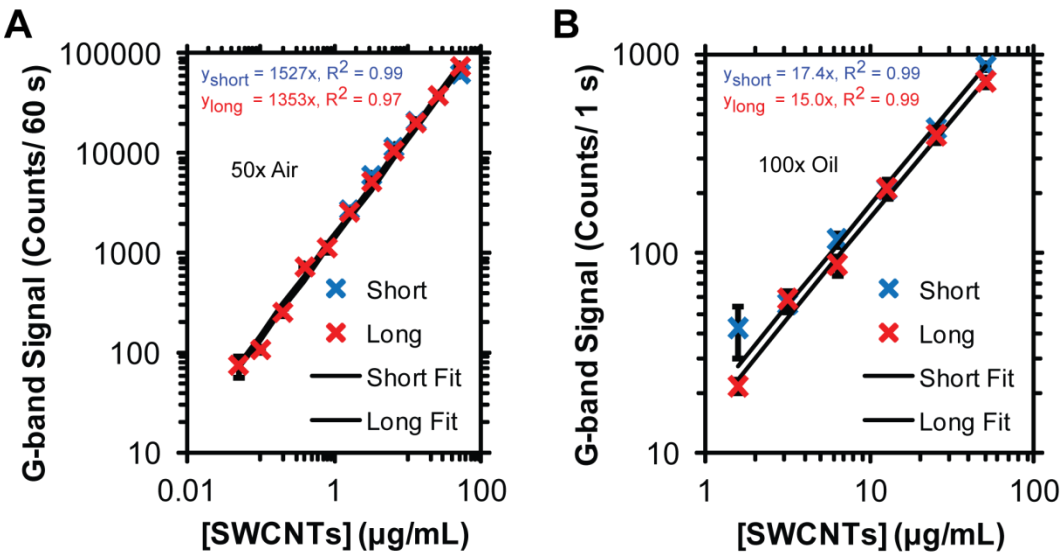

Figure 4.1: Raman spectroscopy standard curves. Standard curve relates SWCNTs Raman G-band height above the baseline to concentration for 50× (0.75 NA), air immersion objective used for solutions (A), and 100× (1.4 NA) oil immersion objective used for Raman mapping experiments (B). The highest concentration sample was made by diluting SWCNT stock dispersion with known concentration from UV-vis-NIR absorbance spectroscopy. The sample was serially diluted, and Raman spectroscopy was performed on each diluted sample with the indicated integration times. The G-band signal was linear with SWCNT concentration over the indicated concentration ranges. Reproducibility of G-band counts measurements were insured by calibrating to the same silicon standard wafer before each experiment. Data = mean ± SEM from ≥ 5 acquisitions.

4.2.5 Subcellular Raman Spectroscopy Mapping

Phase contrast imaging and Raman spectroscopy mapping were performed on an inverted, inVia confocal Raman microscope (Renishaw) using a 0.9 NA air condenser, a 100× (1.4 NA) oil immersion objective, and a 785 nm laser (100 mW). Control of mapping parameters and imaging processing were performed using WiRE software (Renishaw). For Raman mapping, Raman spectra were acquired with an X–Y step size ≤ 1.4 µm for single cell images and ≤ 3.0 µm for multi-cell fields of view. Excitation laser power of 5% was used to prevent

sample degradation and ensure accurate bundle fraction quantification. Spectra corresponding to the G-band, radial breathing modes (RBMs), and NIR fluorescence region were taken sequentially over the same X–Y coordinates all with integration times of 2 s. For G-band, spectra between 1188 – 1696 cm^{-1} (centered at 1450 cm^{-1}) were collected with 0.88cm^{-1} resolution. For RBMs, spectra between 27 – 650 cm^{-1} (centered at 350 cm^{-1}) were collected with 1.08cm^{-1} resolution. For NIR fluorescence, spectra between 2238 – 2659 cm^{-1} (centered at 2450 cm^{-1}) were collected with 0.71cm^{-1} resolution.

4.2.6 Spatial Maps and Quantification

Spatial maps of the G-band intensity, bundle fraction, and NIR fluorescence were performed in MATLAB (MathWorks). The maximum G-band intensity between 1540 – 1610 cm^{-1}, maximum individual RBM intensity between 200 – 250 cm^{-1}, and maximum bundle RBM intensity between 250 – 285 cm^{-1} above the baseline in the respective regions were calculated for each data pixel. For NIR fluorescence, integrated area under the spectral curve between 2238 – 2659 cm^{-1} was tabulated. Bundle fraction was quantified by normalizing the maximum bundle RBM intensity by the sum of maximum individual and maximum bundle RBM intensity. NIR fluorescence was quantified by normalizing the integrated area by the G-band intensity. Local SWCNT concentration was determined using a calibration curve relating G-band intensity to SWCNT concentration determined *via* UV-vis-NIR absorbance spectroscopy for short SWCNTs-BSA and long SWCNTs-BSA (Figure 4.1). Spectra with G-

band signal-to-noise ratio < 3 were excluded from the analysis. Subcellular phase dense regions of interest were manually segmented in ImageJ and the corresponding individual and bundle RBM intensities within the segmented region were quantified.

4.3 Results and Discussion

4.3.1 Long SWCNTs are Individually Dispersed by BSA

We have previously worked with SWCNTs that were purified and length fractionated to 145 ± 17 nm to promote cell uptake.[26-28] To develop comparable SWCNT dispersions with longer lengths, we used the same synthesized batch of SWCNTs in their as-received state before our additional in-house purification and length fractionation. The HiPCO synthesis of SWCNTs is known to produce nanotubes with polydisperse lengths ranging from tens of nm to several μm.[29] To stably disperse SWCNTs into solution while maintaining their length, we used a low power, high frequency bath sonication in the presence of BSA, similar to other approaches used to produce high length (> 1 μm) dispersions with other surfactant molecules.[18] We characterized the dispersion quality of long SWCNTs-BSA and compared to our length fractioned short SWCNTs-BSA using UV-vis-NIR absorbance, Raman, and NIR fluorescence spectroscopy.

Both short and long SWCNTs-BSA showed similar dispersion quality with sharp peaks in absorbance which arise from van Hove singularities, indicating the presence of individually dispersed SWCNTs (Figure 4.2A).[30] We

determined the concentration of dispersed SWCNTs using a known absorption coefficient at 930 nm.[24] For short SWCNTs-BSA, we obtained ~30% mass yield for the chosen dispersion parameters. By comparison, long SWCNTs-BSA had a slightly higher dispersion concentration but were also prepared with different sonication and centrifugation procedures to aid in the preservation of longer SWCNTs (see Methods). The increased absorbance may also reflect an additional contribution from amorphous carbon which was removed during the purification step for short SWCNTs-BSA dispersions. We further determined long SWCNTs-BSA dispersions were stable in water for > 3 months, evidenced by no flocculation induced concentration changes or broadening of van Hove peaks in NIR absorbance (Figure 4.3).

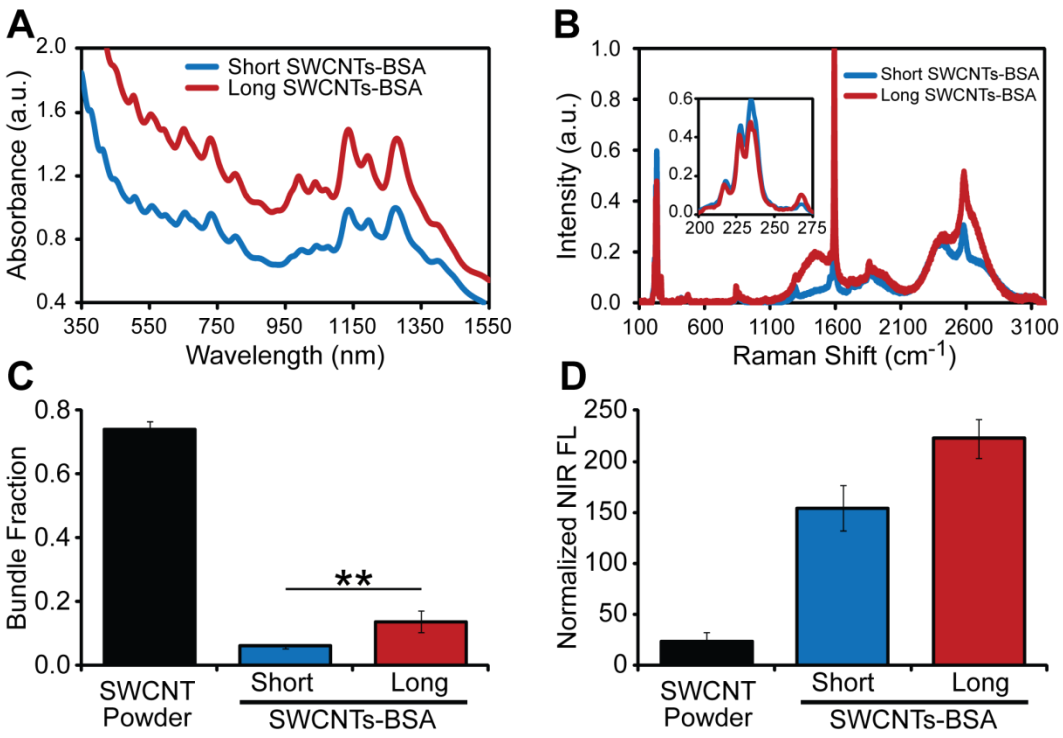

Figure 4.2: Optical characterization and quantification of the aggregation state of length fractionated (short) SWCNTs-BSA and RAW HiPCO (long) SWCNTs-BSA. (A) UV-vis-NIR absorbance spectroscopy of short and long SWCNTs-BSA shows sharp van Hove peaks in absorbance indicative of individually dispersed SWCNTs. (B) Raman spectroscopy of SWCNT dispersions confirms SWCNT structure is maintained with small I_D:I_G ratio. The inset magnifies the radial breathing modes (RBMs) between 200 – 275 cm^{-1} which are sensitive to the aggregation state of SWCNTs. The broad peaks between ~1100 – 3100 cm^{-1} result from unfiltered real space SWCNT fluorescence detected on the system. (C) Quantification of RBM bundle fraction relates resonance Raman intensity of individual SWCNTs < 250 cm^{-1} to bundled SWCNTs > 250 cm^{-1} for E_{laser} = 1.58 eV (785 nm). Both short and long SWCNTs-BSA dispersions have significantly lower bundle fractions than undispersed SWCNT powder ($p < 0.001$). The gentle dispersion with long SWCNTs results in a significantly higher bundle fraction than short SWCNTs (**$p < 0.01$). (D) Quantification of NIR fluorescence intensity between ~2240 – 2660 cm^{-1} resulting from individual SWCNTs normalized to the G-band height. Both dispersions have significantly greater NIR fluorescence than SWCNT powder ($p < 0.05$), and despite the increased bundle fraction, long SWCNTs-BSA show increased NIR fluorescence intensity compared to short SWCNTs. Data = mean ± SEM from ≥ 2 acquisitions.

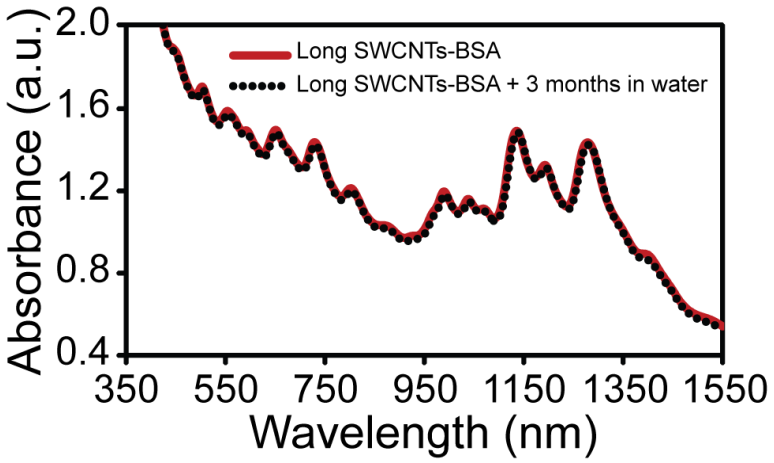

Figure 4.3: Long SWCNTs-BSA stability in water characterized with absorbance spectroscopy. UV-vis-NIR absorbance spectroscopy shows indistinguishable spectra with no concentration loss or peak broadening at the dispersion yield concentration for 3 months.

We performed Raman spectroscopy to further characterize dispersion quality and the initial aggregation state of SWCNTs using characteristic Raman features of SWCNTs including the G-band at ~1590 cm^{-1} for sp^2-hybridized carbon, D-band at ~1300 cm^{-1} for sp^3-hybridized carbon, and radial breathing modes (RBMs) between ~200 – 275 cm^{-1} (Figure 4.2B).[31] Both short and long SWCNTs-BSA showed low D-band intensity relative to G-band intensity (I_D:I_G ~ 0.03) similar to the starting SWCNT powder, indicating that neither sonication procedure significantly altered SWCNT structure. The RBMs arise from vibrations along the SWCNT radius and as such, the corresponding Raman shift is different for each species, or (n,m) chirality of SWCNT.[31] Further, the RBMs which are detected depends on whether the unique electronic transition of a particular chirality is in resonance with the excitation laser. For the distribution of HiPCO SWCNTs in our dispersions with the 785 nm (E_{laser} = 1.58 eV) used here,

only individual nanotubes with RBMs < 250 cm^{-1} are in resonance and appreciably detectable.[32-33] However, if nanotubes are aggregated in bundles, the electronic transitions of bundled nanotubes have been shown to red-shift and broaden, thus bringing the bundled nanotubes with RBMs > 250 cm^{-1} into resonance.[32-33] Specifically, this happens for the (10,2) nanotube with RBM ~ 267 cm^{-1} which is only detected if SWCNTs are bundled.[32-33] Therefore, to determine the level of aggregation or amount of bundling, we quantified the intensity percentage of the bundle RBM at ~ 267 cm^{-1} relative to the max individual RBM intensity < 250 cm^{-1} (typically at ~234 cm^{-1}), *i.e.,* bundle fraction = $I_{RBM@267}/(I_{RBM@234} + I_{RBM@267})$. For both short and long SWCNTs-BSA, we confirmed that dispersion with BSA significantly reduced the bundle fraction of starting SWCNT power by ~5 – 10 times (Figure 4.2C). Dispersions of long SWCNTs-BSA had ~2 times higher bundle fraction compared with short SWCNTs-BSA. The difference may be due to the gentler sonication and centrifugation procedure used to preserve SWCNT length which likely allowed for a greater persistence of small bundles in the sample.

Complimentary to bundle fraction is SWCNT NIR fluorescence, which arises only from non-bundled SWCNTs.[30] We detected the presence of unfiltered real space NIR fluorescence on our Raman system in the form of broad peaks at ~1450, ~1920, ~2430, and ~2610 cm^{-1} resulting from individual SWCNTs. We quantified integrated NIR fluorescence signal between ~2240 – 2660 cm^{-1} normalized to the G-band intensity. Both short and long SWCNTs-BSA dispersions had significantly greater NIR fluorescence than heavily bundled

SWCNT powder (Figure 4.2D). Despite the increased bundle fraction, long SWCNTs-BSA showed increased NIR fluorescence intensity compared to short SWCNTs, likely due to the presence of SWCNTs with longer lengths.[34]

4.3.2 Long SWCNTs-BSA Dispersions Contain High Length SWCNTs with Increased Quantum Yield

The quantum efficiency of SWCNTs is known to strongly depend on their length.[34] For pristine SWCNTs, the main non-radiative decay mechanism is believed to be exciton diffusion to quenching sites consisting of sp^3-hybridized defects, adsorbed molecules, or ends of nanotubes themselves.[35-36] The probability of diffusion to a quenching site within the lifetime of an exciton decreases with increasing SWCNT length resulting in more fluorescence emission events. To verify our long SWCNTs-BSA dispersion prepared from as-received SWCNTs contained nanotubes with longer lengths, we used NIR fluorescence spectroscopy to determine the relative change in quantum yield (QY) compared to our length-fractionated short SWCNTs-BSA dispersion. Individually dispersed semiconducting SWCNTs fluoresce at distinct wavelengths in the NIR corresponding to the unique electronic transition energies of each different SWCNT chirality,[37] whereas bundles containing metallic nanotubes quench inherent SWCNT fluorescence.[30] The NIR fluorescence spectroscopy two-dimensional excitation-emission heat map shows NIR fluorescence intensity from many different SWCNT chiralities, confirming the presence of individual SWCNTs in the long SWCNTs-BSA dispersion (Figure 4.4A). We further

determined a quantum yield (QY) of ~0.082% for long SWCNTs-BSA, which was ~6 times greater than the QY of ~0.014% for short SWCNTs-BSA dispersed with the same BSA protein concentration (Figure 4.4B). The substantial increase in QY suggests the long SWCNTs-BSA dispersion contained a distribution of SWCNTs with longer lengths on average. We also verified that dispersion *via* low power bath sonication preserved longer SWCNT lengths by directly comparing methods with the high power probe-tip sonication used to disperse short SWCNTs. High power dispersion of the as-received SWCNTs resulted in a ~35% reduced QY of ~0.053%, likely from sonication induced cutting of the long length SWCNTs.

Theoretical predictions which incorporate diffusional quenching only at the ends of nanotubes approximate QY scales with L^2, were L is the length of the nanotube.[36] Based on this approximation, we determined long SWCNTs-BSA contain a distribution of SWCNTs with longer lengths with an average length of ~355 nm. This likely represents a lower estimate since other quenching effects including defects were ignored. Furthermore, we performed NIR fluorescence imaging of dilute long SWCNTs-BSA dispersions immobilized in agar. SWCNT structures with lengths of ~1 μm or greater were visible confirming that the distribution of nanotubes in long SWCNTs-BSA, in addition to being at least ~2.5 times longer on average, also contains SWCNTs with significantly longer lengths (Figure 4.4C).

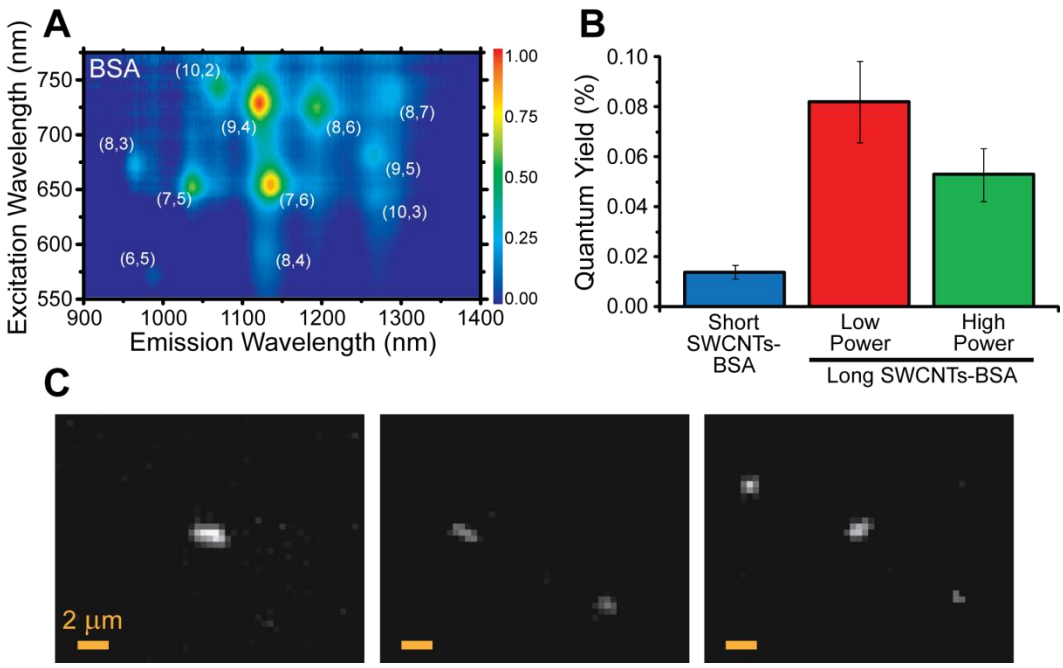

Figure 4.4: NIR fluorescence characterization of long SWCNTs-BSA quantum yield (QY) and length. (A) NIR fluorescence spectroscopy heat map shows SWCNT fluorescence intensity confirming the presence of individual SWCNTs of many different chiralities. The dynamic range is scaled to the max NIR fluorescence intensity. (B) Quantification of long SWCNTs-BSA QY shows significant increase compared to short SWCNTs-BSA when prepared with a low power bath sonication to preserve SWCNT length. High power probe tip sonication artificially shortens SWCNTs and reduces QY. (C) NIR fluorescence images of long SWCNTs-BSA immobilized in agar shows individual SWCNTs with lengths exceeding 1 μm. Data = mean ± SD.

4.3.3 Differential Cellular Uptake of Long SWCNTs-BSA

We compared the uptake of short and long SWCNTs-BSA in multiple cell types with different cell internalization mechanisms. HeLa cells and NIH-3T3 fibroblasts are primarily active in small sized endocytosis mechanisms which typically have upper physical limits of ~200 nm due to the size of clathrin or caveolin vesicles[14]. Macrophages are active in endocytosis as well as specialized phagocytosis for internalization of particles > 1 μm. To quantify cellular uptake,

we exposed cells to SWCNTs for 48 h and subsequently quantified internalized and membrane associated SWCNTs of the cell lysates using Raman spectroscopy with a calibration curve relating G-band intensity to SWCNT concentration (Figure 4.1). For exposure to 1 μg/mL of short SWCNTs-BSA we observed the highest uptake by macrophages followed closely by fibroblasts and lower uptake by HeLa cells (Figure 4.5A). Exposure to equal concentrations of long SWCNTs-BSA resulted in a reduction in uptake for all cell types (Figure 4.5B). However, uptake was reduced more for endocytosis dependent HeLa cells and fibroblasts relative to macrophages, resulting in a ~2 times increase in macrophage selectivity. We did observe non-negligible uptake of long SWCNTs-BSA for both HeLa cells and fibroblasts. While many studies have determined optimal nanoparticle uptake sizes < 200 nm, including 50 nm for gold nanoparticles in HeLa cells,[38] other recent studies in NIH-3T3 fibroblasts showed internalization of DNA dispersed SWCNTs with lengths ranging 130 – 660 nm and maximum uptake rate for 320 nm due to clustering of cell surface receptors.[10] Thus, we cannot neglect the contribution of uptake process including macropinocytosis[14] or even large caveolin vesicles.[15] Further, the long SWCNTs-BSA sample also contains polydisperse lengths including the ~150 nm SWCNTs that were length fractionated to generate the short SWCNTs-BSA sample.

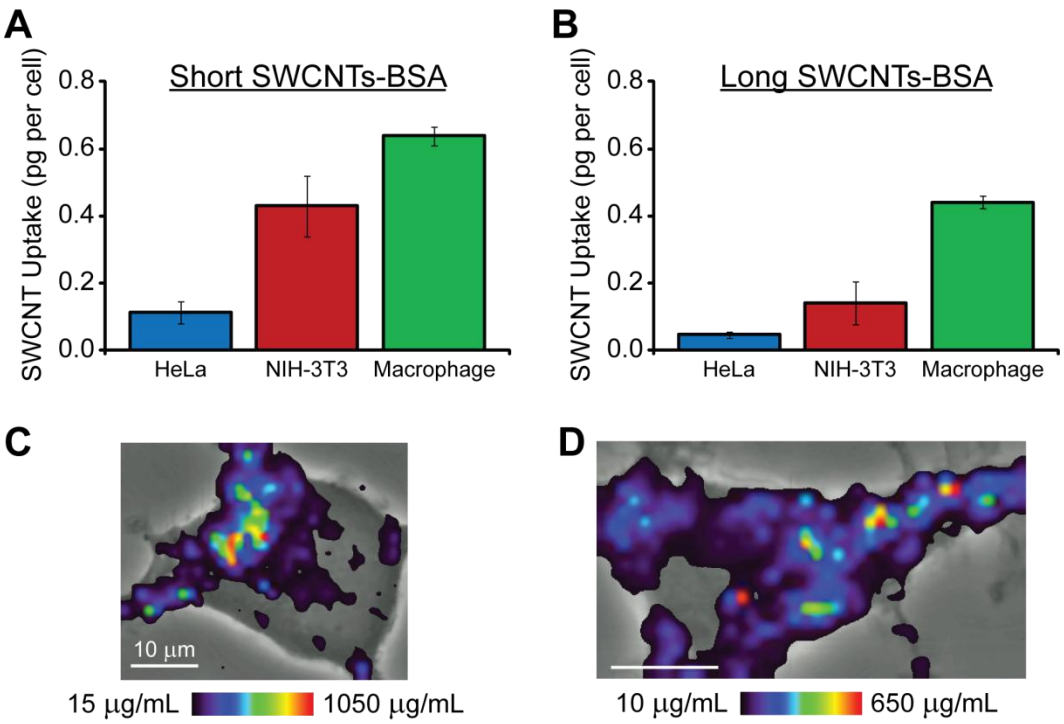

Figure 4.5: Uptake comparison of short and long SWCNTs-BSA in multiple cell types. (A) Average mass of short SWCNTs internalized per cell quantified using Raman spectroscopy shows slightly higher uptake for macrophages compared to NIH-3T3 fibroblasts. (B) Uptake of long SWCNTs-BSA decreases for each cell type, but less so for macrophages resulting in increased selectively compared to short SWCNTs-BSA. For uptake measurements, cells were exposed to 1 μg/mL SWCNTs-BSA. Data = mean ± SEM from 2 replicate experiments. Raman spectroscopy spatial maps of SWCNT intensity in macrophages for short (C) and long (D) SWCNTs-BSA shows subcellular concentrations at 50 – 100 times greater than the 10 μg/mL exposure concentration.

We further compared the subcellular distribution and concentration of short and long SWCNTs-BSA exposed to macrophages at 10 μg/mL. Raman spectroscopy maps of intracellular SWCNT concentration revealed regions as high as 100 times and 50 times more locally concentrated than the exposure dosage for short and long SWCNTs-BSA, respectively (Figure 4.5C-D). The extent of increased concentration within macrophages, particularly for short

SWCNTs-BSA, suggests that increased uptake is driven by efficient entry and subcellular processing though endocytosis. We hypothesized this process might occur though cell specific processes to aggregate SWCNTs.

4.3.4 Macrophages Selectively Bundle Short SWCNTs-BSA

To determine the effects of SWCNT length on subcellular distribution and aggregation state within macrophages, we performed Raman spectroscopy maps over several individual cells exposed to 10 μg/mL short or long SWCNTs-BSA. Each pixel within the maps contained data from Raman spectra relating SWCNT concentration with G-band, SWCNT aggregation state with RBMs, and the presence of individual SWCNTs through NIR fluorescence (Figure 4.6A). Exposure to both short and long SWCNTs-BSA resulted in subcellular regions with markedly increased concentrations of SWCNTs. For cells exposed to short SWCNTs-BSA, regions of localized SWCNT concentration correlated spatially with distinct pockets of higher bundle fractions, as well as reduced NIR fluorescence. For macrophages exposed to long SWCNTs, subcellular regions of equal SWCNT concentration did not appear to have increased bundle fraction or severely reduced NIR fluorescence. We quantified the average bundle fraction and NIR fluorescence for all signal pixels across multiple individual cells (Figure 4.6B). The bundle fraction histogram from cells treated with short SWCNTs-BSA was shifted to higher values compared to cells treated with long SWCNTs-BSA, indicating that short SWCNTs are aggregated more within macrophages. The NIR fluorescence histogram from cells treated with short SWCNTs-BSA was

correspondingly shifted to lower values than cells treated with long SWCNTs-BSA, confirming the increased subcellular aggregation into bundles also resulted in quenching of NIR fluorescence. Further, the bundle fraction of short, but not long, SWCNTs-BSA was significantly increased in cells compared to the starting dispersion ($p < 0.0001$), while the NIR fluorescence of both short and long SWCNTs-BSA was significantly decreased ($p < 0.05$). To account for differences in the starting bundle fraction and NIR fluorescence of short and long SWCNTs-BSA dispersions, we normalized the quantified bundle fractions and NIR fluorescence in cells to the starting SWCNTs dispersions (Figure 4.6C). After normalization, the bundle fraction of short SWCNTs-BSA in cells was increased by ~6.1-fold compared to just ~1.9-fold for long SWCNTs-BSA, indicating significantly greater bundling of short SWCNTs as a result of subcellular processing by macrophages. Normalized NIR fluorescence for of short SWCNTs-BSA in cells was reduced by ~2.1-fold, which was just slightly more than the ~1.9-fold reduction for long SWCNTs-BSA.

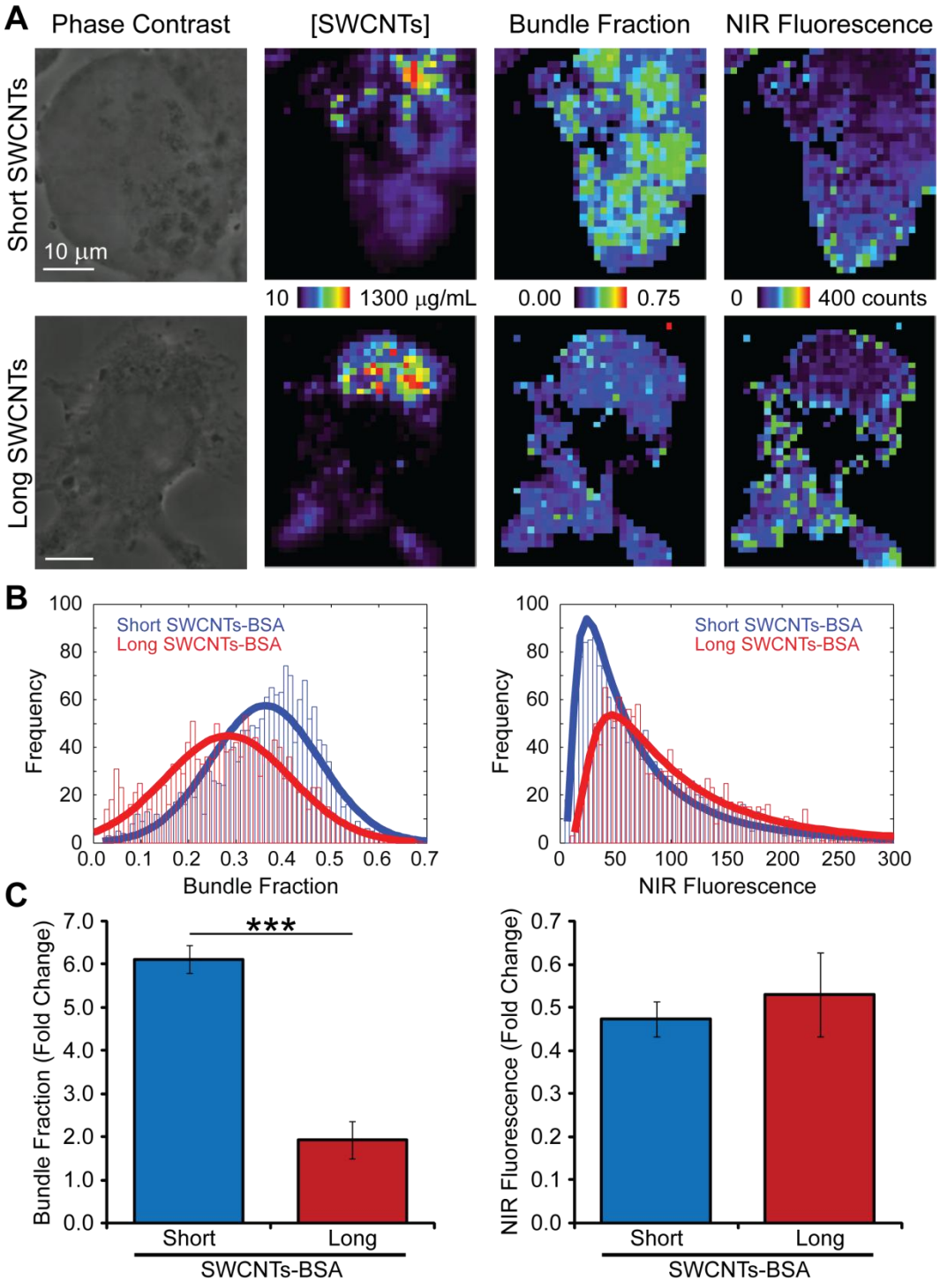

Figure 4.6: Subcellular distribution and aggregation state of short and long SWCNTs-BSA in macrophages. (A) Raman spectroscopy maps taken over individual cells. Each pixel represents a Raman spectrum containing G-band signal for SWCNT concentration, as well as radial breathing modes and NIR fluorescence intensities used to quantify SWCNT aggregation state. SWCNT

concentration maps show regions of similarly high subcellular concentrations of both short and long SWCNTs-BSA. For cells treated with short SWCNTs-BSA, localized regions of SWCNT concentration correspond spatially to regions with higher SWCNT aggregation evidenced by increased bundle fraction and reduced NIR fluorescence. (B) Frequency distributions for all bundle fraction and NIR fluorescence intensity pixel measurements taken across multiple cells for short and long SWCNTs-BSA. Cell exposure to short SWCNTs-BSA results in a shift of the distribution to higher bundle fractions and lower NIR fluorescence compared with cell exposure to long SWCNTs-BSA. The lines represent Gaussian or inverses Gaussian fits to the distributions for bundle fraction or NIR fluorescence, respectively. (C) Quantification of the average fold change in bundle fraction and NIR fluorescence for short and long SWCNTs-BSA in cells relative to their respective starting values as dispersions in solution. The bundle fraction of short SWCNTs-BSA was significantly increased in cells compared to long SWCNTs-BSA, while NIR fluorescence was decreased slightly. Data = mean ± SEM from ≥ 4 fields of view, ***$p < 0.001$ between indicated groups.

For cells exposed to short SWCNTs-BSA we observed that the distribution of subcellular regions with increased bundle fraction also appeared to correlate with changes in cellular morphology in the form of dense regions visible under phase contrast microscopy. We saw similar pocketed phase dense regions in a majority of other cells treated with short SWCNTs-BSA. Using Raman spectroscopy, we selectively examined the average RBM intensity corresponding to individual and bundled SWCNTs within the phase dense regions (Figure 4.7). We found SWCNTs in these regions were highly aggregated, suggesting spatially localized regions of preferential SWCNT bundling with the cell. These regions may represent fused endocytic vesicles which were less abundant in cells treated with long SWCNTs-BSA.

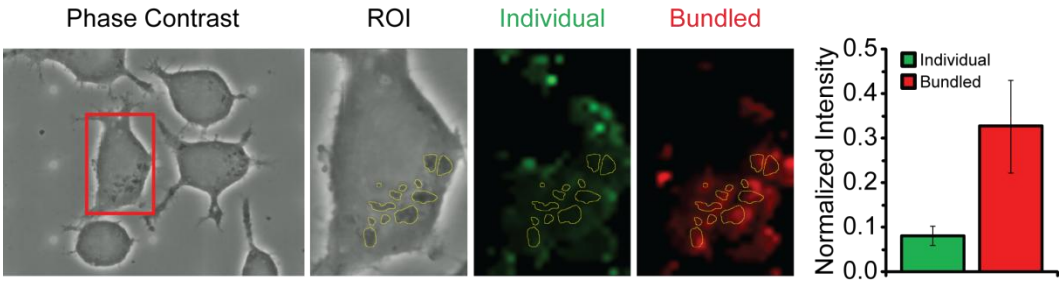

Figure 4.7: Subcellular processing of short SWCNTs-BSA in macrophages. Spatial correlation of phase dense subcellular regions identified in phase contrast images with Raman spectroscopy mapping results shows these regions are preferentially comprised of less individual and more bundled SWCNTs. Data = mean ± SD.

Analyses of RBMs and NIR fluorescence from Raman spectra have been utilized to characterize SWCNT dispersion quality and bundling in solution.[39] Yet there are limited works exploiting these features to analyze the dispersion status of SWCNTs in cellular systems. Raman spectroscopy has been used to visualize live cell uptake dynamics of individual SWCNT chiralities in macrophages. Using DNA dispersed unaltered HiPCO SWCNTs, very little intracellular SWCNT bundling was observed over 30 minutes.[40] Here, we have length fractionated and dispersed SWCNTs with BSA to compare the length dependent subcellular distribution and intracellular state of SWCNTs after 48 hours of exposure. The concomitant increase in bundle fraction, reflecting perturbations to nanotube electronic structure, along with decreases in NIR fluorescence indicating some type of quenching may suggest direct SWCNT-SWCNT contact and removal of the protein dispersing agent. This would not be surprising if SWCNTs are clustered within intracellular compartments of a macrophage cell type containing large amounts of digestive enzymes. Bundled SWCNTs have been observed in the

lysosomes of human macrophages directly under transmission electron microscopy.[41] For long SWCNTs-BSA, the additional surface area available for more extensive protein coverage may help to prevent cell induced aggregation. Further, the high aspect ratio of long SWCNTs-BSA may prevent equivalent levels of cellular processing or facilitate disruption of intracellular vesicles.[42]

4.3.5 Fibroblasts Bundle Short SWCNTs-BSA Less and Release More SWCNTs Over Time than Macrophages

Since we found macrophages increased cellular uptake of short SWCNTs by bundling them within distinct intracellular regions, we examined the subcellular distribution and aggregation state of SWCNTs in fibroblasts to see if other endocytic cell types behaved similarly. Macrophages and fibroblasts were exposed to a higher concentration of 30 μg/mL short SWCNTs-BSA for 24 h. Subcellular Raman spectroscopy maps of fibroblasts showed a more homogeneous distribution of lower SWCNT concentrations (Figure 4.8A). Quantification over several multiple cell fields of view revealed fibroblasts had significantly lower average bundle fraction and significantly increased average NIR fluorescence compared to macrophages. Relative to the initial short SWCNTs-BSA dispersion, the bundle fraction of short SWCNTs-BSA in fibroblasts increased by ~1.9-fold compared to ~6.3-fold for macrophages, while the NIR fluorescence increased by ~1.1-fold compared to the ~2.3-fold decrease observed for macrophages. Since bundling of SWCNTs in cells may result in part from removal of the BSA surface coating, the cellular specific processing

combined with higher protein digestive activity in macrophages could contribute to the observed increased bundling compared to fibroblasts.

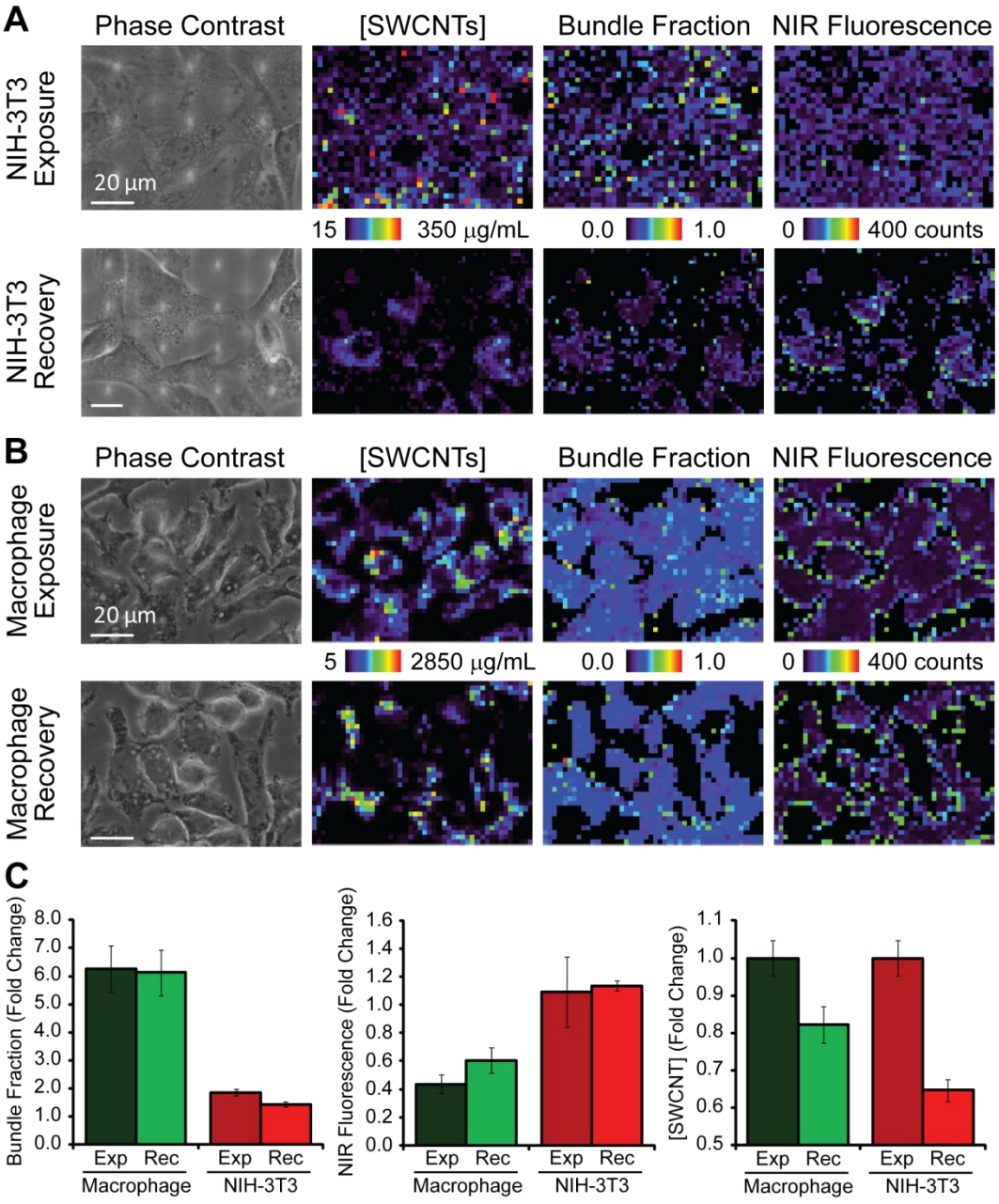

Figure 4.8: Subcellular concentration, distribution, and aggregation state of short SWCNTs-BSA over time in NIH-3T3 fibroblasts and macrophages. (A) Raman spectroscopy maps of multi-cell fields of view for NIH-3T3 fibroblasts

exposed at 30 μg/mL show subcellular distributions of SWCNTs with lower bundle fraction and higher NIR fluorescence after 24 h exposure compared with macrophages. Exposure cells were continued in culture for 24 h without SWCNTs providing an equal time period for cell recovery. For fibroblasts, the recovery results in lower subcellular SWCNT concentrations with reduced bundle fraction and slightly increased NIR fluorescence. (B) Raman spectroscopy maps of macrophages show higher SWCNT concentrations with increased bundle fractions and lower NIR fluorescence. After the recovery period, Raman maps remain largely unchanged with slightly reduced concentration and minimal change in bundle fraction and NIR fluorescence. (C) Quantification of the average fold change in SWCNT concentration, bundle fraction, and NIR fluorescence for short SWCNTs-BSA in recovery cells relative to respective cell exposure without recovery time. The concentration of SWCNTs was reduced more for fibroblasts than macrophages which had lower initial bundle fraction and higher NIR fluorescence. Data = mean ± SEM from ≥ 2 fields of view for exposure, data = mean ± SEM from 1 field of view for recovery.

Since our group and others have observed expulsion of SWCNTs from fibroblasts,[9-10] we characterized the state of SWCNTs remaining in cells and compared fibroblasts with macrophages to determine if they would similarly expel SWCNTs. After 24 h of short SWCNTs-BSA exposure, we removed SWCNT treatment media and replaced with fresh nanotube free media, allowing the cells to experience a 24 h "recovery" period without SWCNTs (Figure 4.8A). After recovery, we found that fibroblasts had ~20% reduced bundle fraction and ~35% increased NIR fluorescence, in addition to ~35% less average subcellular SWCNT concentration (Figure 4.8C). We compared the recovery process in macrophages exposed similarly with 30 μg/mL for 24 h, followed by 24 h recovery (Figure 4.8B). Before recovery, macrophages had largely increased subcellular SWCNT concentrations compared to fibroblasts along with significantly increased bundle fraction and reduced NIR fluorescence. After recovery, we observed just ~2% reduction in bundle fraction and ~38% increase

in NIR fluorescence with ~17% decrease in average subcellular SWCNT concentration (Figure 4.8C). Thus, macrophages recovered only half as efficiently as fibroblasts while retaining nearly the full extent of initial intracellular nanotube bundling, suggesting the aggregation state of SWCNTs in cells may play an important role in determining whether SWCNTs are expelled or retained by the cell. Bundling of SWCNTs into larger intracellular aggregates may slow or inhibit the release of SWCNTs from cells as exocytosis rates have been reported to decrease for longer length SWCNTs.[10]

It is worth noting that cellular recovery in this context encompasses both SWCNT expulsion[9-10] and dilution of internalized SWCNTs between daughter cells due to proliferation[43] over the 24 h period. However, for cells studied here, the doubling time for macrophages is lower than for fibroblasts. Further, studies that measured SWCNT expulsion from fibroblasts involved either single particle tracking on timescales much shorter than division[10] or quantification of expulsion time constants well below proliferation time constants.[9] Release of SWCNTs from macrophages and transfer to other cells has been reported, but only with the stress induced release of microvesicles.[44] Enhanced retention of macrophages in cells over extended periods of time without toxicity[45] may be beneficial for diagnostic or tracking applications given that SWCNTs retained their Raman signature and some NIR fluorescence. Additionally, macrophages may serve as useful SWCNT carriers with intrinsic trafficking across the blood-brain barrier[46] and to hypoxic regions in tumors.[47]

4.4 Conclusions

Determining the subcellular distribution and processing in macrophages is important for translating cellular uptake into controllable intracellular applications. We used two different lengths of SWCNTs dispersed in BSA to probe uptake and differential processing in macrophages compared to non-immune cell fibroblasts. We determined that short SWCNTs-BSA were bundled significantly more in macrophages than both long SWCNTs-BSA and short SWCNTs-BSA in fibroblasts. Further, we found that less bundled SWCNTs in fibroblasts were able to exit cells ~2 times more efficiently than highly bundled SWCNTs in macrophages. Both SWCNT length and cell-specific processing have effects on the aggregation state of SWCNTs in macrophages, which we suggest may affect the cellular retention of SWCNTs and find utility in cell based delivery and tracking applications.

4.5 References

1. Rajendran, L.; Knolker, H.-J.; Simons, K. Subcellular targeting strategies for drug design and delivery. *Nature Reviews Drug Discovery* **2010,** *9*, 29-42.

2. Michalet, X.; Pinaud, F. F.; Bentolila, L. A.; Tsay, J. M.; Doose, S.; Li, J. J.; Sundaresan, G.; Wu, A. M.; Gambhir, S. S.; Weiss, S. Quantum Dots for Live Cells, in Vivo Imaging, and Diagnostics. *Science* **2005,** *307*, 538-544.

3. Dresselhaus, M. S.; Dresselhaus, G.; Eklund, P. C. *Science of Fullerenes and Carbon Nanotubes*. Academic Press: San Diego, 1996.

4. Kruss, S.; Hilmer, A. J.; Zhang, J.; Reuel, N. F.; Mu, B.; Strano, M. S. Carbon nanotubes as optical biomedical sensors. *Advanced Drug Delivery Reviews* **2013,** *65*, 1933-1950.

5. Cherukuri, P.; Bachilo, S. M.; Litovsky, S. H.; Weisman, R. B. Near-Infrared Fluorescence Microscopy of Single-Walled Carbon Nanotubes in Phagocytic Cells. *Journal of the American Chemical Society* **2004,** *126*, 15638-15639.

6. Robinson, J.; Welsher, K.; Tabakman, S.; Sherlock, S.; Wang, H.; Luong, R.; Dai, H. High performance in vivo near-IR (>1 μm) imaging and photothermal cancer therapy with carbon nanotubes. *Nano Research* **2010,** *3*, 779-793.

7. Battigelli, A.; Menard-Moyon, C.; Bianco, A. Carbon nanomaterials as new tools for immunotherapeutic applications. *Journal of Materials Chemistry B* **2014,** *2*, 6144-6156.

8. Fadel, T. R.; Fahmy, T. M. Immunotherapy applications of carbon nanotubes: from design to safe applications. *Trends in Biotechnology* **2014,** *32*, 198-209.

9. Holt, B. D.; Dahl, K. N.; Islam, M. F. Cells Take up and Recover from Protein-Stabilized Single-Wall Carbon Nanotubes with Two Distinct Rates. *ACS Nano* **2012,** *6*, 3481-3490.

10. Jin, H.; Heller, D. A.; Sharma, R.; Strano, M. S. Size-Dependent Cellular Uptake and Expulsion of Single-Walled Carbon Nanotubes: Single Particle Tracking and a Generic Uptake Model for Nanoparticles. *ACS Nano* **2009,** *3*, 149-158.

11. Heller, D. A.; Baik, S.; Eurell, T. E.; Strano, M. S. Single-Walled Carbon Nanotube Spectroscopy in Live Cells: Towards Long-Term Labels and Optical Sensors. *Advanced Materials* **2005,** *17*, 2793-2799.

12. Boyer, P. D.; Holt, B. D.; Islam, M. F.; Dahl, K. N. Decoding membrane- versus receptor-mediated delivery of single-walled carbon nanotubes into macrophages using modifications of nanotube surface coatings and cell activity. *Soft Matter* **2013,** *9*, 758-764.

13. Sahay, G.; Alakhova, D. Y.; Kabanov, A. V. Endocytosis of nanomedicines. *Journal of Controlled Release* **2010,** *145*, 182-195.

14. Khalil, I. A.; Kogure, K.; Akita, H.; Harashima, H. Uptake Pathways and Subsequent Intracellular Trafficking in Nonviral Gene Delivery. *Pharmacological Reviews* **2006,** *58*, 32-45.

15. Rejman, J.; Oberle, V.; Zuhorn, I. S.; Hoekstra, D. Size-dependent internalization of particles via the pathways of clathrin-and caveolae-mediated endocytosis. *Biochemical Journal* **2004,** *377*, 159-169.

16. Holt, B. D.; Dahl, K. N.; Islam, M. F. Quantification of Uptake and Localization of Bovine Serum Albumin-Stabilized Single-Wall Carbon Nanotubes in Different Human Cell Types. *Small* **2011,** *7*, 2348-2355.

17. Holt, B. D.; McCorry, M. C.; Boyer, P. D.; Dahl, K. N.; Islam, M. F. Not all protein-mediated single-wall carbon nanotube dispersions are equally bioactive. *Nanoscale* **2012,** *4*, 7425-7434.

18. Tsyboulski, D. A.; Hou, Y.; Fakhri, N.; Ghosh, S.; Zhang, R.; Bachilo, S. M.; Pasquali, M.; Chen, L.; Liu, J.; Weisman, R. B. Do Inner Shells of Double-Walled Carbon Nanotubes Fluoresce? *Nano Letters* **2009,** *9*, 3282-3289.

19. Islam, M. F.; Milkie, D. E.; Torrens, O. N.; Yodh, A. G.; Kikkawa, J. M. Magnetic heterogeneity and alignment of single wall carbon nanotubes. *Physical Review B* **2005,** *71*, 201401.

20. Johnston, D. E.; Islam, M. F.; Yodh, A. G.; Johnson, A. T. Electronic devices based on purified carbon nanotubes grown by high-pressure decomposition of carbon monoxide. *Nature Materials* **2005,** *4*, 589-592.

21. Islam, M. F.; Rojas, E.; Bergey, D. M.; Johnson, A. T.; Yodh, A. G. High Weight Fraction Surfactant Solubilization of Single-Wall Carbon Nanotubes in Water. *Nano Letters* **2003,** *3*, 269-273.

22. Arnold, M. S.; Green, A. A.; Hulvat, J. F.; Stupp, S. I.; Hersam, M. C. Sorting carbon nanotubes by electronic structure using density differentiation. *Nature Nanotechnology* **2006,** *1*, 60-65.

23. Becker, M. L.; Fagan, J. A.; Gallant, N. D.; Bauer, B. J.; Bajpai, V.; Hobbie, E. K.; Lacerda, S. H.; Migler, K. B.; Jakupciak, J. P. Length-Dependent Uptake of DNA-Wrapped Single-Walled Carbon Nanotubes. *Advanced Materials* **2007,** *19*, 939-945.

24. Fagan, J. A.; Becker, M. L.; Chun, J.; Hobbie, E. K. Length Fractionation of Carbon Nanotubes Using Centrifugation. *Advanced Materials* **2008,** *20*, 1609-1613.

25. Huang, Y. Y.; Knowles, T. P. J.; Terentjev, E. M. Strength of Nanotubes, Filaments, and Nanowires From Sonication-Induced Scission. *Advanced Materials* **2009,** *21*, 3945-3948.

26. Yaron, P.; Holt, B.; Short, P.; Lösche, M.; Islam, M.; Dahl, K. Single wall carbon nanotubes enter cells by endocytosis and not membrane penetration. *Journal of Nanobiotechnology* **2011,** *9*, 45.

27. Holt, B. D.; Short, P. A.; Rape, A. D.; Wang, Y.-l.; Islam, M. F.; Dahl, K. N. Carbon Nanotubes Reorganize Actin Structures in Cells and ex Vivo. *ACS Nano* **2010,** *4*, 4872-4878.

28. Holt, B. D.; Shams, H.; Horst, T. A.; Basu, S.; Rape, A. D.; Wang, Y.-L.; Rohde, G. K.; Mofrad, M. R. K.; Islam, M. F.; Dahl, K. N. Altered Cell Mechanics from the Inside: Dispersed Single Wall Carbon Nanotubes Integrate with and Restructure Actin. *Journal of Functional Biomaterials* **2012,** *3*, 398-417.

29. Paredes, J. I.; Burghard, M. Dispersions of Individual Single-Walled Carbon Nanotubes of High Length. *Langmuir* **2004,** *20*, 5149-5152.

30. O'Connell, M. J.; Bachilo, S. M.; Huffman, C. B.; Moore, V. C.; Strano, M. S.; Haroz, E. H.; Rialon, K. L.; Boul, P. J.; Noon, W. H.; Kittrell, C.; Ma, J.; Hauge, R. H.; Weisman, R. B.; Smalley, R. E. Band Gap Fluorescence from Individual Single-Walled Carbon Nanotubes. *Science* **2002,** *297*, 593-596.

31. Dresselhaus, M. S.; Dresselhaus, G.; Saito, R.; Jorio, A. Raman spectroscopy of carbon nanotubes. *Physics Reports* **2005,** *409*, 47-99.

32. Heller, D. A.; Barone, P. W.; Swanson, J. P.; Mayrhofer, R. M.; Strano, M. S. Using Raman Spectroscopy to Elucidate the Aggregation State of Single-Walled Carbon Nanotubes. *Journal of Physical Chemistry B* **2004,** *108*, 6905-6909.

33. O'Connell, M. J.; Sivaram, S.; Doorn, S. K. Near-infrared resonance Raman excitation profile studies of single-walled carbon nanotube intertube interactions: A direct comparison of bundled and individually dispersed HiPco nanotubes. *Physical Review B* **2004,** *69*, 235415.

34. Rajan, A.; Strano, M. S.; Heller, D. A.; Hertel, T.; Schulten, K. Length-Dependent Optical Effects in Single Walled Carbon Nanotubes†. *The Journal of Physical Chemistry B* **2008,** *112*, 6211-6213.

35. Hertel, T.; Himmelein, S.; Ackermann, T.; Stich, D.; Crochet, J. Diffusion Limited Photoluminescence Quantum Yields in 1-D Semiconductors: Single-Wall Carbon Nanotubes. *ACS Nano* **2010,** *4*, 7161-7168.

36. Harrah, D. M.; Swan, A. K. The Role of Length and Defects on Optical Quantum Efficiency and Exciton Decay Dynamics in Single-Walled Carbon Nanotubes. *ACS Nano* **2011,** *5*, 647-655.

37. Bachilo, S. M.; Strano, M. S.; Kittrell, C.; Hauge, R. H.; Smalley, R. E.; Weisman, R. B. Structure-Assigned Optical Spectra of Single-Walled Carbon Nanotubes. *Science* **2002,** *298*, 2361-2366.

38. Chithrani, B. D.; Ghazani, A. A.; Chan, W. C. W. Determining the Size and Shape Dependence of Gold Nanoparticle Uptake into Mammalian Cells. *Nano Letters* **2006,** *6*, 662-668.

39. Karajanagi, S. S.; Yang, H.; Asuri, P.; Sellitto, E.; Dordick, J. S.; Kane, R. S. Protein-Assisted Solubilization of Single-Walled Carbon Nanotubes. *Langmuir* **2006,** *22*, 1392-1395.

40. Kang, J. W.; Nguyen, F. T.; Lue, N.; Dasari, R. R.; Heller, D. A. Measuring Uptake Dynamics of Multiple Identifiable Carbon Nanotube Species via High-Speed Confocal Raman Imaging of Live Cells. *Nano Letters* **2012,** *12*, 6170-6174.

41. Porter, A. E.; Gass, M.; Bendall, J. S.; Muller, K.; Goode, A.; Skepper, J. N.; Midgley, P. A.; Welland, M. Uptake of Noncytotoxic Acid-Treated Single-Walled Carbon Nanotubes into the Cytoplasm of Human Macrophage Cells. *ACS Nano* **2009,** *3*, 1485-1492.

42. Ji, Z.; Wang, X.; Zhang, H.; Lin, S.; Meng, H.; Sun, B.; George, S.; Xia, T.; Nel, A. E.; Zink, J. I. Designed Synthesis of CeO2 Nanorods and Nanowires for Studying Toxicological Effects of High Aspect Ratio Nanomaterials. *ACS Nano* **2012,** *6*, 5366-5380.

43. Kim, J. A.; Aberg, C.; Salvati, A.; Dawson, K. A. Role of cell cycle on the cellular uptake and dilution of nanoparticles in a cell population. *Nature Nanotechnology* **2012,** *7*, 62-68.

44. Marangon, I.; Boggetto, N.; Ménard-Moyon, C.; Venturelli, E.; Béoutis, M.-L.; Péchoux, C.; Luciani, N.; Wilhelm, C.; Bianco, A.; Gazeau, F. Intercellular Carbon Nanotube Translocation Assessed by Flow Cytometry Imaging. *Nano Letters* **2012,** *12*, 4830-4837.

45. Bertulli, C.; Beeson, H. J.; Hasan, T.; Huang, Y. Y. S. Spectroscopic characterization of protein-wrapped single-wall carbon nanotubes and

quantification of their cellular uptake in multiple cell generations. *Nanotechnology* **2013,** *24*, 265102

46. Madsen, S.; Baek, S.-K.; Makkouk, A.; Krasieva, T.; Hirschberg, H. Macrophages as Cell-Based Delivery Systems for Nanoshells in Photothermal Therapy. *Annals of Biomedical Engineering* **2012,** *40*, 507-515.

47. Choi, M.-R.; Stanton-Maxey, K. J.; Stanley, J. K.; Levin, C. S.; Bardhan, R.; Akin, D.; Badve, S.; Sturgis, J.; Robinson, J. P.; Bashir, R.; Halas, N. J.; Clare, S. E. A Cellular Trojan Horse for Delivery of Therapeutic Nanoparticles into Tumors. *Nano Letters* **2007,** *7*, 3759-3765.

5 Delivering Single Wall Carbon Nanotubes to the Nucleus Using Engineered Nuclear Protein Moieties

5.1 Introduction

Controlled delivery of nanoparticles to subcellular structures including actin filaments,[1-2] mitochondria,[3-4] and the nucleus[5-7] has potential for numerous biomedical applications including modulation of these structures,[8] *in situ* sensors,[9] ablation,[10] and drug delivery.[11] Specifically, transport to the nucleus is required for delivery of DNA for gene therapy, and many anti-cancer strategies include nuclear targeting of small molecular drugs to inhibit DNA duplication or induction of DNA damage by radiation or ablation. Single wall carbon nanotubes (SWCNTs) possess unique mechanical, thermal, electrical, and optical properties making them attractive materials for subcellular imaging, sensing, ablation, and modulation.[12] Most importantly for delivery to the nucleus, small SWCNTs can be internalized by cells at large numbers, and they have a large surface area enabling functionalization for targeting and molecular loading.

Hydrophobic SWCNTs aggregate in water due to strong van der Waals forces, and the resulting bundles have diminished optical properties[13] and deleterious cellular effects.[14] Covalent modifications of SWCNTs promote dispersion into solution as well as adding moieties for targeting to the nucleus.[5, 15-17] However, such chemical functionalizations of SWCNTs alter the sp^2 structure and diminish inherent properties desired for biomedical applications.[18] Non-

covalent attachments of SWCNTs are preferred to retain SWCNT properties, and surfactant-like copolymers, lipids, DNA, proteins and other biomolecules can stably disperse SWCNTs into solution.[19-20] Surfactant-like proteins, such as albumins, are excellent dispersing agents for SWCNTs[21-31] and promote SWCNT cellular entry at extremely high levels (up to millions per cell).[26, 30] However, the interfacial thermodynamic requirements for proteins to individually disperse SWCNTs at suitable concentrations for cellular therapy limits the choice of proteins.[29]

For nuclear targeting we consider SWCNT dispersion with an engineered version of a nuclear protein. The tail domain of the lamin B1 nuclear protein (LB1) lacks an ordered three-dimensional structure, aside from an immunoglobulin (Ig)-fold with a hydrophobic pocket.[32-33] The hydrophobic core between β-sheets of the Ig-fold provides a globular character to LB1 proteins which, along with the ~22 kDa size, present essential structural characteristics likely suitable to disperse SWCNTs. Importantly, LB1 also contains a well-presented nuclear localization sequence (NLS) at the C-terminus, which allows active import of proteins and other larger materials (> 40 kDa) into the nucleus through the nuclear pore complex (NPC).[34]

Here, we report that SWCNTs can be stably dispersed by LB1, hereafter referred to as SWCNTs-LB1, at reasonably high concentrations of at least 150 μg/mL with long-term stability of at least 75 days. We also compare cellular and nuclear delivery of SWCNT-LB1 to SWCNTs dispersed by the nonspecific protein bovine serum albumin (BSA). Nearly one million SWCNTs-LB1 entered

HeLa cells and translocated to the nucleus unlike SWCNTs-BSA, which entered cells at similarly high numbers but remained largely in the cytoplasm. We confirmed nuclear localization by near-infrared (NIR) fluorescence imaging of the SWCNTs and examined molecular interactions between SWCNTs and DNA within the nucleus using fluorescence lifetime imaging microscopy (FLIM). This functional delivery of non-covalently dispersed SWCNTs holds numerous possibilities in gene and cancer therapies as well as the potential for other engineered protein fragments for specific subcellular delivery.

5.2 Materials and Methods

5.2.1 Protein Production and Characterization

LB1 cDNAs (from amino acid R386 to the C-terminus at amino acid M586) were produced from full length cDNA (Accession number AAC37575) by PCR and subcloned into the (Glutathione S Transferase) GST-parallel vector, as described in previous work.[35-38] The plasmids were expressed in E. coli BL21 Codon-Plus cells (Agilent) at 37 °C. Purification was performed with glutathione magnetic beads (Pierce) and the protein was cleaved enzymatically with proTEV cleavage enzyme (Promega) at 30 °C for 5 – 7 h. The cleaved protein was further purified by exposure to agarose glutathione beads (Pierce) to remove excess GST. Purified protein was dialyzed (Slide-A-Lyzer Dialysis Cassettes; Pierce) into deionized water. Concentration was measured by Bradford assay, and protein concentration was adjusted to 5 mg/mL. In our previous study, we fully characterized protein purity using mass spectroscopy and gel electrophoresis as

well as structure using fluorescence spectroscopy, calorimetry, and circular dichroism.[35-38]

5.2.2 SWCNT Dispersions

Unpurified HiPCO (high-pressure carbon monoxide conversion synthesis) SWCNTs (Carbon Nanotechnologies, Inc.) with diameters of 1.0 ± 0.3 nm and polydisperse lengths were purified according to previously established methods.[39-40] The purified SWCNT sample contained < 5 wt% carbonaceous impurities, ~0.3 wt% metallic impurities, and the rest unaltered SWCNTs.[39-40] Length fractionation was performed to obtain SWCNTs with lengths of 145 ± 17 nm, as described previously.[41-44]

The SWCNT dispersion scheme using LB1 was similar to the methods we have used to disperse SWCNTs with BSA and other proteins.[26, 29] Briefly, LB1 or BSA (Sigma-Aldrich) proteins were dissolved in ultrapure deionized water (resistivity 18.3 MΩ/cm, total oxidizable carbon < 5 ppb) and added to SWCNTs to achieve 5:1 protein:SWCNT by weight. The starting SWCNT concentration was set at 0.025 wt%, *i.e.,* 250 μg/mL. The mixtures of protein and SWCNTs were dispersed in water using a probe-tip sonicator (Fisher Scientific, Model 100; 3 mm tip diameter) at an average 5 W for 2 h. Under these conditions, the ~150 nm length SWCNTs were not shortened from sonication induced scission.[45] To separate bundles from isolated SWCNTs, suspensions were centrifuged at 21,000×*g* for 7 min. The supernatants were collected and, for cell experiments, were subsequently sterilized by ultraviolet light for 1 h.

5.2.3 SWCNT Dispersion Characterization

UV-vis-NIR absorbance spectroscopy: To quantitatively determine SWCNT concentration and qualitatively assess dispersion quality, SWCNT dispersions were examined using a UV-vis-NIR absorbance spectrometer (Varian Cary 5000). Concentration was determined using an extinction coefficient of 2.6 (absorbance·mL)/(mg·mm) at 930 nm.[44] The sharpness and amplitude of the van Hove peaks qualitatively indicate dispersion quality.[13] The stability of the SWCNTs-LB1 dispersion in ultrapure water was monitored over 75 days using UV-vis-NIR absorbance spectroscopy by quantifying the peak width at half max of the van Hove peaks in the NIR region. The stability in complete cell culture media was similarly monitored over 72 h at 30 μg/mL, which was the highest experimental concentration and longest exposure time.

Raman spectroscopy: Structural integrity of SWCNTs after dispersion using LB1 and stability in complete cell culture media were characterized with a Raman spectrometer (Renishaw inVia) coupled to an inverted confocal Raman microscope using a 50× air objective with 0.75 numerical aperture (NA) and a 785 nm laser (100 mW). Spectra were acquired between 100 – 3200 cm^{-1}. Each Raman spectrum was normalized by its G-band intensity.

NIR fluorescence spectroscopy: SWCNTs-LB1 dispersion quality was further characterized with a NIR fluorescence spectrometer (Horiba Jobin Yvon Nanolog). SWCNTs-LB1 samples were diluted to 0.3 absorbance/cm in water and NIR fluorescence spectra were collected with a 120 s integration time with excitation and emission slit widths of 14 nm using a liquid nitrogen cooled

detector (Symphony InGaAs-1700). NIR fluorescence intensity maps were constructed using FluorEscence and Nanosizer software.

5.2.4 Cell Culture and Treatment

HeLa cells were cultured in Dulbecco's modified Eagle's medium (1000 mg/L glucose, 4.0 mM L-glutamine, and 110 mg/L sodium pyruvate; Thermo Scientific Hyclone), supplemented with 10% v/v fetal bovine serum (FBS; Invitrogen) and 1% v/v penicillin-streptomycin (Invitrogen). Cells were maintained at 37 °C and 5% CO_2. HeLa cells were seeded at 3×10^4 cells/cm^2 onto sterilized #1.5 coverslips. For 24 h exposure condition, cells were maintained in culture for 72 h. For 48 and 72 h exposure conditions, cells were maintained in culture for 24 h. Then, SWCNTs were diluted to the exposure concentration (10 μg/mL for Raman spectroscopy and imaging experiments or 30 μg/mL for NIR fluorescence imaging experiments) in fresh cell culture media and added to the cells for the indicated treatment time. Afterwards, the media containing SWCNTs was removed. Cells were gently washed three times in PBS and subsequently fixed with 3.7% v/v formaldehyde (Sigma-Aldrich) for 15 min and mounted onto glass slides. For 72 h treatment, fixed cells were labeled with DAPI (Life Technologies), and mounted onto glass slides.

5.2.5 Cell Imaging and Quantification

Confocal Raman Spectroscopy Imaging: Phase contrast imaging and confocal Raman spectroscopy imaging were performed on an inverted, confocal

Raman microscope (Renishaw inVia) using a 0.9 NA air condenser, a 100× (1.4 NA) oil immersion objective, and a 785 nm laser (100 mW). Control of mapping parameters and imaging processing were performed using WiRE software. For Raman mapping, confocal Raman spectra were acquired with an X-Y step size ≤ 2.3 μm. Spectra between 1336 – 1829 cm^{-1} were collected with 0.86 cm^{-1} resolution for integration times of 1 s. Spatial maps of the G-band intensity (1590 ± 20 cm^{-1}) above the baseline signal were performed in WiRE software (Renishaw). Local SWCNT concentration was determined using a calibration curve relating G-band intensity to SWCNT concentration determined *via* UV-vis-NIR absorbance spectroscopy. For the indicated cells, automatic confocal depth slicing was performed across the cell nucleus, whereby 6 – 10 independent points in the X-Y plane were monitored. Confocal Raman spectra were acquired at each point in the Z-direction, where 0 μm corresponds to the focal plane of the cell nucleus.

Quantification of SWCNTs per cell: Cell area was determined from phase contrast images using ImageJ, and average cell height was assumed to be 10 μm. Average SWCNT concentration was determined from the Raman G-band intensity of ~200 individual confocal concentration points and extrapolated to the entire cell volumes.

NIR Fluorescence Imaging: Phase contrast imaging and widefield NIR fluorescence imaging were performed on an inverted, Leica DMI 4000 light and fluorescence microscope using a 0.9 NA air condenser and a 100× (1.4 NA) oil immersion objective. A 785 nm laser (120 mW, CrystaLaser) that was circularly

polarized (quarter-wave plate), decohered (diffuser, ThorLabs), and expanded (bi-convex lens) to fill the objective back focal plane and a 320 pixel × 256 pixel liquid nitrogen cooled InGaAs focal plane array detector (2D-OMA V, Princeton Instruments) were interfaced with the microscope *via* a custom setup to obtain widefield NIR fluorescence images. Within the microscope, a NIR filter cube with a 785 nm excitation notch filter, a 785 nm dichroic, and a 792 nm long pass filter (Semrock) was used in concert with an additional 900 nm long pass filter to limit transmission of excitation light and autofluorescence to the detector ensuring high sensitivity for SWCNT NIR fluorescence. Control of imaging parameters and processing were performed using WinView software (Princeton Instruments). For NIR imaging, NIR fluorescence intensity between 900 – 1700 nm was collected after dark current background correction for integration times ≥ 15 s. Spatial maps of SWCNT NIR fluorescence intensity above noise (~50 counts/s) were performed in WinView software. Images of SWCNT NIR fluorescence across all conditions were scaled to the same dynamic range.

5.2.6 Fluorescence Lifetime Imaging and Analysis

Fluorescence Lifetime Imaging Microscopy: FLIM was performed as previously reported by our group[2, 46] on a Leica TCS SP5 inverted laser scanning confocal microscope using a 100× (1.4 NA) oil immersion objective. A tunable mode-locked Ti:sapphire 80 MHz pulsed laser (Chameleon, Coherent) was tuned to 785 nm for multiphoton excitation of DAPI, and wavelengths of 398 – 602 nm were passed to a photomultiplier tube to detect the full emission range of DAPI.

Time-correlated single photon counting (TCSPC) was performed using a Becker & Hickl SPC-830 counting board and controlled with SPCM software (Becker & Hickl). 256 pixel × 256 pixel lifetime images were acquired at a scan rate of 400 Hz for 300 s with 220 time channels and a measurement window of 10.8 ns to enable an accurate determination of exponential decays and to minimize the coefficient of variation.[47-48]

Fluorescence Lifetime Imaging Microscopy Image Processing: SPCImage software (Becker & Hickl) was used to calculate the lifetime fits per pixel and render spatial lifetime images. Fluorescence lifetime can be modeled as a sum of exponentials:

$$I(t) = I_o + \sum_n a_n e^{-t/\tau_n}$$

where *I(t)* is the intensity of emitted photons as a function of time, I_o is an offset, a_n is the relative amplitude of the n^{th} lifetime, and τ_n is the n^{th} lifetime.[49-50] Data were modeled as a single exponential decay (n = 1) and as a double exponential decay (n = 2). As necessary, double exponential decay lifetime data was binned to achieve a peak photon count of > 1000 to ensure accurate fits.[48, 50] For double exponential decay lifetime data, the mean fluorescence (τ_m) lifetime[50] was used to represent the data:

$$\tau_m = \sum_n a_n \tau_n \Big/ \sum_n a_n$$

Pixel-by-pixel single and double exponential lifetime decay data and their corresponding goodness of fits (χ^2) were exported to MATLAB (The MathWorks,

Inc.) for further analysis. Fluorescence lifetime was best modeled by a double exponential decay, indicated by χ^2 closer to unity without over fitting.[46, 50]

FLIM images were photon peak intensity thresholded in SPCImage (Becker & Hickl) to exclude background pixels from analysis. The corresponding fluorescence intensity images were segmented in ImageJ to exclude any extranuclear pixels that represented autofluorescence and not DAPI signal. The nuclear segmentation was used to produce the final lifetime images and perform the τ_m quantification. Lifetime data were analyzed in MATLAB using a previously developed algorithm[46] to determine average, standard deviation, and distribution of DAPI fluorescence lifetime on a per nucleus basis. The final results represent an average of 17 – 33 nuclei per condition. Note that each included (*i.e.*, non-thresholded) pixel represents a unique data point of τ_m.

5.2.7 Nuclear Localization Quantification

Phase contrast imaging and DAPI fluorescence imaging were used to define cell and nuclear borders. Area within the nuclear border comprised the nuclear region (N) and area within the cell border exclusive of the nuclear region comprised the cytoplasm region (C). The perinuclear region (P) was defined as the region formed from a 10× single pixel dilation of the nuclear border, exclusive of the nucleus region, resulting in an annular region ~2.2 μm thick. For each cell, ImageJ software was used to quantify the intensity of SWCNT NIR fluorescence obtained from NIR fluorescence imaging within each of the regions. For

quantitative comparisons, average intensity in the nuclear and perinuclear regions were normalized to average intensity in the cytoplasm regions for each cell. We individually analyzed 60 – 100 cells for each SWCNTs-BSA treatment and 25 – 70 cells for each SWCNTs-LB1 treatment.

5.3 Results and Discussion

5.3.1 SWCNTs are Individually Dispersed by Lamin B1 Tail Domain Proteins

We dispersed SWCNTs with the recombinantly produced globular tail domain of the nuclear lamin B1 protein (Figure 5.1).[35, 38] The resulting SWCNTs-LB1 dispersion was characterized using UV-vis-NIR absorbance, Raman, and NIR fluorescence spectroscopy (Figure 5.2). For quantitative purposes, we compared dispersion characteristics of SWCNTs-LB1 to that of SWCNTs-BSA (Figure 2); SWCNTs-BSA has been shown to be high-quality, stable, and biocompatible.[21-30]

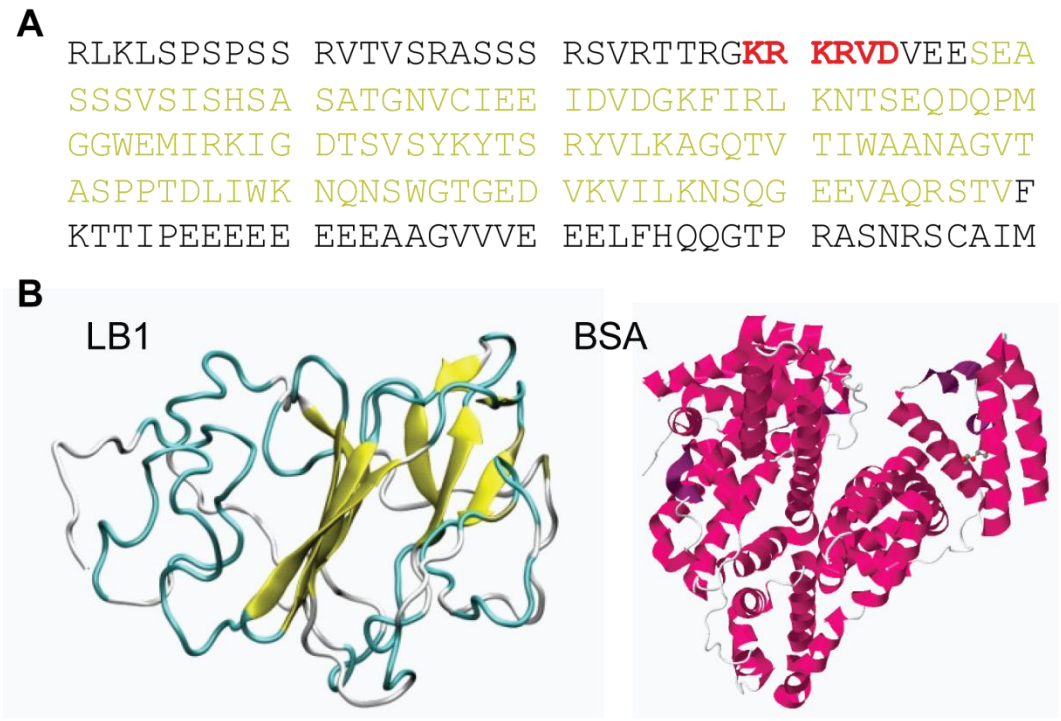

Figure 5.1: Structures of LB1 and BSA used for dispersions. (A) The sequence of the lamin B1 tail (accession number AAC37575) from amino acid R386 to the C-terminus at amino acid M586 with the Ig-fold in yellow and NLS highlighted in red. (B) LB1 contains an Ig-fold (yellow, PDB 3JT0) which is surrounded by primarily disordered protein shown in a likely conformation as determined from replica exchange molecular dynamics simulations (adapted with permission from[32]). BSA, displayed by Cn3D (PDB 4F5S), is mostly α-helix. Both proteins have a central, stable hydrophobic cleft.

Both SWCNTs-BSA and SWCNTs-LB1 were produced using similar protein-to-SWCNT weight ratios and absolute protein concentrations. However, the overall yield of SWCNTs-BSA was 48% higher than SWCNTs-LB1 as determined by UV-vis-NIR absorbance at 930 nm using a known absorption coefficient (Figure 5.2A),[44] suggesting slightly better effectiveness for BSA compared to LB1 in dispersing SWCNTs. Nevertheless, SWCNTs-LB1 showed sharp van Hove peaks in absorbance, indicative of individualized nanotubes in the dispersion. The width of the absorbance peaks in the NIR region corresponding to

the E_{11} transitions at ~1275 nm and ~1140 nm showed an average 3 nm peak broadening for SWCNTs-LB1 compared to SWCNTs-BSA, suggesting SWCNTs-LB1 were slightly less individualized relative to SWCNTs-BSA. We also characterized the SWCNTs-LB1 dispersion using the characteristic Raman signatures of SWCNTs: G-band at ~1590 cm^{-1} that is associated with sp^2-hybridized carbon, D-band at ~1300 cm^{-1} that characterized sp^3-hybridized carbon, and radial breathing modes (RBMs) at 200-275 cm^{-1} (Figure 5.2B).[12] The intensity ratio between D-band and G-band for both SWCNTs-LB1 and SWCNTs-BSA were similar to that of the starting SWCNT powder indicating that the dispersion process did not degrade the structure of SWCNTs. Both SWCNTs-LB1 and SWCNTs-BSA had < 8% of their maximum RBM intensity > 250 cm^{-1}, which corresponds to bundled SWCNTs for the 1.58 eV (785 nm) laser line used,[22, 51] suggesting the majority of SWCNTs were not bundled. Furthermore, we observed NIR fluorescence at ~2300 cm^{-1} in the Raman spectra confirming the presence of individually dispersed SWCNTs in both samples (Figure 5.2B).

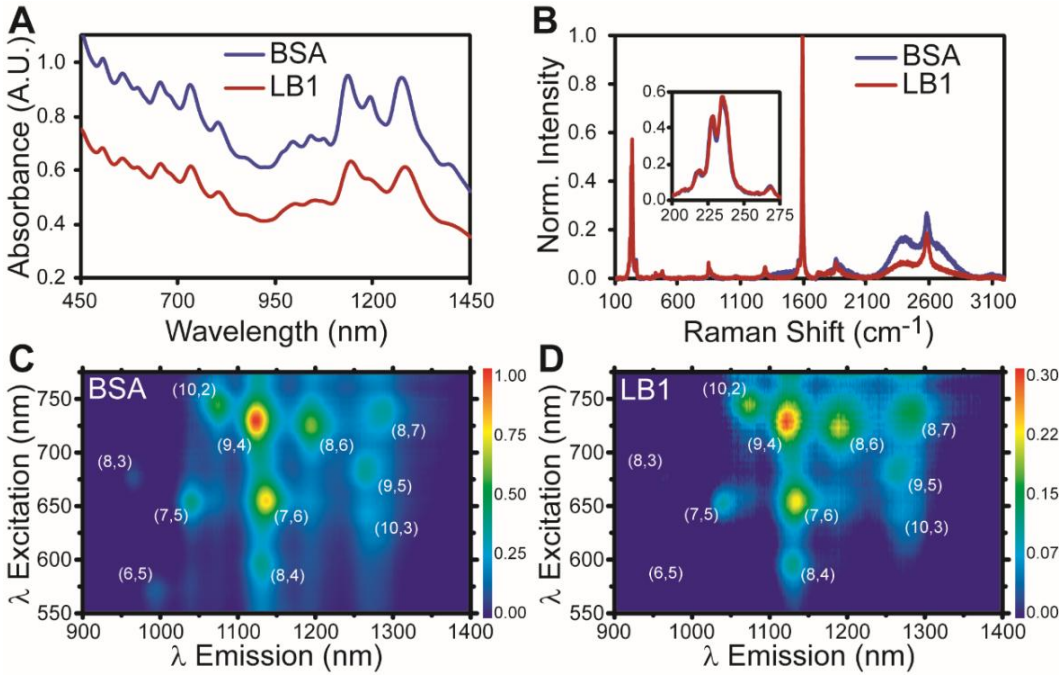

Figure 5.2: Optical characterization of SWCNT dispersions. (A) UV-vis-NIR absorbance spectroscopy of SWCNTs-BSA and SWCNTs-LB1 shows sharp van Hove peaks indicative of individually dispersed SWCNTs. (B) Raman spectroscopy of SWCNTs-BSA and SWCNTs-LB1 confirms dispersions maintain SWCNT structure and result in minimal bundling with NIR fluorescence. The inset magnifies the radial breath mode regime. NIR fluorescence intensity maps for SWCNTs-BSA (C) and SWCNTs-LB1 (D) show a similar distribution of chiralities of individually dispersed SWCNTs. The dynamic range in both maps is scaled to the maximum NIR fluorescence intensity from SWCNTs-BSA.

To further characterize dispersion quality, we performed NIR fluorescence spectroscopy on samples diluted to 0.3 absorbance/cm in water. Individually dispersed SWCNTs emit fluorescence at distinct wavelengths in the NIR region corresponding to different SWCNT chiralities,[52] whereas fluorescence from nanotubes becomes quenched when nanotubes are in bundles.[13] The two-dimensional (2D) fluorescence intensity map for SWCNTs-LB1 showed significant fluorescence intensity at numerous different chiralities demonstrating that LB1 proteins individually disperse SWCNTs in water. By comparing 2D

maps of SWCNTs-LB1 and SWCNTs-BSA, we find that both protein dispersions resulted in a similar distribution of chiralities (Figure 5.2C-D). The quantum yield (QY) for SWCNTs-LB1 was determined to be ~0.004%, which was 2.5 times less than SWCNTs-BSA QY of ~0.010%. The reduced quantum efficiency of SWCNTs-LB1 indicates additional non-radiative energy losses likely due to the presence of more SWCNT bundles. In sum, the data demonstrate LB1 proteins dispersed SWCNTs in water individually with a dispersion quality and efficiency that are somewhat lower than that of BSA but still of exceptional quality required for cellular therapies.

5.3.2 SWCNTs-LB1 Dispersions are Extremely Stable

Many molecules can transiently disperse nanomaterials in water, but flocculation may still occur over time, particularly in the higher ionic strength of biological media.[29] We maintained SWCNTs-LB1 at 160 μg/mL in water for 75 days (Figure 5.3A) and at 30 μg/mL in cell culture media with 10% v/v serum for 3 days (Figure 5.3B) and characterized the dispersion using UV-vis-NIR absorbance spectroscopy. The width of the absorbance peaks in the NIR did not change over 75 days in water or over 3 days diluted in media, suggesting that SWCNTs-LB1 remained stable in the supernatant. For SWCNTs-LB1 in media, the difference in absorbance at ~550 nm was due to the presence of the pH indicator phenol red in the media. We also verified that SWCNTs-LB1 retained their Raman signature with a similar low fraction of RBM bundle intensity and maintained NIR fluorescence at ~2300 cm^{-1} in media (Figure 5.3C). This stability

further suggested that proteins were stably covering the surface of the SWCNTs preventing SWCNT-SWCNT contact that would lead to bundling and settling in water. In media, the SWCNT coating by LB1 was likely sufficiently strong to prevent displacement by serum proteins in the media.

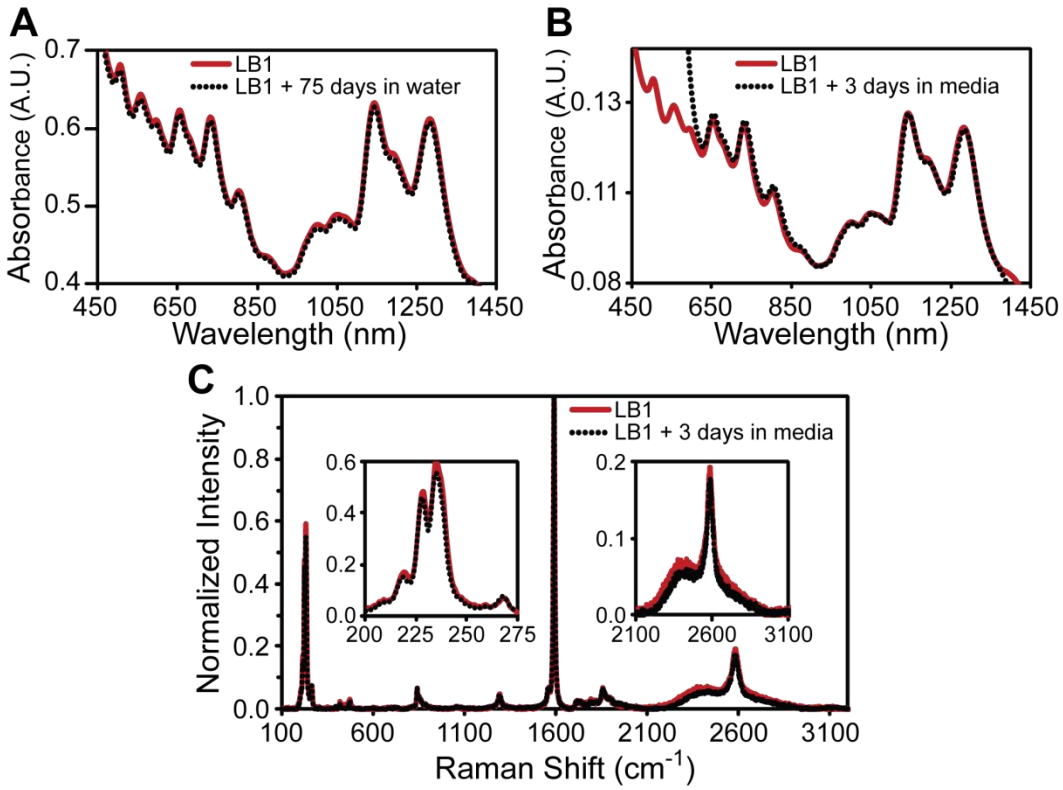

Figure 5.3: SWCNTs-LB1 stability in water and cell culture media characterized with absorbance and Raman spectroscopy. SWCNTs-LB1 absorbance spectra are indistinguishable with no concentration loss or peak broadening in water at the dispersion yield concentration for 75 days (A) or complete cell culture media at the maximum cell exposure concentration for 3 days (B). (C) Raman spectroscopy of SWCNTs-LB1 shows similar RBM and NIR fluorescence features (magnified in insets) in water and after 3 days in cell culture media indicating no significant bundling or loss of NIR fluorescence.

SWCNTs can be dispersed with many proteins, but some proteins such as lysozyme, immunoglobulins, *etc.* do not produce stable dispersions in high ionic

strength biological media.[29] From our works with protein-dispersed SWCNTs, here and in previous studies, we suggest parameters required for stable dispersions of SWCNTs. We suggest a preferred protein molecular radius of 2–3 nm. This protein size is sufficiently large to wrap around the SWCNTs and sufficiently small so as to not greatly increase the ~1 nm diameter SWCNT. For a globular protein, 2–3 nm corresponds to a molecular weight of 20–100 kDa.[53] In the case of this study, BSA is ~66 kDa and LB1 is ~22 kDa. Another factor that we believe to be necessary to confer stable, individually dispersed SWCNTs is the surfactant-like nature of the protein including the presence of a hydrophobic pocket. BSA (generally, all serum albumin) has a hydrophobic core region for trafficking of fatty acids and small hydrophobic molecules.[54-55] The Ig-fold of LB1 also has a hydrophobic core capable of directly binding to many different protein partners within the cell.[56-57]

5.3.3 SWCNTs-LB1 Enter Cells and Localize to the Nucleus

Since the LB1 protein has a NLS, we hypothesized that the SWCNTs would localize to the nucleus of cells. We added SWCNTs-BSA and SWCNTs-LB1 to HeLa cells and imaged SWCNTs within the cells after 48 h using confocal Raman spectroscopy of the G-band, at ~1590 cm^{-1} (Figure 5.4). Overlays of spatial Raman imaging with phase contrast images showed more SWCNTs in cells treated with SWCNTs-LB1 than in cells treated with SWCNTs-BSA (Figure 5.4A). A delivery of this concentration of ~150 nm long SWCNTs over the entire cells corresponds to approximately $0.67 \pm 0.14 \times 10^6$ SWCNTs-LB1 and 0.39 ±

0.08×10^6 SWCNTs-BSA per cell.[26, 29-30] However, cells treated with SWCNTs-LB1 showed reduced proliferation (Figure 5.5). Focusing on just the nucleus and performing higher spatial resolution scans, we observed localization of SWCNTs mostly at the periphery of the nucleus for SWCNTs-BSA whereas SWCNTs-LB1 localized both at the periphery and inside the nucleus (Figure 5.4B). A confocal Raman G-band Z-scan through the nucleus with the nuclear interior set at Z = 0 μm (Figure 5.4B) showed that the SWCNT intensity was highest at the nuclear center for SWCNTs-LB1 but lowest for SWCNTs-BSA (Figure 5.4C). This confocal quantification confirmed that SWCNTs-LB1 were located inside the volume of the nucleus whereas SWCNTs-BSA were located above and below the nucleus at the nuclear periphery.

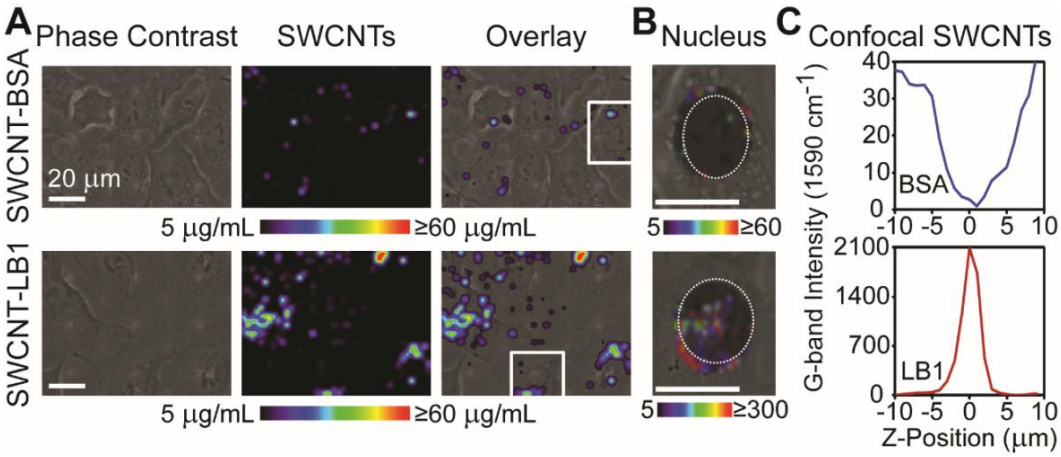

Figure 5.4: Confocal Raman spectroscopy and imaging of SWCNT localization in cells. (A) Phase contrast and confocal Raman spectral mapping overlays of SWCNT G-band intensity show increased cellular internalization for SWCNTs-LB1. The boxed regions indicate individual nuclei that were selected for further confocal spectral mapping and Z-scans. (B) Small step size spectral mapping of the nucleus reveals increased proximity and concentration of SWCNTs in the nucleus for SWCNTs-LB1. Dashed ellipses indicate the outside edge of the nucleus. (C) Confocal Z-scans through the nucleus show SWCNT

intensity in the center of the nucleus is lowest for SWCNTs-BSA, but highest for SWCNTs-LB1.

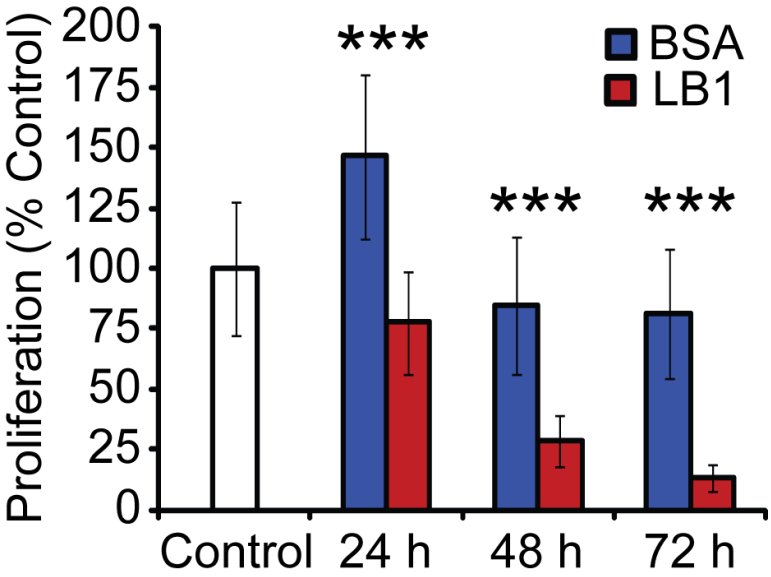

Figure 5.5: Quantification of changes in cell proliferation in response to 24 – 72 h of SWCNT exposure time. SWCNTs-LB1 exposure significantly reduced proliferation compared to SWCNTs-BSA at all exposure times. Data = mean ± SD. ***$p<0.0001$ between BSA and LB1 groups. For control and SWCNTs-BSA treatments, ≥ 2000 total cells on average over ≥ 10 FOV were counted for each exposure time. For SWCNTs-LB1 treatments, ≥ 500 total cells on average over ≥ 10 FOV were counted for each exposure time.

We imaged nanoscale interactions between SWCNTs and DAPI labeled DNA within the nucleus using FLIM. This type of fluorescence imaging measures changes in the fluorescence emission decay rate which is highly sensitive to the surrounding environment of a fluorophore within the Förster radius (~5 nm), including electronic interactions with SWCNTs.[49] SWCNTs significantly reduce the lifetime of fluorophores including rhodamine, Oregon Green, Alexa Fluor 488, and GFP.[2, 46] Treatment with SWCNTs did not obviously alter the fluorescence intensity of the DAPI signal, but we found that cells treated with

SWCNTs-BSA showed slight deviations at the nuclear periphery of some nuclei from a relatively homogeneous mean fluorescence lifetime (τ_m) of ~2.5 ns, similar to control nuclei (Figure 5.6A). In comparison, cells treated with SWCNTs-LB1 had a heterogeneous τ_m throughout the nuclei (Figure 5.6A). Aggregate data from many nuclei showed a singular lifetime peak at ~2.5 ns for DAPI in control nuclei, a slight shoulder for cells treated with SWCNTs-BSA, and a large low lifetime shoulder for SWCNTs-LB1 (Figure 5.6B). The τ_m averaged across all nuclei were statistically significant from one another (Figure 5.6C). The altered τ_m and spatial heterogeneity suggested that SWCNTs-BSA may localize to some degree in the nucleus, perhaps at the nuclear periphery, but SWCNTs-LB1 localize to the nucleus to a larger degree and localize in the nuclear interior.

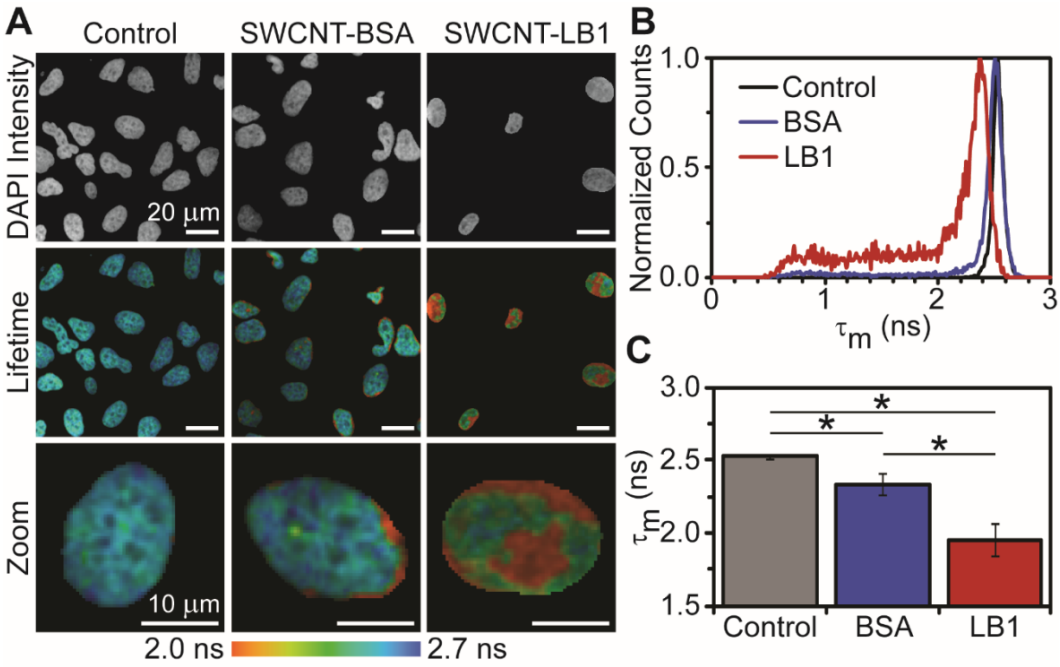

Figure 5.6: Fluorescence lifetime imaging microscopy (FLIM) of DAPI labeled nuclei. (A) Color coded mean fluorescence lifetime (τ_m) images. SWCNTs-BSA treated cell nuclei show a homogeneous distribution of τ_m similar to control with minimal quenched (reduced) τ_m at the periphery of some nuclei, while treatment with SWCNTs-LB1 results in a heterogeneous quenched lifetime throughout nuclei. Selected nuclei are enlarged in the bottom row. Note that each pixel represents a unique data point of τ_m. (B) Histograms of DAPI τ_m for all nuclei normalized to the maximum of each condition show SWCNTs-LB1 shift the distribution of τ_m to lower values. (C) Quantitative comparison of the average τ_m for each condition shows significant quenching for SWCNTs-LB1. Data = mean ± SD. *$p<0.0001$ between indicated groups.

Transport of material into the nucleus through the NPC occurs by diffusion for molecules with a radius smaller than 5 nm, but much larger materials can be actively transported with the aid of an NLS.[58] While protein coated ~1 nm by ~150 nm SWCNTs may have a sufficiently small physical dimension to pass through the NPC by passive diffusion, the large aspect ratio likely inhibits translocation. Other nanomaterials including spherical gold nanoparticles,[6, 59-61] gold nanorods,[62] silver nanoparticles,[63] silica nanoparticles,[64] and quantum dots[65]

have been modified with classical NLSs derived from the Simian virus 40 (SV40) large T-antigen, human immunodeficiency virus type 1 (HIV-1) Tat peptides, and arginine rich import sequences to dramatically enhance nuclear localization.[66-67]

Here, we non-covalently functionalized SWCNTs with a nuclear protein which contains a well-presented NLS. While synthesized peptide sequences offer sufficient specificity for targeting, we find that full proteins can similarly be used to target SWCNTs to subcellular regions while also allowing for multifunctional complexes. Using proteins maintained the sp^2 structure of SWCNTs and preserved the unique properties that facilitated unambiguous measures of SWCNT subcellular localization that may also enable future biomedical applications such as imaging, sensing, ablation, or electrical stimulation. The chemistry and structure of the protein coating itself also offers opportunities to incorporate loading and release of other bioactive molecules. Further, complete, stable coating of LB1 protein may offer better control of the SWCNT interface in complex media or cellular environments compared to minimally covalently functionalized surfaces.

5.3.4 SWCNTs-LB1 Translocate to the Nucleus Within Cells Over Time

We observed that SWCNTs-LB1 did not all localize within the nucleus (Figure 5.4), and we tracked movement within the cell over time. We fixed cells treated with either SWCNTs-BSA or SWCNTs-LB1 at set exposure time points and imaged the localization of SWCNTs directly using NIR fluorescence

microscopy. Visualization of SWCNT NIR fluorescence confirmed that SWCNTs remained stably dispersed within cells; likely SWCNTs well-coated in proteins did not aggregate and quench NIR fluorescence. After 24 h post treatment, we observed SWCNTs within the cell for both SWCNTs-LB1 and SWCNTs-BSA, but neither preferentially localized to the nucleus (Figure 5.7). After 48 h, we observed more SWCNTs within the nucleus for the SWCNTs-LB1, and after 72 h, the SWCNTs-LB1 localized five times more to the nuclear interior compared with SWCNTs-BSA (Figure 5.7, 5.8A).

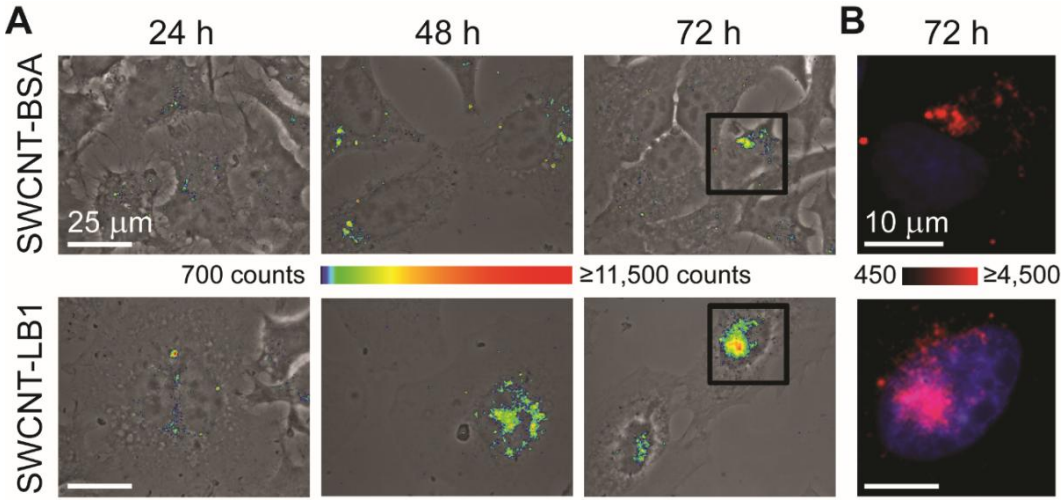

Figure 5.7: NIR fluorescence imaging of SWCNT localization in cells over 24 – 72 h of SWCNT exposure time. (A) Phase contrast and NIR fluorescence imaging overlays of SWCNT NIR fluorescence show SWCNTs-LB1 translocate to the nucleus over time. The boxed regions indicate individual nuclei that were selected and magnified for nuclear co-localization analysis with DAPI stain. NIR fluorescence heat map intensity is represented on a log scale. (B) After 72 h SWCNTs-LB1 NIR fluorescence in red strongly co-localized with DAPI fluorescence in blue labeling DNA in the nucleus. SWCNT NIR fluorescence and DAPI fluorescence are both indexed linearly.

In segmenting regions of the cell, we observed a time-dependent localization of SWCNTs-LB1 from the perinuclear region (P) to the nuclear region (N) over 24 to 48 to 72 h after treatment (Figure 5.8B). At 24 h, cells had similarly limited amounts of SWCNTs-LB1 in both perinuclear and nuclear regions. After 48 h, SWCNTs-LB1 intensity in the perinuclear region doubled that of the nuclear region, while after 72 h, SWCNTs-LB1 intensity transitioned to twice as much in the nuclear region compared to the perinuclear region. We also observed an increase in the percentage of cells with high nuclear accumulation of SWCNTs (*i.e.,* greater average SWCNT intensity in the nucleus than the cytoplasm) over time (Figure 5.8A). The percentage of cells treated with SWCNTs-LB1 with high nuclear accumulation increased from 12% to 19% to 36% over the 24 to 48 to 72 h of treatment. After 72 h, the fraction of cells with significant amounts of SWCNTs in the nucleus was 5 times greater when treated with SWCNTs-LB1 compared to SWCNTs-BSA treatment.

We did observe non-zero fluorescence intensity for SWCNTs-BSA localized with the nucleus of cells, which may result in part from out of plane widefield NIR fluorescence from SWCNTs above and below the volume of the nucleus; this was observed in the confocal Raman spectroscopy Z-scans (Figure 5.4). SWCNTs-BSA signal in the nucleus may also be due to a limited amount of passive diffusion through the NPC or non-specific interactions with the nuclear import machinery.[68] Unlike SWCNTs-LB1, no translocation dynamics were observed for SWCNTs-BSA as intensity in the perinuclear region remained fairly constant over time (Figure 5.8B).

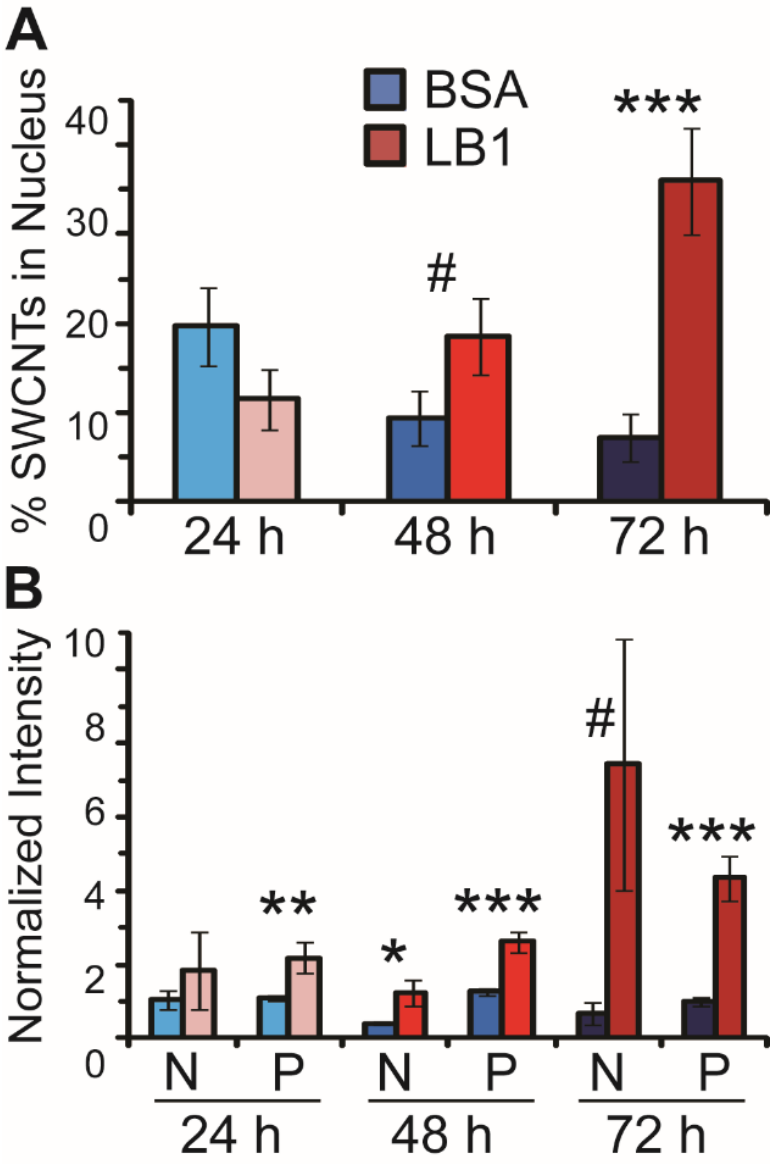

Figure 5.8: Quantification of NIR fluorescence intensity in subcellular regions over 24 – 72 h of SWCNT exposure time. (A) The percentage of cells with a majority of SWCNTs in the nucleus increases over time for SWCNTs-LB1. Data = mean ± SD. (B) SWCNT NIR fluorescence intensity in the nuclear (N) and perinuclear (P) regions normalized to the SWCNT NIR fluorescence intensity in the cytoplasm. SWCNT NIR fluorescence intensity for SWCNTs-LB1 treated cells shows a transition from perinuclear to nuclear regions over time. Data = mean ± SEM. $^{\#}p<0.07$, $^{*}p<0.05$, $^{**}p<0.01$, $^{***}p<0.0001$ between SWCNTs-BSA and SWCNTs-LB1 groups.

Quantifying the kinetics of nanomaterial delivery to the cell and movements within the cell to different compartments is important for designing materials for appropriate therapies. There are numerous timescales to be considered for delivery: cell uptake by endocytosis, endosome escape, intracellular trafficking, and in this case, nuclear import. Previously, we have quantified that cell uptake of SWCNTs-BSA by endocytosis takes only minutes.[28] Many studies have shown uptake of nanomaterials to occur under 1 h.[69] Further, active nuclear translocation rates have been reported as high as 1,000 events per NPC per second.[70] These rates suggest crossing cellular and nuclear membranes happens quickly given sufficient protein interactions with the cellular machinery. Here, we find that the entire process from treatment to nuclear localization takes 72 h, similar to some previous reports.[71] However, this timescale is not universal for all nanomaterials as particle size, shape, geometry, and surface chemistry have significant impacts on nuclear entry and endosome escape. For instance, peptide-targeted gold nanoparticles have been documented in the nucleus of cells after only a few hours of exposure.[59-61] However the ~3–20 nm diameter particles tested were small and spherical in comparison to our ~150 nm SWCNTs used here. Small ~3–4 nm fullerenes[7] and short ~50–100 nm SWCNTs[17, 72] have also been found in nuclei within hours of treatment, despite lacking a nuclear localization type sequence. While direct TEM imaging of similar length (~175 nm) MWCNTs with non-covalent BSA-FITC coating revealed endosomal escape and nuclear entry only after 48 h.[73] This seeming disconnect between delivery (hours) and subcellular processing to the nucleus (days) may represent the

complex processing within the cell. SWCNTs enter cells and need to escape the endosomal compartment. They then diffuse randomly since there is no mechanism of transport along the cytoskeleton, trafficking within a vesicle or otherwise. The NLS of the LB1 coating on the SWCNT, assuming that it survived the enzymatic processing of the late endosome or lysosome, must be in the appropriate conformation to be recognized by the machinery for nuclear import. While the mechanisms underlying the slow cellular processing are still being elucidated, it is important to understand for the purpose of therapeutic design that cellular uptake may be quick but cellular processing is slow.

5.4 Conclusions

Controlling the subcellular delivery of SWCNTs is important for the realization of safe and effective cellular therapies. To overcome limitations of covalent peptide attachment and nonspecific globular proteins, we created nuclear proteins with native biofunctionality. Recombinantly engineered LB1 domains possess essential structural characteristics which allow for effective dispersion of SWCNTs while maintaining their desirable properties. LB1 proteins also enhance the functionality of SWCNTs through the incorporation of a NLS enabling subcellular targeting. We observed translocation of SWCNTs from the cytoplasm to the perinuclear region to the nucleus over 72 h. SWCNTs with LB1, but not BSA, proteins localized to the center of nuclei, quenching the fluorescence lifetime of DAPI labeled DNA. Here, we developed a non-covalent protein based functionalization of SWCNTs that maximizes the availability of SWCNT

properties while imparting controllable subcellular delivery, thereby enabling multifunctional use within cells.

5.5 Acknowledgements

I would like to thank Sairaam Ganesh (Carnegie Mellon University) for collaboration with LB1 protein production and Brian Holt (Carnegie Mellon University) for assistance with FLIM measurements.

5.6 References

1. Holt, B. D.; Short, P. A.; Rape, A. D.; Wang, Y.-l.; Islam, M. F.; Dahl, K. N. Carbon Nanotubes Reorganize Actin Structures in Cells and ex Vivo. *ACS Nano* **2010,** *4*, 4872-4878.

2. Holt, B. D.; Shams, H.; Horst, T. A.; Basu, S.; Rape, A. D.; Wang, Y.-L.; Rohde, G. K.; Mofrad, M. R. K.; Islam, M. F.; Dahl, K. N. Altered Cell Mechanics from the Inside: Dispersed Single Wall Carbon Nanotubes Integrate with and Restructure Actin. *Journal of Functional Biomaterials* **2012,** *3*, 398-417.

3. Zhou, F.; Xing, D.; Wu, B.; Wu, S.; Ou, Z.; Chen, W. R. New Insights of Transmembranal Mechanism and Subcellular Localization of Noncovalently Modified Single-Walled Carbon Nanotubes. *Nano Letters* **2010,** *10*, 1677-1681.

4. Battigelli, A.; Russier, J.; Venturelli, E.; Fabbro, C.; Petronilli, V.; Bernardi, P.; Da Ros, T.; Prato, M.; Bianco, A. Peptide-based carbon nanotubes for mitochondrial targeting. *Nanoscale* **2013,** *5*, 9110-9117.

5. Cheng, J.; Fernando, K. A. S.; Veca, L. M.; Sun, Y.-P.; Lamond, A. I.; Lam, Y. W.; Cheng, S. H. Reversible Accumulation of PEGylated Single-Walled Carbon Nanotubes in the Mammalian Nucleus. *ACS Nano* **2008,** *2*, 2085-2094.

6. Kang, B.; Mackey, M. A.; El-Sayed, M. A. Nuclear Targeting of Gold Nanoparticles in Cancer Cells Induces DNA Damage, Causing Cytokinesis Arrest and Apoptosis. *Journal of the American Chemical Society* **2010,** *132*, 1517-1519.

7. Raoof, M.; Mackeyev, Y.; Cheney, M. A.; Wilson, L. J.; Curley, S. A. Internalization of C60 fullerenes into cancer cells with accumulation in the nucleus via the nuclear pore complex. *Biomaterials* **2012,** *33*, 2952-2960.

8. Ménard-Moyon, C.; Kostarelos, K.; Prato, M.; Bianco, A. Functionalized Carbon Nanotubes for Probing and Modulating Molecular Functions. *Chemistry & Biology* **2010,** *17*, 107-115.

9. Kruss, S.; Hilmer, A. J.; Zhang, J.; Reuel, N. F.; Mu, B.; Strano, M. S. Carbon nanotubes as optical biomedical sensors. *Advanced Drug Delivery Reviews* **2013,** *65*, 1933-1950.

10. Robinson, J.; Welsher, K.; Tabakman, S.; Sherlock, S.; Wang, H.; Luong, R.; Dai, H. High performance in vivo near-IR (>1 μm) imaging and photothermal cancer therapy with carbon nanotubes. *Nano Research* **2010,** *3*, 779-793.

11. Vashist, S. K.; Zheng, D.; Pastorin, G.; Al-Rubeaan, K.; Luong, J. H. T.; Sheu, F.-S. Delivery of drugs and biomolecules using carbon nanotubes. *Carbon* **2011,** *49*, 4077-4097.

12. Dresselhaus, M. S.; Dresselhaus, G.; Eklund, P. C. *Science of Fullerenes and Carbon Nanotubes*. Academic Press: San Diego, 1996.

13. O'Connell, M. J.; Bachilo, S. M.; Huffman, C. B.; Moore, V. C.; Strano, M. S.; Haroz, E. H.; Rialon, K. L.; Boul, P. J.; Noon, W. H.; Kittrell, C.; Ma, J.; Hauge, R. H.; Weisman, R. B.; Smalley, R. E. Band Gap Fluorescence from Individual Single-Walled Carbon Nanotubes. *Science* **2002,** *297*, 593-596.

14. Kaiser, J.-P.; Wick, P.; Manser, P.; Spohn, P.; Bruinink, A. Single walled carbon nanotubes (SWCNT) affect cell physiology and cell architecture. *Journal of Materials Science: Materials in Medicine* **2008,** *19*, 1523-1527.

15. Battigelli, A.; Ménard-Moyon, C.; Da Ros, T.; Prato, M.; Bianco, A. Endowing carbon nanotubes with biological and biomedical properties by chemical modifications. *Advanced Drug Delivery Reviews* **2013,** *65*, 1899-1920.

16. Pantarotto, D.; Briand, J.-P.; Prato, M.; Bianco, A. Translocation of bioactive peptides across cell membranes by carbon nanotubes. *Chemical Communications* **2004**, 16-17.

17. Andreoli, E.; Suzuki, R.; Orbaek, A. W.; Bhutani, M. S.; Hauge, R. H.; Adams, W.; Fleming, J. B.; Barron, A. R. Preparation and evaluation of polyethyleneimine-single walled carbon nanotube conjugates as vectors for pancreatic cancer treatment. *Journal of Materials Chemistry B* **2014,** *2*, 4740-4747.

18. Bekyarova, E.; Sarkar, S.; Wang, F.; Itkis, M. E.; Kalinina, I.; Tian, X.; Haddon, R. C. Effect of Covalent Chemistry on the Electronic Structure and Properties of Carbon Nanotubes and Graphene. *Accounts of Chemical Research* **2012,** *46*, 65-76.

19. Britz, D. A.; Khlobystov, A. N. Noncovalent interactions of molecules with single walled carbon nanotubes. *Chemical Society Reviews* **2006,** *35*, 637-659.

20. Adeli, M.; Soleyman, R.; Beiranvand, Z.; Madani, F. Carbon nanotubes in cancer therapy: a more precise look at the role of carbon nanotube-polymer interactions. *Chemical Society Reviews* **2013,** *42*, 5231-5256.

21. Cherukuri, P.; Gannon, C. J.; Leeuw, T. K.; Schmidt, H. K.; Smalley, R. E.; Curley, S. A.; Weisman, R. B. Mammalian pharmacokinetics of carbon nanotubes using intrinsic near-infrared fluorescence. *Proceedings of the National Academy of Sciences of the United States of America* **2006,** *103*, 18882-18886.

22. Karajanagi, S. S.; Yang, H.; Asuri, P.; Sellitto, E.; Dordick, J. S.; Kane, R. S. Protein-Assisted Solubilization of Single-Walled Carbon Nanotubes. *Langmuir* **2006,** *22*, 1392-1395.

23. Matsuura, K.; Saito, T.; Okazaki, T.; Ohshima, S.; Yumura, M.; Iijima, S. Selectivity of water-soluble proteins in single-walled carbon nanotube dispersions. *Chemical Physics Letters* **2006,** *429*, 497-502.

24. Nepal, D.; Geckeler, K. E. Proteins and Carbon Nanotubes: Close Encounter in Water. *Small* **2007,** *3*, 1259-1265.

25. Edri, E.; Regev, O. "Shaken, Not Stable": Dispersion Mechanism and Dynamics of Protein-Dispersed Nanotubes Studied via Spectroscopy. *Langmuir* **2009,** *25*, 10459-10465.

26. Holt, B. D.; Dahl, K. N.; Islam, M. F. Quantification of Uptake and Localization of Bovine Serum Albumin-Stabilized Single-Wall Carbon Nanotubes in Different Human Cell Types. *Small* **2011,** *7*, 2348-2355.

27. Ge, C.; Du, J.; Zhao, L.; Wang, L.; Liu, Y.; Li, D.; Yang, Y.; Zhou, R.; Zhao, Y.; Chai, Z.; Chen, C. Binding of blood proteins to carbon nanotubes reduces cytotoxicity. *Proceedings of the National Academy of Sciences of the United States of America* **2011,** *108*, 16968-16973.

28. Holt, B. D.; Dahl, K. N.; Islam, M. F. Cells Take up and Recover from Protein-Stabilized Single-Wall Carbon Nanotubes with Two Distinct Rates. *ACS Nano* **2012,** *6*, 3481-3490.

29. Holt, B. D.; McCorry, M. C.; Boyer, P. D.; Dahl, K. N.; Islam, M. F. Not all protein-mediated single-wall carbon nanotube dispersions are equally bioactive. *Nanoscale* **2012,** *4*, 7425-7434.

30. Boyer, P. D.; Holt, B. D.; Islam, M. F.; Dahl, K. N. Decoding membrane- versus receptor-mediated delivery of single-walled carbon nanotubes into

macrophages using modifications of nanotube surface coatings and cell activity. *Soft Matter* **2013,** *9*, 758-764.

31. Calvaresi, M.; Zerbetto, F. The Devil and Holy Water: Protein and Carbon Nanotube Hybrids. *Accounts of Chemical Research* **2013,** *46*, 2454-2463.

32. Dhe-Paganon, S.; Werner, E. D.; Chi, Y.-I.; Shoelson, S. E. Structure of the Globular Tail of Nuclear Lamin. *Journal of Biological Chemistry* **2002,** *277*, 17381-17384.

33. Ruan, J.; Xu, C.; Bian, C.; Lam, R.; Wang, J.-P.; Kania, J.; Min, J.; Zang, J. Crystal structures of the coil 2B fragment and the globular tail domain of human lamin B1. *FEBS Letters* **2012,** *586*, 314-318.

34. Talcott, B.; Moore, M. S. Getting across the nuclear pore complex. *Trends in Cell Biology* **1999,** *9*, 312-318.

35. Ganesh, S.; Qin, Z.; Spagnol, S. T.; Biegler, M. T.; Coffey, K. A.; Kalinowski, A.; Buehler, M. J.; Dahl, K. N. The tail domain of lamin B1 is more strongly modulated by divalent cations than lamin A. *Nucleus* **2015**, DOI: 10.1080/19491034.2015.1031436.

36. Kalinowski, A.; Qin, Z.; Coffey, K.; Kodali, R.; Buehler, Markus J.; Lösche, M.; Dahl, Kris N. Calcium Causes a Conformational Change in Lamin A Tail Domain that Promotes Farnesyl-Mediated Membrane Association. *Biophysical Journal* **2013,** *104*, 2246-2253.

37. Qin, Z.; Kalinowski, A.; Dahl, K. N.; Buehler, M. J. Structure and stability of the lamin A tail domain and HGPS mutant. *Journal of Structural Biology* **2011,** *175*, 425-433.

38. Wunderlich, Z.; Acton, T. B.; Liu, J.; Kornhaber, G.; Everett, J.; Carter, P.; Lan, N.; Echols, N.; Gerstein, M.; Rost, B.; Montelione, G. T. The protein target list of the Northeast Structural Genomics Consortium. *Proteins: Structure, Function, and Bioinformatics* **2004,** *56*, 181-187.

39. Islam, M. F.; Milkie, D. E.; Torrens, O. N.; Yodh, A. G.; Kikkawa, J. M. Magnetic heterogeneity and alignment of single wall carbon nanotubes. *Physical Review B* **2005,** *71*, 201401.

40. Johnston, D. E.; Islam, M. F.; Yodh, A. G.; Johnson, A. T. Electronic devices based on purified carbon nanotubes grown by high-pressure decomposition of carbon monoxide. *Nature Materials* **2005,** *4*, 589-592.

41. Islam, M. F.; Rojas, E.; Bergey, D. M.; Johnson, A. T.; Yodh, A. G. High Weight Fraction Surfactant Solubilization of Single-Wall Carbon Nanotubes in Water. *Nano Letters* **2003,** *3*, 269-273.

42. Arnold, M. S.; Green, A. A.; Hulvat, J. F.; Stupp, S. I.; Hersam, M. C. Sorting carbon nanotubes by electronic structure using density differentiation. *Nature Nanotechnology* **2006,** *1*, 60-65.

43. Becker, M. L.; Fagan, J. A.; Gallant, N. D.; Bauer, B. J.; Bajpai, V.; Hobbie, E. K.; Lacerda, S. H.; Migler, K. B.; Jakupciak, J. P. Length-Dependent Uptake of DNA-Wrapped Single-Walled Carbon Nanotubes. *Advanced Materials* **2007,** *19*, 939-945.

44. Fagan, J. A.; Becker, M. L.; Chun, J.; Hobbie, E. K. Length Fractionation of Carbon Nanotubes Using Centrifugation. *Advanced Materials* **2008,** *20*, 1609-1613.

45. Huang, Y. Y.; Knowles, T. P. J.; Terentjev, E. M. Strength of Nanotubes, Filaments, and Nanowires From Sonication-Induced Scission. *Advanced Materials* **2009,** *21*, 3945-3948.

46. Yaron, P.; Holt, B.; Short, P.; Lösche, M.; Islam, M.; Dahl, K. Single wall carbon nanotubes enter cells by endocytosis and not membrane penetration. *Journal of Nanobiotechnology* **2011,** *9*, 45.

47. Duncan, R. R.; Bergmann, A.; Cousin, M. A.; Apps, D. K.; Shipston, M. J. Multi-dimensional time-correlated single photon counting (TCSPC) fluorescence lifetime imaging microscopy (FLIM) to detect FRET in cells. *Journal of Microscopy* **2004,** *215*, 1-12.

48. Köllner, M.; Wolfrum, J. How many photons are necessary for fluorescence-lifetime measurements? *Chemical Physics Letters* **1992,** *200*, 199-204.

49. Berezin, M. Y.; Achilefu, S. Fluorescence Lifetime Measurements and Biological Imaging. *Chemical Reviews* **2010,** *110*, 2641-2684.

50. Becker, W. *The bh TCSPC handbook*. 3rd ed.; Becker & Hickl GmbH: Berlin, Germany, 2008.

51. Heller, D. A.; Barone, P. W.; Swanson, J. P.; Mayrhofer, R. M.; Strano, M. S. Using Raman Spectroscopy to Elucidate the Aggregation State of Single-Walled Carbon Nanotubes. *Journal of Physical Chemistry B* **2004,** *108*, 6905-6909.

52. Bachilo, S. M.; Strano, M. S.; Kittrell, C.; Hauge, R. H.; Smalley, R. E.; Weisman, R. B. Structure-Assigned Optical Spectra of Single-Walled Carbon Nanotubes. *Science* **2002,** *298*, 2361-2366.

53. Erickson, H. Size and Shape of Protein Molecules at the Nanometer Level Determined by Sedimentation, Gel Filtration, and Electron Microscopy. *Biological Procedures Online* **2009,** *11*, 32-51.

54. Carter, D. C.; Ho, J. X. Structure of Serum Albumin. *Advances in Protein Chemistry* **1994,** *45*, 153-203.

55. Curry, S. Lessons from the Crystallographic Analysis of Small Molecule Binding to Human Serum Albumin. *Drug Metabolism and Pharmacokinetics* **2009,** *24*, 342-357.

56. Simon, D. N.; Wilson, K. L. The nucleoskeleton as a genome-associated dynamic 'network of networks'. *Nature Reviews Molecular Cell Biology* **2011,** *12*, 695-708.

57. Simon, D.; Wilson, K. Partners and post-translational modifications of nuclear lamins. *Chromosoma* **2013,** *122*, 13-31.

58. Panté, N.; Kann, M. Nuclear Pore Complex Is Able to Transport Macromolecules with Diameters of ~39 nm. *Molecular Biology of the Cell* **2002,** *13*, 425-434.

59. Nativo, P.; Prior, I. A.; Brust, M. Uptake and Intracellular Fate of Surface-Modified Gold Nanoparticles. *ACS Nano* **2008,** *2*, 1639-1644.

60. Ryan, J. A.; Overton, K. W.; Speight, M. E.; Oldenburg, C. N.; Loo, L.; Robarge, W.; Franzen, S.; Feldheim, D. L. Cellular Uptake of Gold Nanoparticles Passivated with BSA−SV40 Large T Antigen Conjugates. *Analytical Chemistry* **2007,** *79*, 9150-9159.

61. de la Fuente, J. M.; Berry, C. C. Tat Peptide as an Efficient Molecule To Translocate Gold Nanoparticles into the Cell Nucleus. *Bioconjugate Chemistry* **2005,** *16*, 1176-1180.

62. Oyelere, A. K.; Chen, P. C.; Huang, X.; El-Sayed, I. H.; El-Sayed, M. A. Peptide-Conjugated Gold Nanorods for Nuclear Targeting. *Bioconjugate Chemistry* **2007,** *18*, 1490-1497.

63. Austin, L. A.; Kang, B.; Yen, C.-W.; El-Sayed, M. A. Plasmonic Imaging of Human Oral Cancer Cell Communities during Programmed Cell Death

by Nuclear-Targeting Silver Nanoparticles. *Journal of the American Chemical Society* **2011,** *133*, 17594-17597.

64. Pan, L.; He, Q.; Liu, J.; Chen, Y.; Ma, M.; Zhang, L.; Shi, J. Nuclear-Targeted Drug Delivery of TAT Peptide-Conjugated Monodisperse Mesoporous Silica Nanoparticles. *Journal of the American Chemical Society* **2012,** *134*, 5722-5725.

65. Chen, F.; Gerion, D. Fluorescent CdSe/ZnS Nanocrystal−Peptide Conjugates for Long-term, Nontoxic Imaging and Nuclear Targeting in Living Cells. *Nano Letters* **2004,** *4*, 1827-1832.

66. Nakielny, S.; Dreyfuss, G. Transport of Proteins and RNAs in and out of the Nucleus. *Cell* **1999,** *99*, 677-690.

67. Marfori, M.; Mynott, A.; Ellis, J. J.; Mehdi, A. M.; Saunders, N. F. W.; Curmi, P. M.; Forwood, J. K.; Bodén, M.; Kobe, B. Molecular basis for specificity of nuclear import and prediction of nuclear localization. *Biochimica et Biophysica Acta, Molecular Cell Research* **2011,** *1813*, 1562-1577.

68. Nabiev, I.; Mitchell, S.; Davies, A.; Williams, Y.; Kelleher, D.; Moore, R.; Gun'ko, Y. K.; Byrne, S.; Rakovich, Y. P.; Donegan, J. F.; Sukhanova, A.; Conroy, J.; Cottell, D.; Gaponik, N.; Rogach, A.; Volkov, Y. Nonfunctionalized Nanocrystals Can Exploit a Cell's Active Transport Machinery Delivering Them to Specific Nuclear and Cytoplasmic Compartments. *Nano Letters* **2007,** *7*, 3452-3461.

69. Jin, H.; Heller, D. A.; Sharma, R.; Strano, M. S. Size-Dependent Cellular Uptake and Expulsion of Single-Walled Carbon Nanotubes: Single Particle Tracking and a Generic Uptake Model for Nanoparticles. *ACS Nano* **2009,** *3*, 149-158.

70. Ribbeck, K.; Görlich, D. Kinetic analysis of translocation through nuclear pore complexes. *EMBO Journal* **2001,** *20*, 1320-1330.

71. Treuel, L.; Jiang, X.; Nienhaus, G. U. New views on cellular uptake and trafficking of manufactured nanoparticles. *Journal of the Royal Society Interface* **2013,** *10*, 20120939.

72. Kang, B.; Chang, S.; Dai, Y.; Yu, D.; Chen, D. Cell Response to Carbon Nanotubes: Size-Dependent Intracellular Uptake Mechanism and Subcellular Fate. *Small* **2010,** *6*, 2362-2366.

73. Mu, Q.; Broughton, D. L.; Yan, B. Endosomal Leakage and Nuclear Translocation of Multiwalled Carbon Nanotubes: Developing a Model for Cell Uptake. *Nano Letters* **2009,** *9*, 4370-4375.

6 Non-covalent Ternary Dispersions of Single Wall Carbon Nanotubes for Controlled Cellular Delivery

6.1 Introduction

A major barrier to drug delivery is the ability to achieve optimal intracellular therapeutic concentrations at low exposure doses that minimize systemic effects. Establishing precise control of intracellular delivery of drugs with toxic or broad physiologic effects is crucial for the prevention of adverse off-target and systemic responses and the realization of effective therapy. Nanomaterials with physicochemical properties that promote cell internalization and are tunable at the length scales of molecular drugs are being intensely investigated to improve the delivery of poorly water-soluble drugs as well as new classes of bioactive macromolecules through cell-specific targeting and controlled intracellular release.[1] Single wall carbon nanotubes (SWCNTs) possess essential physical characteristics for drug delivery vehicles including their small size, which allows for efficient internalization of large number of SWCNTs, coupled with their high surface area which allows for extensive molecular loading and multi-functionalization. SWCNTs also possess unique mechanical, thermal, electrical, and optical properties[2] providing the additional advantages of *in situ* sensing,[3] imaging,[4] and thermal ablation[5] at the sites of delivery.

SWCNTs are hydrophobic and readily aggregate in aqueous environments due to strong van der Waals forces forming SWCNT bundles which have

deleterious cell effects[6] and reduced optical properties.[7] Thus, for biomedical applications SWCNTs must first be dispersed through covalent or non-covalent functionalizations. There are numerous chemical strategies to increase the solubility of SWCNTs which also provide reactive groups for easy attachment of drugs.[8] Drugs may be attached either directly for enhanced stability or through enzymatic cleavable linkers to promote release. Topoisomerase inhibitors, platinum-based drugs, antifolates, antimitotic drugs, and antimicrobials have been loaded onto SWCNTs with pH, protease, esterase, and thiol liable chemistries.[9] However, chemical modification of SWCNTs attenuates desirable properties for multi-modal applications while chemistry to the drug molecule may alter its therapeutic activity.[10] Non-covalent dispersions using biocompatible phospholipids, copolymers, and proteins are preferred to preserve SWCNT properties.[11-12] Further, the physicochemical properties of some polycyclic aromatic drugs including doxorubicin, methotrexate, and paclitaxel have proven well-suited for enabling direct adsorption to SWCNTs forming supramolecular complexes via π-stacking.[9] However, the loading efficiency and control of release is often dependent on the ionization state of the molecule in its current environment.[13]

To enable more generic control of polycyclic drug molecule loading onto SWCNT while maintaining dispersion and SWCNT properties and to promote cellular specific release, we considered biocompatible dispersing agents that could maintain interaction with both drug molecules and SWCNTs. Globular albumin proteins have a structure that facilitates remarkable transport properties for native

hydrophobic molecules including fatty acids as well as proclivity for binding exogenous drugs in the blood stream, impacting their eventual tissue distribution.[14-15] Albumin has been shown to accumulate in solid tumors and inflamed joints of arthritic disease due to the enhanced permeability of the local vasculature as well as the energy source it provides for tumor growth and synovial cells with highly up-regulated metabolisms.[16] Designed therapeutic systems carried by albumin including paclitaxel in Abraxane for treating metastatic breast cancer and insulin derivatives in Levemir for treating diabetes are already on the marketplace.[17] Our group and others have used bovine serum albumin (BSA) to non-covalently disperse SWCNTs which preserves inherent SWCNT properties allowing for multifunctional applications and promotes high levels of cell internalization (~tens of millions per cell) into HeLa cells[18] and macrophages.[19] We hypothesized that anti-cancer and anti-inflammatory drugs bound to BSA could be used to non-covalently disperse SWCNTs. The resulting ternary complex would serve to solubilize drugs, sequester their bioactivity until released from the complex, and dramatically increase the efficiency of drug delivery to cells improving therapeutic effectiveness.

Here, we perform molecular docking studies which identify separate binding locations and characteristics within BSA for SWCNTs and drugs. Using rhodamine B (RB) as a fluorescent model drug molecule, we characterize the loading and release of molecules from our ternary complex dispersion *in vitro* and in cells. *In vitro* we find release is triggered quickly by denaturation or enzymatic digestion of BSA. In cells we observe slower cell type dependent separation of

RB from SWCNTs over time using fluorescence lifetime imaging microscopy (FLIM) of RB and direct near-infrared (NIR) fluorescence imaging of SWCNTs. Ternary complex dispersions with topoisomerase inhibitor daunomycin (DM) or corticosteroids prednisone (PRD) and prednisolone (PSL) had increased effectiveness in cells inhibiting HeLa cell proliferation and suppressing the production of key inflammatory cytokine interleukin (IL)-1β in macrophages to greater extents than free or BSA-bound drug.

6.2 Materials and Methods

6.2.1 BSA-SWCNT Complex Modeling

Docking: The PatchDock[20-21]/FireDock[22-23] webservers were used for all docking analyses. In the first phase, the crystal structure of the BSA molecule (PDB ID: 4F5S) was used as the receptor, while each of the SWCNT chiralities in the solution for NIR fluorescence intensity measurements was submitted individually as the ligand molecule to the PatchDock server.[20-21] Both geometrical compatibility and interaction energies were used to estimate favorability of BSA-SWCNT binding modes. Then from the PatchDock output, the first 1,000 most favorable binding modes were submitted to FireDock for further surface refinement. After the PatchDock binding modes were re-ranked, the new top 10 modes were selected by FireDock.[22-23] We then clustered similar binding modes into more distinct modes based on spatial adjacency.

In the second phase, the BSA molecule was equilibrated in a water box using molecular dynamics (MD) simulation prior to performing any docking analyses. Although the BSA backbone was not significantly displaced during equilibration, the side chains were re-adjusted causing a notable alteration in the protein surface. Therefore, docking analyses resulted in notably different binding modes, and the number of clusters was also changed.

It should be noted that the initial SWCNTs used were 1 nm in length which showed a strong tendency to interact with BSA *via* their tips. This seemed to be an artifact of having finite size SWCNTs. Therefore, we chose longer SWCNTs (~1.5 nm) based on comparison with the largest principal axis of BSA that increased the likelihood of lateral binding formation.

Molecular Dynamics: Only a subset of the most prominent SWCNT chiralities were selected for further MD simulations. The NAMD 2.9 molecular dynamics package[24] and CHARMM27 forcefield[25] were used for all MD studies. BSA and SWCNT complexes were solvated using the TIP3P explicit water model in order to improve the model accuracy. Then, counter ions were included to neutralize the excess charge of the system followed by setting the overall ion concentration to 150 mM. The MD time-step was 2 fs and periodic boundary conditions were applied in all directions. In the NPT ensemble, pressure and temperature were kept constant at 1 bar and 310 K using Langevin Piston and Langevin dynamics,[26] respectively.

The system was minimized for 50,000 steps in order to remove all bad contacts. This was followed by an equilibration simulation for 1 ns. Each model

then ran for 5 ns which was considered as the production run and was then post-processed. System coordinates along with system properties (*e.g.*, temperature, energies, *etc.)* were recorded every 20 ps. All energy calculations and visualization were performed using visual molecular dynamics software (VMD).[27]

6.2.2 SWCNT Purification and Length Fractionation

Unpurified high pressure carbon monoxide conversion synthesis (HiPCO) SWCNTs (Carbon Nanotechnologies, Inc.) with diameters of 1 ± 0.3 nm and polydisperse lengths were purified to remove amorphous carbon and metal impurities according to previously described methods.[28-29] Thermogravimetric analysis and wide-angle X-ray scattering confirmed that the purified sample contained < 5 wt% carbonaceous impurities and ~0.3 wt% metallic impurities, with the rest of the sample being unaltered SWCNTs.[28-29]

Purified SWCNTs were dispersed in water using sodium deoxycholate (DOC) and centrifuged at 21,000×*g* for 2 h to remove remaining SWCNT bundles according to previous methods.[30-31] Individualized SWCNTs were length fractionated using density gradient ultracentrifugation.[32] SWCNTs in the 10^{th}-12^{th} fractions with lengths of 145 ± 17 nm were collected[33] and subsequently pelleted and burned at 300 °C in wet air in the presence of H_2O_2 to remove DOC and then washed in water several times.

6.2.3 SWCNT Ternary Complex Dispersion and Molecular Loading

We describe the procedure in detail for RB. The methods for daunomycin (DM), prednisone (PRD), and prednisolone (PSL) were similar except where noted. RB was dissolved in ultrapure deionized water (resistivity 18.3 MΩ/cm, total oxidizable carbon < 5 ppb) at 600 μM. For PRD and PSL solutions, a brief probe-tip sonication (Fisher Scientific, Model 100; 3 mm tip diameter) at 6 W was performed to assist in solubilization. Bovine serum albumin (BSA) was dissolved separately also in ultrapure deionized water at 300 μM. Equal volumes of RB and BSA solutions were mixed to achieve a final solution of 1 wt% BSA and a 2:1 molar ratio of RB:BSA . The BSA-RB mixture was incubated overnight at 4 °C in the dark to promote full infiltration of RB into BSA hydrophobic cavities.

SWCNTs were non-covalently dispersed in BSA-RB using methods described previously for BSA.[18-19, 34-35] Briefly, the starting SWCNT concentration was set at 0.1 wt%. The mixture of BSA-RB and SWCNTs were dispersed in water using a probe-tip sonicator (Fisher Scientific, Model 100; 3 mm tip diameter) at 6 W for 2 h. Under these conditions, the ~150 nm SWCNTs were not shortened from sonication induced scission.[36] To separate bundles from isolated SWCNTs, suspensions were centrifuged at 21,000×*g* for 7 min (Beckman Coulter Allegra 25R Centrifuge with a TA-15-1.5 rotor). To remove RB and BSA that were not complexed with SWCNTs, the supernatant was diluted in ultrapure deionized water and ultracentrifuged at 60,000 rpm (308,450×*g* max) for 2 h to pellet the SWCNTs (Beckman Coulter Optima L-100K Ultracentrifuge with a Type 90Ti rotor). The pellet was wash 3 times with ultrapure deionized

water and resuspended at the initial concentration in only deionized water using a brief probe-tip sonication (Fisher Scientific, Model 100; 3 mm tip diameter) at 6 W for 30 min. Afterwards, residual bundles were separated from isolated SWCNTs through centrifugation of the suspension at 21,000×*g* for 7 min. The supernatants were collected and used immediately for cell experiments without sterilization to prevent photobleaching.

6.2.4 SWCNT Ternary Complex Dispersion Characterization

UV-vis-NIR absorbance spectroscopy: To quantitatively determine SWCNT concentration and qualitatively assess dispersion quality, SWCNT dispersions were examined using UV-vis-NIR absorbance spectroscopy (Varian Cary 5000 UV-vis-NIR spectrophotometer). Concentration was determined using an extinction coefficient of 2.6 (absorbance mL)/(mg mm) at 930 nm.[32] The sharpness and intensity of the van Hove peaks qualitatively indicate dispersion quality.[7]

Raman spectroscopy: SWCNT structure after dispersion was characterized with Raman spectroscopy. Samples diluted to 0.3 absorbance/cm in water were analyzed on an inverted, inVia confocal Raman microscope (Renishaw) using a 50× air objective with 0.75 numerical aperture (NA) and a 785 nm laser (100 mW). Spectra were acquired between 100 – 3200 cm^{-1}. The data were normalized by the G-band intensity. The D-band-to-G-band intensity ratio (I_D:I_G) was calculated by dividing the D-band intensity at ~1300 cm^{-1} by the G-band intensity.

NIR fluorescence spectroscopy: SWCNT dispersion quality was characterized with NIR fluorescence spectroscopy (Horiba Jobin Yvon Nanolog spectrofluorometer). SWCNT samples were diluted to 0.3 absorbance/cm in water and NIR fluorescence spectra were collected with a 60 s integration time and excitation and emission slit widths of 10 nm using a liquid nitrogen cooled detector (Symphony InGaAs-1700). The excitation grating was 1200 grooves/mm and blazed at 500 nm and the emission grating was 150 grooves/mm and blazed at 1200 nm. NIR fluorescence heatmaps of corrected fluorescence intensity normalized to excitation intensity were constructed using FluorEscence and Nanosizer software with chirality peak fits generated using a Voight 2D model. SWCNT quantum yield (QY) was determined at 2 different wavelengths corresponding to different major chiralities in the sample. The total corrected SWCNT NIR fluorescence signal per absorbance was normalized to fluorescence per absorbance of NIR dye indocyanine green with known quantum efficiency with the same system parameters.

6.2.5 Quantification of Loaded Molecules

To determine the loading of RB or DM on SWCNTs, ultracentrifuged and re-dispersed SWCNTs-BSA-RB or SWCNTs-BSA-DM were subjected to UV-vis-NIR absorbance spectroscopy. The peak absorbance of RB at ~567 nm or ~483 nm for DM above SWCNTs-BSA baseline at the corresponding wavelength was used to determine the concentration of RB or DM in the sample using a standard curve relating BSA-RB or BSA-DM absorbance and concentration. Note

that the peak absorbance of RB with SWCNTs-BSA-RB was shifted from typical RB peak absorbance at ~555 nm alone in water or with BSA. A similar ~10 – 20 nm red shift of DM with SWCNTs-BSA-DM was observed, but DM absorbance was weak and broad with interference from SWCNT contributing additional uncertainty to the peak height and location. For PRD and PSL, which absorb in the UV at ~244 nm and ~247 nm, respectively, the high absorbance of SWCNTs makes similar calculations difficult. For these samples, the supernatant from the SWCNT ternary complex ultracentrifugation step, combined with the pellet washes, was ultracentrifuged again to produce a SWCNT free supernatant. The concentration of PRD and PSL was then determined from a standard curve relating BSA-PRD or BSA-PSL absorbance and concentration. The fraction of initial PRD or PSL in the supernatant was then used to estimate the loaded concentration of the SWCNT ternary complex sample. For RB, this indirect method was found to overestimate the loaded concentration by as much as ~300%, which assumes a mass balance where no RB was lost to the non-dispersed SWCNT pellet. However, for initial experiments involving SWCNTs-BSA-PRD and SWCNTs-BSA-PSL, the indirect method was still used to determine loaded concentration and dosing.

6.2.6 Stimulated *In Vitro* RB Release

RB fluorescence spectroscopy measurements were performed on a Horiba Jobin Yvon Nanolog spectrofluorometer. Sample excitation was fixed at 550 nm with a 2 nm slit width. Emission spectra were collected from 555 – 615 nm with 1

nm step size and 2 nm slit width. Both excitation and emission gratings were 1200 grooves/mm blazed at 500 nm. For quantification of fluorescence changes, the maximum corrected fluorescence intensity at ~575 nm normalized to the excitation intensity was used. All fluorescence measurements were normalized by the absorbance of the sample at 550 nm using a Varian Cary 5000 UV-vis-NIR spectrophotometer.

Temperature: SWCNTs-BSA-RB was diluted to 11.6 μg/mL (containing 2 μM loaded RB concentration) in ultrapure deionized water. Fluorescence and absorbance measurements of SWCNTs-BSA-RB and BSA-RB or RB only at 2 μM were taken from 10 – 85 °C in 5 °C intervals. Measurements were also made at 37 °C and the denaturation temperature of native BSA, ~68 °C. Temperature was controlled using FluorEscence software with a thermoelectric temperature controller (Wavelength Electronics). Measurements were made 5 min after each new temperature set point was reached to allow sufficient time for samples to reach equilibrium. Temperature controller response time between set point changes was quick, so that the total amount of time between measurements remained consistent throughout the duration of the experiment at ~5 min.

Trypsin: 1.35 mL of 11.6 μg/mL SWCNTs-BSA-RB was equilibrated at 37 °C and then diluted with 0.15 mL of 37 °C equilibrated 2.5% (w/v) trypsin in Hank's Balanced Salt Solution (HBSS) without phenol red (Corning). The sample was pipetted up and down 5 times to ensure a well-mixed solution with a new effective 1.8 μM RB concentration. Fluorescence and absorbance measurements

of SWCNTs-BSA-RB and BSA-RB or RB only at equivalent concentrations were taken over time starting immediately after mixing up to 2 h with initial measurements every 30 s. Similar measurements were repeated with ultrapure deionized water instead of trypsin at 37 °C and 80 °C.

6.2.7 Cell Culture and Treatment

J774A.1 mouse macrophage-like cells (ATCC) were cultured in Dulbecco's Modified Eagle's Medium (DMEM; 4500 mg/L glucose, 4.0 mM L-glutamine, without sodium pyruvate; Thermo Scientific Hyclone), supplemented with 10% v/v fetal bovine serum (FBS; Invitrogen) and 1% v/v penicillin-streptomycin (Invitrogen). HeLa cells were cultured in DMEM (1000 mg/L glucose, 4.0 mM L-glutamine, with 110 mg/L sodium pyruvate; Thermo Scientific Hyclone), supplemented with 10% v/v FBS (Invitrogen) and 1% v/v penicillin-streptomycin (Invitrogen). Cells were maintained at 37 °C and 5% CO_2.

6.2.8 Quantification of RB Delivery to Cells

J774A.1 cells were seeded at 1×10^4 cells/cm^2, and HeLa cells were seeded at 3×10^4 cells/cm^2 onto sterilized #1.5 coverslips and maintained in culture for 24 h. Subsequently, cells were exposed to SWCNTs-BSA-RB diluted in fresh media at concentrations of 1 and 10 μg/mL for 48 h. Side by side control exposures were performed similarly with RB and BSA-RB (2:1 molar ratio) at concentrations equal to the determined loaded RB concentration for SWCNTs, as well as 1 wt% BSA and no treatment. After 48 h, the media containing treatments

was removed. Cells were washed 6 times in PBS and fixed with 3.7% v/v formaldehyde (Sigma-Aldrich) for 15 min in the dark and mounted onto glass slides. Cells were imaged in phase contrast, brightfield, and fluorescence (with N2.1 filter cube for RB) on a Leica DMI 6000B inverted light and fluorescence microscope using a 0.6 NA air condenser and a 40× (0.75 NA) oil immersion objective. For each condition, ≥ 4 fields of view with an average total ≥ 800 cells for J774A.1 and ≥ 450 cells for HeLa were analyzed. As cells were mostly confluent, the average RB fluorescence intensity per pixel per field of view was quantified in ImageJ and normalized to the number of cells for that particular field of view. The average RB intensity per cell for each treatment condition was normalized to the average intensity per cell for untreated samples.

6.2.9 SWCNT NIR Fluorescence Imaging

Phase contrast imaging and widefield NIR fluorescence imaging were performed on an inverted, Leica DMI 4000 light and fluorescence microscope using a 0.9 NA air condenser and a 100× (1.4 NA) oil immersion objective. A 785 nm laser (120 mW, CrystaLaser) that was decohered and expanded to fill the objective back focal plane and a 320 pixel × 256 pixel liquid nitrogen cooled 2D InGaAs camera (2D-OMA V, Princeton Instruments) were interfaced with the microscope *via* a custom setup to obtain widefield SWCNT NIR fluorescence images. Control of imaging parameters and processing were performed using WinView software (Princeton Instruments). For NIR imaging, NIR fluorescence intensity between 900 – 1700 nm was collected after dark current background

correction for integration times ≥ 20 s. Spatial maps of SWCNT NIR fluorescence intensity above noise (~50 counts/s) were performed in WinView software. SWCNT NIR fluorescence images were overlaid with visible fluorescence images taken on the same system for RB and DM (with Y5 filter cube).

6.2.10 Fluorescence Lifetime Imaging and Analysis

FLIM was performed as previously reported by our group[37-38] on a Leica TCS SP5 inverted laser scanning confocal microscope using a 100× (1.4 NA) oil immersion objective. A tunable mode-locked Ti:sapphire 80 MHz pulsed laser (Chameleon, Coherent) served at the multiphoton excitation source. For RB, the multiphoton laser was tuned to 850 nm, and wavelengths of 516 – 724 nm were passed to a photomultiplier tube to detect the full range of RB emission. Time-correlated single photon counting (TCSPC) was performed using a Becker & Hickl SPC-830 counting board and controlled with SPCM software (Becker & Hickl). To enable an accurate determination of exponential decays and to minimize the coefficient of variation, 256 pixel × 256 pixel lifetime images were acquired at a scan rate of 400 Hz for at least 180 s with 220 time channels and a measurement window of 10.8 ns.[39-40] SPCImage software (Becker & Hickl) was used to calculate the lifetime fits per pixel and render spatial lifetime images using binning, as necessary, to achieve peak photon counts of ≥ 1,000.[40-41]

The calculated single (τ_1) and double exponential (τ_1 and τ_2) decay lifetimes, along with their relative magnitudes and corresponding goodness of fits (χ^2), were analyzed in MATLAB.[37] For double exponential decays, the mean

fluorescence (τ_m) lifetime was used to represent the data, which is the weighted average of τ_1 and τ_2. FLIM images were photon peak intensity thresholded in SPCImage (Becker & Hickl) to exclude background pixels from analysis. All reported values of lifetime are the average value of τ_m averaged across n = 5 analyzed images per experimental condition. Note that each included (*i.e.*, non-thresholded) pixel represents a unique data point of τ_m.

6.2.11 Quantification of Anti-Proliferative Effects from DM Delivery

HeLa cells were seeded at 3×10^4 cells/cm^2 onto sterilized #1.5 coverslips and maintained in culture for 24 h. Subsequently, cells were exposed to SWCNTs-BSA-DM diluted in fresh media at a concentration of 1 μg/mL for 48 h. Side by side control exposures were performed similarly with DM and BSA-DM (2:1 molar ratio) at concentrations equal to the determined loaded DM concentration for SWCNTs, as well as 1 wt% BSA and no treatment. After 48 h, the media containing treatments was removed. Cells were washed 3 times in PBS and fixed with 3.7% v/v formaldehyde for 15 min in the dark and mounted onto glass slides. Cells were imaged in phase contrast and fluorescence (with N2.1 filter cube) on a Leica DMI 6000B inverted light and fluorescence microscope using a 0.6 NA air condenser and a 40× (0.75 NA) oil immersion objective. For each condition, ≥ 10 fields of view with an average total ≥ 400 cells were analyzed. Proliferation was determined as a percentage of cells normalized to control cell count.

6.2.12 Flow Cytometry and Quantification of Anti-Inflammatory Effects from PRD and PSL Delivery

Macrophages were seeded at 2.5×10^4 cell/cm^2 into 6-well plates, allowed to adhere for 1 h, and treated immediately afterwards. Cells were exposed to 1 μg/mL SWCNTs-BSA-PRD or SWCNTs-BSA-PSL. Side by side control exposures were performed similarly with PRD or PSL and BSA-PRD or BSA-PSL (2:1 molar ratio) at concentrations equal to the determined loaded PRD (~16 nM) or PSL (~44 nM) concentrations for SWCNT ternary complexes. Treatments with 1 μg/mL SWCNTs-BSA or equivalent 1 wt% BSA solution along with untreated cells were used as controls. All exposures were for 46 h. Afterwards, the treatment media was removed for all cells and replaced with fresh media containing 1 μg/mL lipopolysaccharide (LPS) to stimulate an inflammatory response for 16 h. Note the negative control cells received neither drug treatment nor LPS stimulation.

After LPS challenge, 1.5 μL of protein transport inhibitors containing Monensin (BD GolgiStop) or Brefeldin A (BD GolgiPlug) were added to all cells for 2 h. The supernatant was collected and stored at -80 °C for cytokine analysis. Cells were lifted off of the surface using a cell scraper and washed 1 time in PBS. Cell suspensions were transferred to smaller staining tubes and portion of each sample was taken to build immunoglobulin (Ig) isotype and unstained controls. Cell suspensions were incubated for 5 min with Fc Block (BD Biosciences) and then stained with fluorochrome conjugated antibodies (BD Biosciences) against

surface markers CD40 and MHC class II IAb for 25 min at room temperature in the dark followed by two washes in PBS. Cells were fixed and permeabilized for 20 min (BD Cytofix/Cytoperm). The cell cytoplasm was stained with appropriate fluorochrome conjugated antibodies (BD Biosciences) against inflammatory proteins and cytokines MyD88, NF-κB, IL-1β, TNF-α, and IL-6 for 25 min at room temperature in the dark. Cell suspensions were washed 3 times in 1× BD Perm/Wash and 1 time in PBS followed by storage in 2% w/v paraformaldehyde in PBS until analysis. Control cells were incubated with the appropriate species-specific IgG isotype conjugated with the same fluorochrome following the same procedure, and used to measure intrinsic cell fluorescence.

Raw cytometric data were acquired using the LSRII cytometer (BD Biosciences). Cytometer efficiency and signal compensation were established for each fluorochrome using calibration beads (Spherotec). Live cells were electronically gated using forward and side scatter profiles. Single cells were discriminated by height *versus* width plot of the forward scatter. Signal intensities of antigen-specific staining were normalized against a compensation matrix constructed from signals of the calibration beads and control cells. Cell populations were analyzed offline using FlowJo software (Tree Star). Kolmogorov-Smirnov (K-S) and chi-square probability binning algorithms were used to quantitatively compare differences in populations relative to the untreated control. Cell response was quantified using the geometric mean fluorescence intensities (GMFIs) of the labeled proteins within each treatment group in the

form of a stimulation index (SI): SI = (GMFI treatment sample)/(GMFI untreated control sample).

6.3 Results and Discussion

6.3.1 BSA Pockets are Versatile and Allow for Loading SWCNTs with Many Different Molecules

Structurally, albumin is composed of 3 homologous domains (named I, II, and III) with each domain containing two separate helical subdomains (named A and B).[14] The folded protein forms an asymmetric heart shaped structure with a cleft-like region between domains IB and IIIB. The unique arrangement of α-helices within the subdomains of albumin gives rise to several pre-formed cavities which have been found to bind a wide range of drug molecules.[14-15] Binding and crystallography studies have determined two main drug sites in domains IIA and IIIA referred to as drug sites 1 and 2, respectively.[15] To determine how albumin non-covalently associates with SWCNTs and whether albumin drug sites remain available, we performed molecular docking studies to identify favorable binding modes followed by all-atom molecular dynamic (MD) simulations on solvated BSA molecules and several chiralities of SWCNTs including (7,6), (8,6), (9,4), and (10,2) with diameters between 0.87 – 0.95 nm. Equilibrated BSA from initial MD simulations and SWCNTs were submitted to PatchDock, where both geometrical compatibility and interaction energies were used to estimate the most favorable SWCNT-BSA binding modes.[20-21] The binding modes were further

refined in FireDock, and the top 10 modes were selected and clustered into more distinct modes based on spatial adjacency for further MD studies.[22-23] We found that the most energetically favorable (between -105 and -130 kcal/mol) binding modes for all SWCNTs occurred within the cleft-like region between domains IB and IIIB (Figure 6.1A). As anticipated, the hydrophobic residues showed a notable affinity for SWCNTs. All SWCNT axes aligned almost perfectly on top of each other showing that they positioned approximately at the same point of the BSA surface.

We further compared the BSA inter-domain interaction energies in the presence and absence of SWCNT. The interaction energy in the cleft-like region between domains IB and IIIB ranged between 0 and -100 kcal/mol even in the absence of SWCNT indicating that the cleft was flexible and leaped between closed and open states several times. The (9,4) SWCNT promoted this interaction for 3 ns, but eventually it was disrupted (average energy = -48 kcal/mol). The interaction between adjacent domains IA and IIIA was weak but negative in most simulations. We suggest that the flexibility of size and shape of the cleft could be one reason for the observation of a common binding mode for all SWCNTs since it allows for necessary adjustments with rigid SWCNT ligands. Moreover, there are other binding modes occurring within the same cleft that are rotated relative to the best modes but are not as energetically favorable (Figure 6.1B).

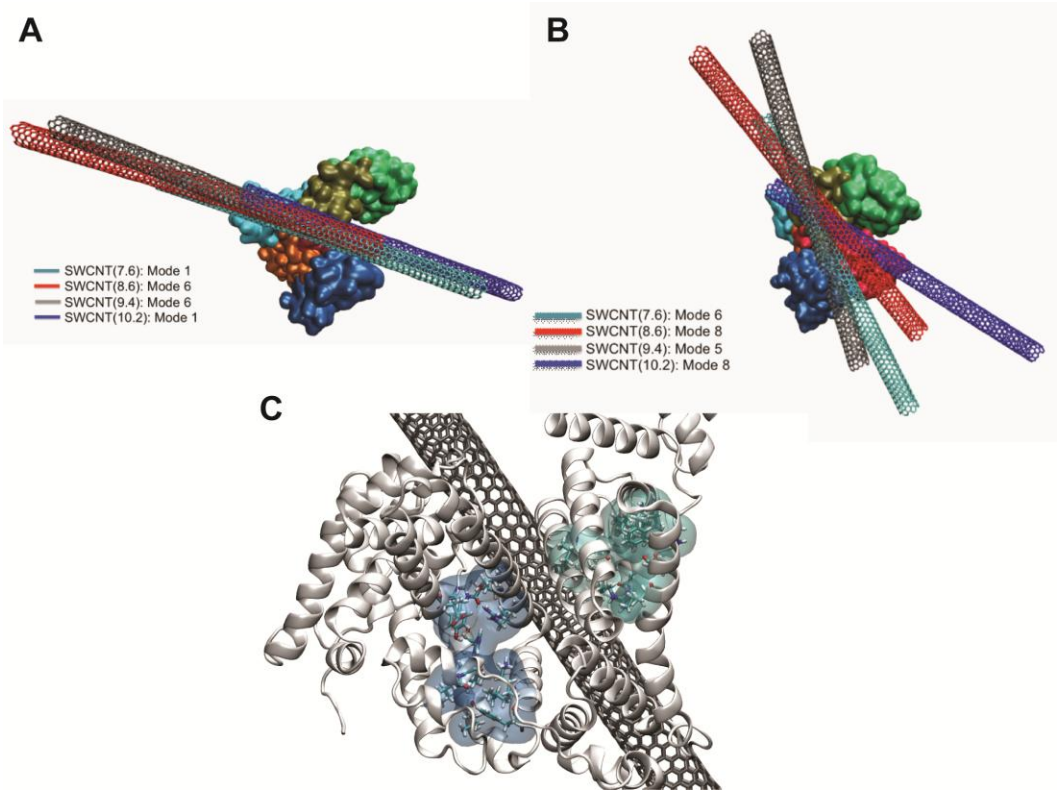

Figure 6.1: Complex formation between BSA and SWCNTs. (A) The lowest interaction energy binding modes from molecular docking for 4 different SWCNT chiralities show a similar preference for association with BSA in the cleft region formed between subdomains IB (red) and IIIB (light green). (B) SWCNT binding occurs at many different orientations within the BSA cleft with slightly less favorable interaction energies indicating flexibility in the BSA cleft for accommodating rigid SWCNTs. (C) Energetically favorable SWCNT binding modes in the BSA cleft do not directly involve interactions with albumin drug binding cavities colored in blue.

Through further analysis of amino acids involved in the association with ligands in albumin drug binding sites, we determined that these sites were not directly involved in promoting interactions with SWCNTs in the energetically favored binding modes within the BSA cleft (Figure 6.1C). The average center of mass distance between pockets comprising the drug binding sites in albumin and

bound SWCNT was determined to be ~2.7 nm. Thus, drugs and SWCNTs may complex BSA simultaneously in spatially distinct, but nearby locations.

Crystallography studies have revealed the drug binding cavities contain asymmetric hydrophobic and polar features which have been found to preferentially bind to drugs with similar physicochemical characteristics.[14] Drug site 1 in domain IIA is slightly larger and contains polar residues in the middle of two nonpolar chambers, thus showing specificity for binding flat aromatic compounds with centrally located negatively charged features.[15] RB was determined through competitive binding experiments to bind to site 1 for RB:BSA molar ratios < 50,[42] showing structural similarities to other site 1 binders including phenylbutazone and warfarin.[15] Drug site 2 in domain IIIA is more compact, but with a completely solvent accessible entrance lined with polar residues shows affinity for aromatic compounds with peripherally located electronegative features.[15] PSL was found to associate in site 2 by molecular docking[43] with similar peripheral negative charged features as recognized site 2 binders including ibuprofen and diazepam.[15] Thus, the diverse binding of BSA to small hydrophobic anionic molecules enables many different molecules to be loaded on to SWCNTs. Furthermore, specific site 1 and site 2 biding drugs may be combined for multimodal delivery accentuating the versatility of BSA and the ternary complex.

6.3.2 SWCNTs-BSA-RB Ternary Complex Formation

We first chose to study ternary complex formation with the fluorophore molecule RB. RB has similar size and structure to other small molecule therapeutics, and the fluorescent properties of RB allow for facile spectroscopic characterization and imaging in cells. To develop the SWCNT ternary complex dispersion, we first solubilized RB *via* hydrophobic binding sites in the BSA. We quantified the fluorescence quenching of the tryptophan amino acid near site 1 and determined that RB bound to BSA with $K_d \sim 2.1 \times 10^{-5}$ M at ~0.9:1 stoichiometry, similar to previous reports.[42] Subsequently, the BSA-RB complex was used to disperse SWCNTs in water through sonication. Similar to BSA by itself, we found that the BSA-RB complex produced high yield dispersions with sharp van Hove peaks in absorbance indicative of individually dispersed SWCNTs (Figure 6.2A). In order to determine the amount of RB loaded onto SWCNTs *via* BSA, we carried out a sedimentation, washing, and re-dispersion sequence to remove unbound RB and BSA-RB from SWCNTs-BSA-RB. Through this process, we were able to retain > 80% of the initial mass yield of the dispersion as well as dispersion quality indicated by the persistence of narrow van Hove peak widths in the NIR. We found this method to be more efficient for protein dispersions compared to other reported dialysis or filtration procedures. The ~20% reduction in mass yield is consistent with the effects of additional centrifugation time on dispersion mass yield previously reported by our group.[18] The presence of RB on the well-dispersed SWCNTs was clearly visible due to the dark red coloring of the solution as well as an additional strong absorbance peak

>10 times above SWCNT absorbance in the visible region (Figure 6.2A). We determined the amount of RB loaded onto SWCNTs by quantifying the height of the RB absorbance peak above SWCNTs-BSA baseline for a dispersion of equivalent concentration and quality. We calculated solution concentrations of ~66 μM RB for SWCNT concentrations of ~385 μg/mL. For our ~150 nm SWCNTs we approximated a loading of 37 ± 7 RB per SWCNT.

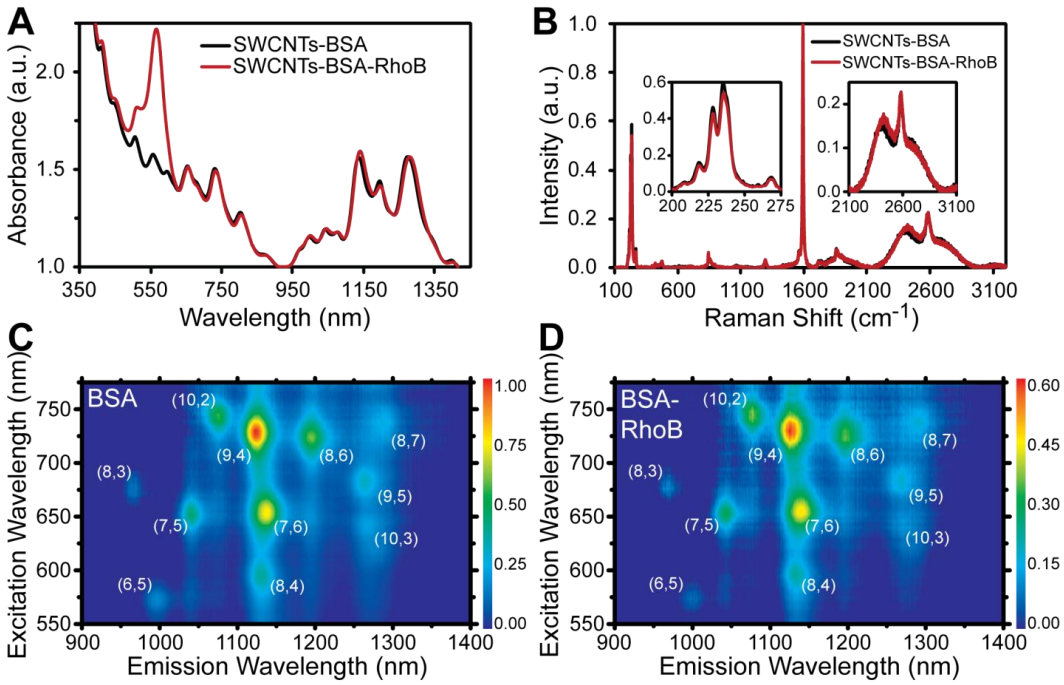

Figure 6.2: Optical characterization of SWCNT ternary complex dispersion with BSA-RB. (A) UV-vis-NIR absorbance spectroscopy of SWCNTs-BSA and SWCNTs-BSA-RB. The sharp peaks arise from the van Hove singularities of the density of states indicating individually dispersed SWCNTs. For SWCNTs-BSA-RB, the intense absorbance peak at ~550 nm results from RB loaded onto SWCNTs after removal of unbound RB though ultracentrifugation and re-dispersion in water. (B) Raman spectroscopy of SWCNTs-BSA and SWCNTs-BSA-RB confirms the dispersions maintain SWCNT structure with low I_D:I_G ratio and result in minimal aggregation with NIR fluorescence. The insets magnify the radial breathing modes (200-275 cm^{-1}) and the broad peak (~2100-3100 cm^{-1}) resulting from unfiltered real space SWCNT NIR fluorescence. (C-D) NIR

fluorescence spectroscopy heat maps show SWCNT fluorescence intensity confirming the presence of individual SWCNTs for both SWCNTs-BSA and SWCNTs-BSA-RB with a similar distribution of chiralities. The dynamic range in both maps is scaled to the maximum NIR fluorescence intensity for SWCNTs-BSA.

We further characterized the SWCNTs-BSA-RB ternary complex dispersion using characteristic Raman spectral features including the G-band at ~1590 cm^{-1} resulting from sp^2-hybridized carbon, the D-band at ~1300 cm^{-1} from sp^3-hybridized carbon, and radial breathing modes (RBMs) at 200-275 cm^{-1} (Figure 6.2B).[44] The intensity ratio between the D-band and G-band was < 0.04 and similar to SWCNTs-BSA and starting SWCNT power which confirmed that the dispersion process maintained SWCNT structure. Both SWCNTs-BSA-RB and SWCNTs-BSA had minimal RBM intensity > 250 cm^{-1}, which corresponds to SWCNT bundles for the 1.58 eV (785 nm) laser line used. Furthermore, we observed unfiltered real-space NIR fluorescence at ~2300 cm^{-1} in the Raman spectra confirming the presence of individually dispersed SWCNTs.[45]

To quantitatively assess dispersion quality and electronic interactions within the ternary complex, we performed NIR fluorescence spectroscopy on SWCNT dispersions. Individually dispersed semiconducting SWCNTs emit NIR fluorescence at distinct wavelengths corresponding to the band gap energies of different SWCNT chiralities,[46] whereas bundles containing metallic SWCNTs quench fluorescence.[7] We found that SWCNTs-BSA-RB contained individually dispersed SWCNTs similar to SWCNTs-BSA as evidenced by NIR fluorescence from multiple different chiralities shown in a fluorescence intensity heat map over

excitation and emission wavelengths (Figure 6.2C-D). The distribution of chiralities was similar for SWCNTs-BSA-RB with < 1% difference in relative abundance of each chirality, except for (9,4) which was reduced by 3%, relative to SWCNTs-BSA. Compared to BSA protein alone, the interaction of BSA-RB contributed an additional red shift of ~4.7 meV and ~3.1 meV to average excitation and emission maxima, respectively, determined from peak fits of fluorescence intensity. The quantum yield (QY) of SWCNTs-BSA-RB was determined to be ~0.011%, which was ~1.3 times less than the QY of ~0.015% for SWCNTs-BSA, despite having nearly identical absorbance and Raman dispersion characteristics.

Here, we observed BSA-RB complexes load RB molecules onto SWCNTs in what appears to be the primary mechanism of SWCNTs-BSA-RB complex formation. We also observed electronic interactions between RB and SWCNTs suggesting some RB may adsorb directly onto the SWCNT surface via π-stacking adding to the loaded concentration. RB has been observed to directly disperse SWCNTs at favorable efficiencies compared to other fluorophores.[47] Here, we found that RB alone did not disperse SWCNTs at the same concentration used for BSA-RB dispersions. RB absorbance was peak shifted from ~555 nm, alone or with BSA, to ~567 nm with SWCNTs. Further, RB fluorescence was reduced, but not peak shifted, suggesting some form of contact or static quenching *via* the formation of a non-fluorescent ground state complex.[48] Additionally, SWCNTs-BSA-RB NIR absorbance peaks were red shifted ~3 nm and broadened 2 – 3 nm in width compared to SWCNTs-BSA. We also observed SWCNTs-BSA-RB QY

was ~1.3 times less than SWCNTs-BSA. Similar drops in QY despite good dispersion quality have been reported for adsorption of other aromatic compounds including doxorubicin and pyrenes which perturbed the electronic structure of SWCNTs through π-stacking resulting in reduced exciton lifetimes leading to fluorescence quenching and broadening of optical transitions.[49] Despite the additional contributions of RB, we saw almost no difference in the relative abundance of different dispersed chiralities between SWCNTs-BSA-RB and SWCNTs-BSA suggesting BSA still maintains the primary role of dispersant.

6.3.3 Disruption of BSA *In Vitro* Triggers Release of RB from SWCNTs-BSA-RB Ternary Complex

Since we found that RB molecules could be effectively loaded onto SWCNTs *via* interactions with BSA, we hypothesized that RB could be released by inducing specific disruptions to the adsorbed BSA. Intracellularly, proteins are chemically degraded and denatured through proteolyic enzymes, pH, and other conditions in lysosomes. To test our hypothesis *in vitro*, we exposed SWCNTs-BSA-RB to denaturing heat to alter protein conformation and enzymatic digestion with trypsin to cleave protein structure. To determine whether RB was still bound to SWCNTs, we measured the relative quenching of RB fluorescence intensity. SWCNTs are known to quench the fluorescence of many fluorophores, including RB,[48] through distant dependent energy transfer (*i.e.*, Förster resonance energy transfer; FRET) or electron transfer mechanisms.[50] Thus, we considered increases

in RB fluorescence intensity to infer decoupling of RB from SWCNTs and indicate release from the ternary complex.

We observed initial fluorescence intensity from SWCNTs-BSA-RB complex which was ~82% quenched compared to the fluorescence of unbound SWCNTs-BSA and RB mixed together in solution which we used to represent the maximum fluorescence intensity from a completely decomplexed system. We exposed SWCNTs-BSA-RB to increasing temperature from 12 °C to 85 °C and calculated the change in RB fluorescence relative to the starting intensity at 12 °C (Figure 6.3A). Note that the quantum efficiency of RB is temperature dependent,[51] so we used the fluorescence change of RB solution alone at the same starting intensity as the baseline for calculations. As temperature increased, BSA denatured, and SWCNTs-BSA-RB fluorescence intensity increased following a sigmoidal behavior with inflection point at ~37 °C leading to a maximum increase of ~57%. The maximum steady state fluorescence intensity at 80 °C for thermal denaturing of the ternary complex corresponded to ~85% of the maximum intensity of the completely decomplexed system, indicating as much as 15% of the loaded RB may be irreversibly bound to SWCNTs. We observed only ~3% fluorescence intensity increase from BSA-RB complexes without SWCNTs over the same temperature range indicating that separation from SWCNTs is the main driving force behind the increased fluorescence.

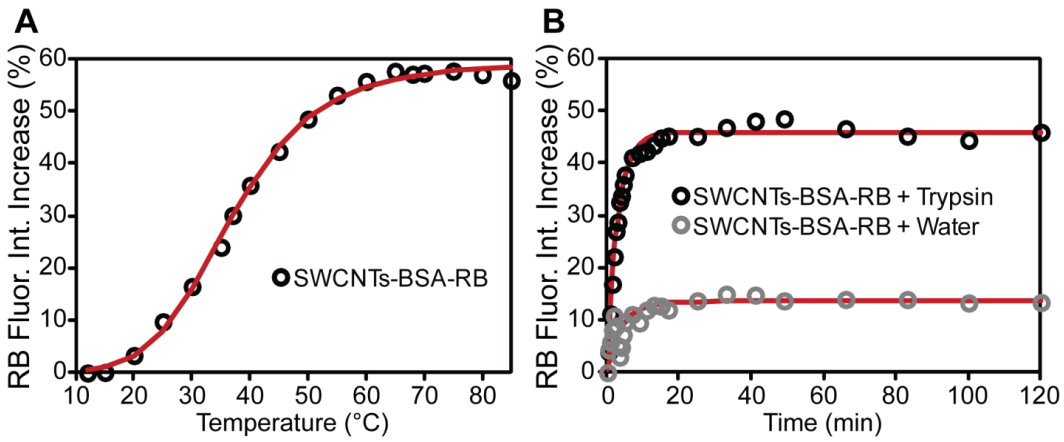

Figure 6.3: Quantification of SWCNTs-BSA-RB fluorescence intensity changes in response to thermal or enzymatic degradation of BSA. (A) SWCNTs-BSA-RB fluorescence intensity increases largely around 40 °C indicating separation from the fluorescence quenching SWCNT complex with little increase beyond the denaturation temperature of native BSA at ~68 °C. Red line represents fit to 4 parameter logistic curve. (B) SWCNTs-BSA-RB fluorescence intensity increases rapidly after typsin treatment indicating fast dissociation from the complex before reaching steady state after 20 min. Without trypsin, RB fluorescence intensity increases to a lower steady state value at slower rate. Red lines represent fit to a first order rate law assuming first order kinetic release from the SWCNT complex. Non-linear fits give rate constants $k_{trypsin}$ = 0.327 ± 0.025 min^{-1} and k_{water} = 0.232 ± 0.093 min^{-1}, where ± represent 95% confidence intervals to the fitted parameter.

We also quantified release over 2 h from SWCNTs-BSA-RB at 37 °C using the protease trypsin to enzymatically cleave BSA (Figure 6.3B). Fluorescence intensity increased rapidly after the addition of trypsin before reaching a plateau of ~46% increase. Similar experiments with BSA-RB complexes without SWCNTs showed a slower increase in fluorescence to a maximum ~6% increase. We compared this enzyme specific release to non-specific release over the same times at 37 °C with ultrapure deionized water added instead of trypsin. We observed a kinetically slower process with ~14% increased fluorescence intensity for SWCNTs-BSA-RB and a slight ~1% decrease

in fluorescence intensity for BSA-RB complexes only. Modeling RB release from SWCNTs using first order release kinetics showed a significantly higher rate constant for trypsin-mediated release, $k_{trypsin} = 0.327 \pm 0.025$ min^{-1}, compared to non-specific release in water, $k_{water} = 0.232 \pm 0.093$ min^{-1}, where ± represent 95% confidence intervals. The maximum steady state fluorescence intensity with trypsin treatment was ~35% of the maximum intensity of the completely decomplexed system compared to ~31% without trypsin. We found the maximum steady state fluorescence intensity at 37 °C without treatment corresponded to ~27% of the maximum intensity of the completely decomplexed system. Thus, specific trypsin enzyme activity was ~2 – 3 times more effective in inducing RB release compared to non-specific dilution in water, which resulted in only ~4% of the maximum possible release.

Initially, the SWCNTs-BSA-RB ternary dispersion complex showed non-zero RB fluorescence intensity, which was ~18% of the maximum fluorescence intensity from a completely decomplexed system. This indicated that a fraction of RB molecules or BSA-RB complexes may have initially been free in solution or adsorbed to SWCNTs in orientations that exclude RB molecules from energy or electron transfer with SWCNTs. Nevertheless, we still observed significant increases in fluorescence intensity which revealed decomplexation of SWCNTs-BSA-RB with denaturation or proteolysis of BSA. RB may be released from binding sites within BSA immobilized on SWCNTs or from entire BSA-RB complexes leaving SWCNTs. The smaller increase in fluorescence intensity for enzymatic treatment may be the result of RB molecules that remain pinned

between protein fragments and SWCNTs or remain stuck within partially digested protein fragments still on SWCNTs. Whereas heat treatment may completely disrupt the entire BSA protein conformation and thus SWCNT-BSA interaction, trypsin activity is more selective in the digest of specific amino acid residues. At 37 °C steady state fluorescence measurements showed ~27% of the maximum intensity of the completely decomplexed system, suggesting that at least 2/3 of loaded RB molecules are still available for specific or long-term release in cells. Further, the decomplexation of RB from SWCNTs-BSA-RB was found to be highly sensitive to changes in temperature around 37 °C. This heightened sensitivity could allow the strong NIR absorption and high thermal conductivity of SWCNTs to be used locally to trigger SWCNT heating and disruption of BSA promoting increased intracellular release to specific cells.

6.3.4 SWCNTs-BSA-RB Ternary Complex Increases Delivery of RB to Cells

Since SWCNTs-BSA-RB ternary complex produced good quality dispersions with high loading of releasable RB, we next determined whether SWCNTs could serve as efficient vectors to deliver RB, or other loaded molecules, to different cell types. We exposed HeLa cells and mouse macrophages to 1 and 10 μg/mL SWCNTs-BSA-RB for 48 h and quantified the intracellular delivery of RB through widefield fluorescence imaging microscopy (Figure 6.4A-B). To assess the efficiency of SWCNTs, we also imaged cells treated with only RB or BSA-RB at equivalent concentrations to the amount of

RB loaded on SWCNTs. HeLa cells exposed to 1 μg/mL SWCNTs-BSA-RB showed a small but statistically significant ~1.2-fold increase in RB delivery compared to RB or BSA-RB alone (Figure 6.4C). Higher concentrations of SWCNTs showed similarly modest ~1.2-fold increases, suggesting additional delivered RB molecules may still be trapped on SWCNTs and thus were not visible to our fluorescence based assay. For macrophages treated with 1 μg/mL SWCNTs-BSA-RB we quantified a ~5-fold increase in delivery (Figure 6.4D). Increasing the exposure concentration to 10 μg/mL resulted in a ~20-fold enhancement in RB delivery. The substantial increase in SWCNT effectiveness for macrophages is likely facilitated by the high amounts of SWCNT uptake for this cell type and suggests substantial uptake of the SWCNT vector is essential for enhanced RB delivery effect. Thus, SWCNTs are a useful vector for delivery where the quantity and specificity of SWCNT uptake can be used to control the intracellular dosage and selectivity of loaded drugs. Further, cell types with higher cellular activity (*e.g.*, uptake, proteolysis, *etc.*) may be further sensitized to lower treatment doses based on intracellular processing and release of the loaded molecule, while more long term release kinetics may be explored in less active cells.

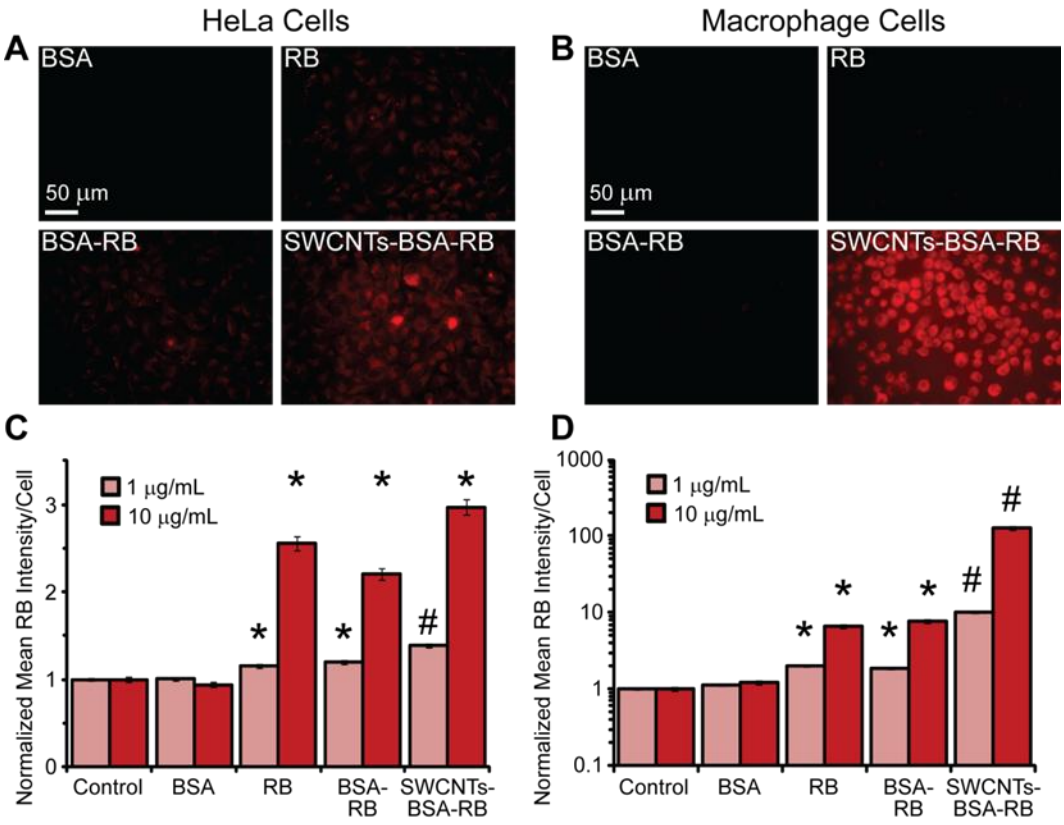

Figure 6.4: Fluorescence imaging and quantification of RB delivered to HeLa cells and J774A.1 macrophages. (A-B) Widefield fluorescence images for (A) HeLa cells and (B) macrophages exposed to 10 μg/mL SWCNTs-BSA-RB or equivalent concentration of loaded RB and BSA-RB for 48 h. (C-D) Quantification of mean widefield RB fluorescence intensity normalized to total cells for exposure to 1 or 10 μg/mL SWCNTs-BSA-RB and equivalent loaded RB concentrations for 48 h. Data = mean ± SEM, *$p < 0.001$ compared to control, $^{\#}p < 0.001$ compared to RB and BSA-RB.

6.3.5 RB is Released from SWCNTs-BSA-RB Ternary Complex Over Time in Cells

We examined the localization of RB relative to SWCNTs over time in cells using fluorescence lifetime imaging microscopy (FLIM). FLIM measures changes in the decay rate of fluorescence emission from a fluorophore which is highly sensitive to the local environment of the fluorophore within typical energy

transfer distances (~5 nm), including electronic interactions with SWCNTs.[52] SWCNTs have been shown to significantly quench the lifetime of fluorophores including RB based actin probes in cells.[38] Thus, FLIM provides details at length scales relevant for studying RB release from SWCNTs offering an enhancement from standard diffraction limited real-space imaging with typical optical resolution of ~200 nm. Macrophages treated with 10 μg/mL SWCNTs-BSA-RB for 24 h showed a significantly quenched homogeneous mean fluorescence lifetime (τ_m) of ~1.0 ns compared to macrophages treated with equal concentrations of only RB with homogeneous τ_m of ~2.6 ns (Figure 6.5A). The dramatic and consistent reduction in RB lifetime suggested all RB molecules were still attached to SWCNTs after 24 h in cells. When we followed the SWCNTs-BSA-RB treatment in macrophages out to 48 h, we observed a return of nearly all internalized RB lifetimes to the RB only treatment state with τ_m of ~2.3 ns. Most cells had a few subcellular regions of quenched lifetime while the majority of lifetime signal in the cytoplasm appeared to be non-quenched indicating RB had largely been released from SWCNTs. A histogram of quantified lifetimes from the images revealed that 24 h treatment with SWCNTs-BSA-RB shifted the distribution of τ_m to significantly lower values (Figure 6.5B). After 48 h of SWCNTs-BSA-RB treatment, the distribution of τ_m in macrophages was almost completely shifted back to the RB only τ_m distribution with only a minor contribution from reduced lifetime observed at earlier exposure times. Thus, over 48 h in macrophages, τ_m transitioned from quenched to non-quenched suggesting

that macrophages are able to intracellularly liberate RB from SWCNT ternary complexes (Figure 6.5C). Similar treatment and imaging in HeLa cells revealed a bimodal τ_m after 48 h, with the distribution more heavily weighted to quenched lifetimes. The bimodal distribution resulted in an average τ_m of ~1.5 ns, suggesting intracellular release is less efficient or occurs on longer timescales in HeLa cells compared to macrophages, likely due to differential cellular processing including higher protein digestive activity in macrophages.

.

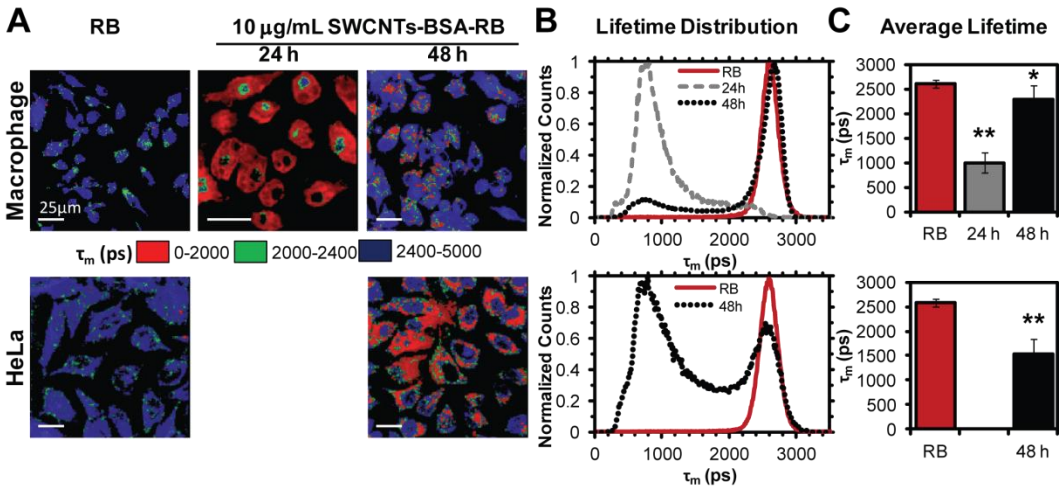

Figure 6.5: Fluorescence lifetime imaging microscopy (FLIM) of RB in macrophages and HeLa cells over 24 – 48 h of SWCNT exposure time. (A) Color coded mean fluorescence lifetime (τ_m) images. After 24 h of SWCNTs-BSA-RB exposure, macrophages show a homogeneous distribution of reduced (quenched) τ_m compared with exposure to only RB. After 48 h of SWCNTs-BSA-RB exposure, τ_m largely returns to RB only exposure lifetimes for macrophages with a few remaining quenched regions, while HeLa cells show a heterogeneous distribution of quenched τ_m through the cytoplasm. Note that each pixel represents a unique data point of τ_m. (B) Histograms of RB τ_m for all cells normalized to the maximum of each condition show 24 h SWCNTs-BSA-RB exposure shifts the distribution of τ_m to significantly lower values for macrophages. After 48 h SWCNTs-BSA-RB exposure, macrophages show a nearly complete return to the RB only distribution, while the distribution of τ_m remains bimodal in HeLa cells. (C) Quantitative comparison of the average τ_m for

each condition shows significant quenching for 24 h SWCNTs-BSA-RB exposure in macrophages returns close to RB only average τ_m after 48 h. The average τ_m for HeLa cells exposed to SWCNTs-BSA-RB remains significantly quenched after 48 h. Data = mean ± SD, **p<0.0001, *p<0.05 compared to RB.

Since FLIM is an indirect measure of SWCNT and RB subcellular localization, we also performed direct real-space imaging of both components in cells to confirm RB release. We utilized the inherent NIR fluorescence of individual semiconducting SWCNTs to unambiguously track SWCNT position in cells without the assistance of other fluorescence labels. For macrophages after 48 h of 10 μg/mL SWCNTs-BSA-RB treatment, overlaid widefield fluorescence images of RB and SWCNT NIR fluorescence showed a low degree of spatial correlation between RB and SWCNTs (Figure 6.6). A majority of RB fluorescence intensity appeared to be located towards the center of cells while SWCNT NIR fluorescence intensity was largely located at the cell periphery. SWCNT locations are not devoid of RB fluorescence, but RB intensity in these regions is much less than other regions in the cell. SWCNT NIR fluorescence also indicates the presence of individual SWCNTs, suggesting that the BSA has not yet been disrupted to the extent of inducing SWCNT-SWCNT contact and NIR fluorescence quenching.

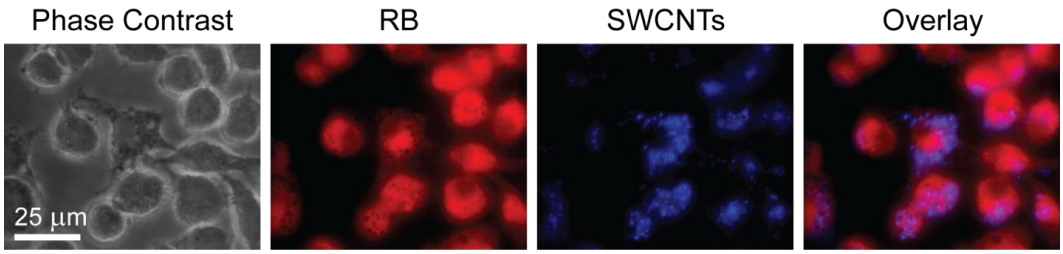

Figure 6.6: Fluorescence imaging of RB and SWCNT localization in macrophages after 48 h exposure to 10 μg/mL SWCNTs-BSA-RB. NIR fluorescence imaging overlays of SWCNT NIR fluorescence with RB fluorescence show a majority of subcellular locations with spatially separate SWCNTs and RB.

In vitro, we observed fast release kinetics from SWCNTs-BSA-RB on the order of minutes, whereas in cells, we found subcellular release requires additional time on the order of hours. Further the efficiency and time scales of intracellular RB release were cell type dependent, suggesting cell specific contributions to the release of RB. Macrophages are known to have high protein digestive activity and showed intracellular release of nearly all RB from 24 to 48 hours of exposure. HeLa cells on the other hand showed incomplete release with many subcellular regions still containing a majority of SWCNT-bound RB after 48 h exposure. This could explain why significant increases in RB fluorescence intensity concurrent with uptake were observed for macrophages but not for HeLa cells, as many RB molecules may still be complexed with SWCNTs inside cells quenching fluorescence. Thus, delivery strategies may be best optimized using a combination of SWCNT uptake and cellular proteolytic activity to achieve the desired selectivity or intracellular release kinetics that best suit the intended treatment. Furthermore, using the release of RB or other quenched molecules as

an intracellular fluorescence reporter may be useful to study cellular processing dynamics in real time with imaging.

6.3.6 SWCNT Ternary Complexes Deliver Bioactive Molecules Inside Cells Increasing Therapeutic Efficiency

Our ternary SWCNT-BSA-RB complex increased the delivery of RB to both HeLa cells and macrophages and facilitated localized intracellular release. To design a therapeutic delivery system, we considered bioactive hydrophobic molecules with similar physical characteristics. Since HeLa cells and macrophages readily internalize millions of SWCNTs-BSA, we selected drugs for modulating cancer and inflammation. Using similar methods to RB, we loaded daunomycin (DM), an anthracycline topoisomerase inhibitor effective as a chemotherapeutic, and prednisone (PRD) or prednisolone (PSL), corticosteroids particularly effective as immunosuppressant drugs, onto SWCNTs using BSA. We carried out a sedimentation, washing, and re-dispersion sequence to remove unbound drugs from SWCNTs before determining the loaded concentration. For DM, we measured the absorbance height above SWCNTs-BSA baseline similar to RB. For PRD and PSL which absorb in the UV where SWCNT baseline absorbance is also high, we quantified the amount of unbound drug to determine loaded concentrations (see Methods). We calculated loadings of 42 ± 23 DM per SWCNT, 35 ± 8 PRD per SWCNT, and 97 ± 25 PSL per SWCNT, which were similar to SWCNTs-BSA-RB

We exposed HeLa cells to 1 μg/mL SWCNTs-BSA-DM for 48 h. Using widefield fluorescence imaging we examined the subcellular distribution of both SWCNTs and DM. SWCNTs primarily localized to the perinuclear region in cells, while DM clearly separated from SWCNTs and localized within the nucleus (Figure 6.7). Since DM was delivered to the nucleus where it is known to intercalate DNA and interfere with DNA replication, we further quantified the resulting cellular effects by examining proliferation. To assess the efficiency of SWCNT ternary complex based DM delivery, we also compared cells treated with only DM or BSA-DM at the equivalent concentration of DM loaded onto SWCNTs. At these concentrations, DM and BSA-DM reduced HeLa cell proliferation by 40 – 45%. For SWCNTs-BSA-DM we observed an even greater anti-proliferative effect further reducing proliferation by 60% which represented a significant 30% enhancement in effectiveness.

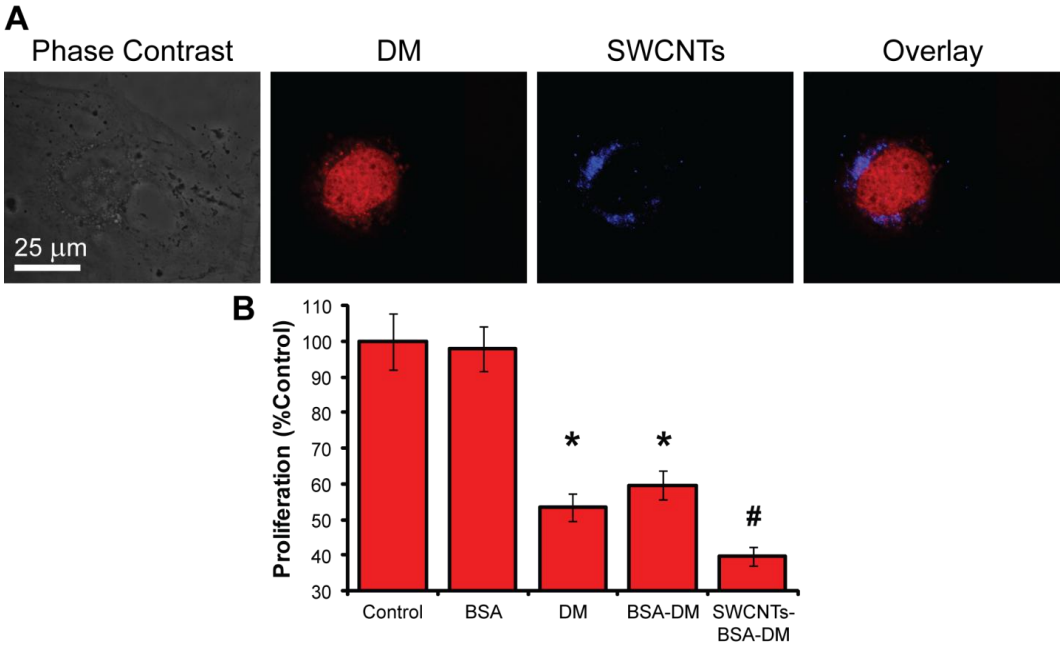

Figure 6.7: Fluorescence imaging of DM and SWCNT localization and quantification of cellular effects in HeLa cells after 48 h exposure to SWCNTs-BSA-DM. (A) NIR fluorescence imaging overlays of SWCNT NIR fluorescence with DM fluorescence shows SWCNTs localize to the perinuclear region while DM separates from SWCNTs and translocates into the nucleus. (B) Exposure to 1 μg/mL SWCNTs-BSA-DM for 48 h significantly enhanced anti-proliferative effects of DM compared to equivalent concentrations of loaded DM alone or with BSA. Data = mean ± SEM, *$p < 0.001$ compared to control, $^{\#}p < 0.001$ compared to DM and BSA-DM.

We also exposed macrophages to 1 μg/mL SWCNTs-BSA-PRD and SWCNTs-BSA-PSL for 48 h alongside equal concentrations of PRD and PSL either alone or complexed with BSA. Based on calculations of PRD or PSL loading, 1 μg/mL SWCNTs corresponded to ~16 nM PRD or ~45 nM PSL which were on the lower end of typical *in vitro* exposure ranges used to represent clinical dosage values.[53] We also treated cells with 1 μg/mL SWCNTs-BSA or equivalent 1 wt% BSA solution as controls. After 46 h, we replaced treatment media with fresh media, and cells were challenged by inflammatory

lipopolysaccharide (LPS) stimulation at 1 μg/mL for 16 h. LPS binds to toll-like receptors on the surface of macrophages which triggers interactions with adapter proteins in the cytoplasm including MyD88, initiating translocation of NF-κB to the nucleus and subsequent expression of inflammatory cytokines.[54] We harvested the cells and quantified the relative amounts of intracellular inflammatory proteins MyD88, NF-κB, and characteristic inflammatory cytokines TNF-α, IL-1β, and IL-6 using multicolor flow cytometry (Figure 6.8). We compared the cellular response using the geometric mean fluorescence intensities (GMFIs) of the labeled proteins within each treatment group in the form of a stimulation index (SI): SI = (GMFI treatment sample)/(GMFI untreated control sample). In general, all treatments resulted in a reduction of the SI for most inflammatory markers, however we observed a high degree of variability in the magnitude of the reductions between different markers. We saw the most consistent cellular responses with IL-1β and MyD88 where treatment with SWCNTs-BSA-PSL significantly lowered the SI below treatments with SWCNTs-BSA, PSL, or BSA-PSL alone. SWCNTs-BSA-PRD treatment with lower drug loading also significantly reduced IL-1β SI compared to controls and showed similar trends for MyD88 although it did not reduce the SI below SWCNTs-BSA control. SWCNTs-BSA-PSL also showed favorable reductions of the SI for NF-κB and IL-6 compared to PSL and BSA-PSL only, but similarly not below SWCNTs-BSA controls. TNF-α SIs were slightly reduced but not below BSA or SWCNTs-BSA controls. The inconsistency with TNF-α, may be the result of variable states

of cell activation as we observed a bimodal population of untreated control cells with high and low GMFIs after LPS activation. We further note that BSA only treatments at the dispersant concentration appeared to consistently reduce SI for all inflammatory markers. This effect was enhanced by SWCNTs-BSA, suggesting that cellular interaction with BSA or internalization of many SWCNTs coated with BSA may have some passivating effect on the inflammatory response of cells.

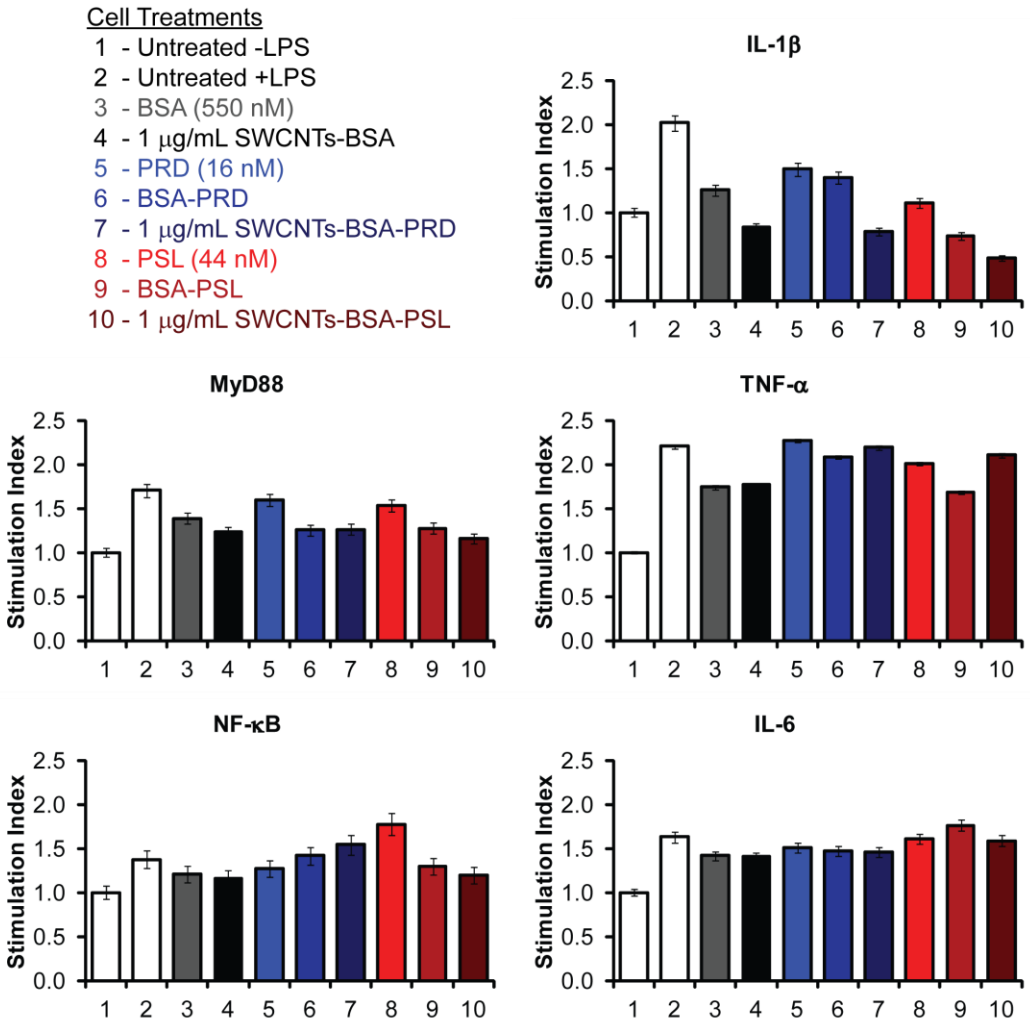

Figure 6.8: Suppression of macrophage intracellular inflammatory proteins and cytokines in response to delivery of anti-inflammatory drugs with SWCNTs-BSA-PRD and SWCNTs-BSA-PSL ternary complexes. The GMFIs of treatment groups were normalized by the GMFI of the untreated control without LPS to generate the stimulation index (SI). SWCNT ternary complex dispersions lower the SI for MyD88 and IL-1β more than BSA-drug or drug alone. Other markers show less effect for SWCNT ternary complex dispersions than SWCNTs-BSA without drugs. Data = mean ± SD for a single culture of J774A.1 macrophages. All treatment populations were statistically different from the untreated control determined by Kolmogorov-Smirnov (K-S) and chi-square probability binning comparison algorithms.

We found that different drugs DM, PRD, and PSL had similar loadings compared to RB of ~40 molecules per SWCNT, suggesting a similar mechanism

of loading onto SWCNTs *via* BSA. Thus, BSA based ternary complex formation between SWCNTs and drugs may be easily extended to other molecules and combinations that share the general characteristics that promote binding within BSA pockets. The molecular loading corresponded to weight ratios of ~0.06:1 – 0.16:1 between drugs and SWCNTs, which were expectedly much lower than values as high as 4:1 for π-stacking of doxorubicin covering ~70 – 80% of SWCNT surface area.[13] For other adsorbing systems, ratios in the range of 0.35:1 – 0.54:1 were determined for PSL on oxidized single wall carbon nanohorns.[55] For our ternary complex system, drug loading scaled with the stoichiometry of drug-BSA binding and the fractional surface coverage of each large BSA protein adsorbed to SWCNTs. However, BSA performs several important functions: (1) BSA entraps drugs preventing their recognition, degradation, and non-specific release in the bloodstream; (2) BSA promotes uptake of SWCNTs in highly metabolic cells including tumor cells and inflammatory immune cells; (3) BSA facilitates intracellular release at cell-specific rates based on lysosomal protein digestive activity.

For cancer treatments, the high cellular uptake of SWCNTs combined with the long (> 48 h) timescales observed for RB release from the ternary complex may find additional utility for overcoming the action of P-gylcoprotein efflux pumps in multidrug resistance cells.[56] For immunomodulation, the suppression of IL-1β has wide ranging implications in the regulation of inflammatory processes and the treatment of autoinflammatory diseases. In contrast to autoimmune diseases where T-cells are largely responsible for

detrimental inflammatory responses, in autoinflammatory diseases, macrophages are the driving force of inflammation which is primarily mediated by increased secretion of IL-1β.[57] The effectiveness of IL-1β blockers in treating other more common diseases including rheumatoid arthritis, gout, and type 2 diabetes suggests further avenues for SWCNT-based IL-1β modulation.[58] Given the preferential uptake into inflammatory macrophages and upstream effects on MyD88, highly loaded SWCNT ternary complexes may find a diverse role improving the specificity and effectiveness of corticosteroid treatments.

6.4 Conclusions

We developed a ternary complex between polycyclic aromatic molecules, BSA, and SWCNTs through all non-covalent interactions for controlled cellular delivery. Our approach is extendable to any molecules or combinations that fit within albumin pockets. We demonstrated albumin proteins could bind relevant molecules and load them onto SWCNTs though non-covalent interactions creating excellent dispersions that maintain inherent properties for multimodal applications. We further found that high SWCNT uptake increased the delivery of loaded molecules, while cell type specific enzymatic processes promoted intracellular release from SWCNTs over 24 – 72 h. The non-covalent ternary complex delivery system was easily modified to deliver chemotherapeutics which inhibited HeLa proliferation and immunotherapeutics which suppressed the production of a subset of macrophage inflammatory cytokines more effectively

than equivalent doses of non-complexed drug. Here, we took non-specific molecules or drugs and through complexation with BSA and SWCNTs provided ways to control the specificity and release with multifunctional SWCNT-protein properties.

6.5 Acknowledgements

I would like to thank Stefanie Baker (Carnegie Mellon University) for assistance with *in vitro* release measurements and Brian Holt (Carnegie Mellon University) for assistance with FLIM measurements. I would also like to thank Hengameh Shams and Prof. Mohammad Mofrad (University of California, Berkeley) for collaboration with BSA-SWCNT complex modeling, as well as Joshua Michel and Prof. Abbe de Vallejo (Children's Hospital of Pittsburgh of UPMC) for collaboration with flow cytometry measurements.

6.6 References

1. Farokhzad, O. C.; Langer, R. Impact of Nanotechnology on Drug Delivery. *ACS Nano* **2009,** *3*, 16-20.

2. Dresselhaus, M. S.; Dresselhaus, G.; Eklund, P. C. *Science of Fullerenes and Carbon Nanotubes*. Academic Press: San Diego, 1996.

3. Kruss, S.; Hilmer, A. J.; Zhang, J.; Reuel, N. F.; Mu, B.; Strano, M. S. Carbon nanotubes as optical biomedical sensors. *Advanced Drug Delivery Reviews* **2013,** *65*, 1933-1950.

4. Robinson, J. T.; Hong, G.; Liang, Y.; Zhang, B.; Yaghi, O. K.; Dai, H. In Vivo Fluorescence Imaging in the Second Near-Infrared Window with Long Circulating Carbon Nanotubes Capable of Ultrahigh Tumor Uptake. *Journal of the American Chemical Society* **2012,** *134*, 10664-10669.

5. Kosuge, H.; Sherlock, S. P.; Kitagawa, T.; Dash, R.; Robinson, J. T.; Dai, H.; McConnell, M. V. Near Infrared Imaging and Photothermal Ablation of Vascular Inflammation Using Single-Walled Carbon Nanotubes. *Journal of the American Heart Association* **2012,** *1*, e002568.

6. Kaiser, J.-P.; Wick, P.; Manser, P.; Spohn, P.; Bruinink, A. Single walled carbon nanotubes (SWCNT) affect cell physiology and cell architecture. *Journal of Materials Science: Materials in Medicine* **2008,** *19*, 1523-1527.

7. O'Connell, M. J.; Bachilo, S. M.; Huffman, C. B.; Moore, V. C.; Strano, M. S.; Haroz, E. H.; Rialon, K. L.; Boul, P. J.; Noon, W. H.; Kittrell, C.; Ma, J.; Hauge, R. H.; Weisman, R. B.; Smalley, R. E. Band Gap Fluorescence from Individual Single-Walled Carbon Nanotubes. *Science* **2002,** *297*, 593-596.

8. Battigelli, A.; Ménard-Moyon, C.; Da Ros, T.; Prato, M.; Bianco, A. Endowing carbon nanotubes with biological and biomedical properties by chemical modifications. *Advanced Drug Delivery Reviews* **2013,** *65*, 1899-1920.

9. Wong, B. S.; Yoong, S. L.; Jagusiak, A.; Panczyk, T.; Ho, H. K.; Ang, W. H.; Pastorin, G. Carbon nanotubes for delivery of small molecule drugs. *Advanced Drug Delivery Reviews* **2013,** *65*, 1964-2015.

10. Bekyarova, E.; Sarkar, S.; Wang, F.; Itkis, M. E.; Kalinina, I.; Tian, X.; Haddon, R. C. Effect of Covalent Chemistry on the Electronic Structure and Properties of Carbon Nanotubes and Graphene. *Accounts of Chemical Research* **2012,** *46*, 65-76.

11. Adeli, M.; Soleyman, R.; Beiranvand, Z.; Madani, F. Carbon nanotubes in cancer therapy: a more precise look at the role of carbon nanotube-polymer interactions. *Chemical Society Reviews* **2013,** *42*, 5231-5256.

12. Calvaresi, M.; Zerbetto, F. The Devil and Holy Water: Protein and Carbon Nanotube Hybrids. *Accounts of Chemical Research* **2013,** *46*, 2454-2463.

13. Liu, Z.; Sun, X.; Nakayama-Ratchford, N.; Dai, H. Supramolecular Chemistry on Water-Soluble Carbon Nanotubes for Drug Loading and Delivery. *ACS Nano* **2007,** *1*, 50-56.

14. He, X. M.; Carter, D. C. Atomic structure and chemistry of human serum albumin. *Nature* **1992,** *358*, 209-215.

15. Ghuman, J.; Zunszain, P. A.; Petitpas, I.; Bhattacharya, A. A.; Otagiri, M.; Curry, S. Structural Basis of the Drug-binding Specificity of Human Serum Albumin. *Journal of Molecular Biology* **2005,** *353*, 38-52.

16. Kratz, F. Albumin as a drug carrier: Design of prodrugs, drug conjugates and nanoparticles. *Journal of Controlled Release* **2008,** *132*, 171-183.

17. Elsadek, B.; Kratz, F. Impact of albumin on drug delivery — New applications on the horizon. *Journal of Controlled Release* **2012,** *157*, 4-28.

18. Holt, B. D.; Dahl, K. N.; Islam, M. F. Quantification of Uptake and Localization of Bovine Serum Albumin-Stabilized Single-Wall Carbon Nanotubes in Different Human Cell Types. *Small* **2011,** *7*, 2348-2355.

19. Boyer, P. D.; Holt, B. D.; Islam, M. F.; Dahl, K. N. Decoding membrane- versus receptor-mediated delivery of single-walled carbon nanotubes into macrophages using modifications of nanotube surface coatings and cell activity. *Soft Matter* **2013,** *9*, 758-764.

20. Duhovny, D.; Nussinov, R.; Wolfson, H. Efficient Unbound Docking of Rigid Molecules. In *Algorithms in Bioinformatics*, Guigó, R.; Gusfield, D., Eds. Springer Berlin Heidelberg: 2002; Vol. 2452, pp 185-200.

21. Schneidman-Duhovny, D.; Inbar, Y.; Nussinov, R.; Wolfson, H. J. PatchDock and SymmDock: servers for rigid and symmetric docking. *Nucleic Acids Research* **2005,** *33*, W363-W367.

22. Andrusier, N.; Nussinov, R.; Wolfson, H. J. FireDock: Fast interaction refinement in molecular docking. *Proteins: Structure, Function, and Bioinformatics* **2007,** *69*, 139-159.

23. Mashiach, E.; Schneidman-Duhovny, D.; Andrusier, N.; Nussinov, R.; Wolfson, H. J. FireDock: a web server for fast interaction refinement in molecular docking. *Nucleic Acids Research* **2008,** *36*, W229-W232.

24. Phillips, J. C.; Braun, R.; Wang, W.; Gumbart, J.; Tajkhorshid, E.; Villa, E.; Chipot, C.; Skeel, R. D.; Kalé, L.; Schulten, K. Scalable molecular dynamics with NAMD. *Journal of Computational Chemistry* **2005,** *26*, 1781-1802.

25. MacKerell, A. D.; Banavali, N.; Foloppe, N. Development and current status of the CHARMM force field for nucleic acids. *Biopolymers* **2000,** *56*, 257-265.

26. Nosé, S. A unified formulation of the constant temperature molecular dynamics methods. *The Journal of Chemical Physics* **1984,** *81*, 511-519.

27. Humphrey, W.; Dalke, A.; Schulten, K. VMD: Visual molecular dynamics. *Journal of Molecular Graphics* **1996,** *14*, 33-38.

28. Islam, M. F.; Milkie, D. E.; Torrens, O. N.; Yodh, A. G.; Kikkawa, J. M. Magnetic heterogeneity and alignment of single wall carbon nanotubes. *Physical Review B* **2005,** *71*, 201401.

29. Johnston, D. E.; Islam, M. F.; Yodh, A. G.; Johnson, A. T. Electronic devices based on purified carbon nanotubes grown by high-pressure decomposition of carbon monoxide. *Nature Materials* **2005,** *4*, 589-592.

30. Islam, M. F.; Rojas, E.; Bergey, D. M.; Johnson, A. T.; Yodh, A. G. High Weight Fraction Surfactant Solubilization of Single-Wall Carbon Nanotubes in Water. *Nano Letters* **2003,** *3*, 269-273.

31. Arnold, M. S.; Green, A. A.; Hulvat, J. F.; Stupp, S. I.; Hersam, M. C. Sorting carbon nanotubes by electronic structure using density differentiation. *Nature Nanotechnology* **2006,** *1*, 60-65.

32. Fagan, J. A.; Becker, M. L.; Chun, J.; Hobbie, E. K. Length Fractionation of Carbon Nanotubes Using Centrifugation. *Advanced Materials* **2008,** *20*, 1609-1613.

33. Becker, M. L.; Fagan, J. A.; Gallant, N. D.; Bauer, B. J.; Bajpai, V.; Hobbie, E. K.; Lacerda, S. H.; Migler, K. B.; Jakupciak, J. P. Length-

Dependent Uptake of DNA-Wrapped Single-Walled Carbon Nanotubes. *Advanced Materials* **2007,** *19*, 939-945.

34. Holt, B. D.; Dahl, K. N.; Islam, M. F. Cells Take up and Recover from Protein-Stabilized Single-Wall Carbon Nanotubes with Two Distinct Rates. *ACS Nano* **2012,** *6*, 3481-3490.

35. Holt, B. D.; McCorry, M. C.; Boyer, P. D.; Dahl, K. N.; Islam, M. F. Not all protein-mediated single-wall carbon nanotube dispersions are equally bioactive. *Nanoscale* **2012,** *4*, 7425-7434.

36. Huang, Y. Y.; Knowles, T. P. J.; Terentjev, E. M. Strength of Nanotubes, Filaments, and Nanowires From Sonication-Induced Scission. *Advanced Materials* **2009,** *21*, 3945-3948.

37. Yaron, P.; Holt, B.; Short, P.; Lösche, M.; Islam, M.; Dahl, K. Single wall carbon nanotubes enter cells by endocytosis and not membrane penetration. *Journal of Nanobiotechnology* **2011,** *9*, 45.

38. Holt, B. D.; Shams, H.; Horst, T. A.; Basu, S.; Rape, A. D.; Wang, Y.-L.; Rohde, G. K.; Mofrad, M. R. K.; Islam, M. F.; Dahl, K. N. Altered Cell Mechanics from the Inside: Dispersed Single Wall Carbon Nanotubes Integrate with and Restructure Actin. *Journal of Functional Biomaterials* **2012,** *3*, 398-417.

39. Duncan, R. R.; Bergmann, A.; Cousin, M. A.; Apps, D. K.; Shipston, M. J. Multi-dimensional time-correlated single photon counting (TCSPC) fluorescence lifetime imaging microscopy (FLIM) to detect FRET in cells. *Journal of Microscopy* **2004,** *215*, 1-12.

40. Köllner, M.; Wolfrum, J. How many photons are necessary for fluorescence-lifetime measurements? *Chemical Physics Letters* **1992,** *200*, 199-204.

41. Becker, W. *The bh TCSPC handbook*. 3rd ed.; Becker & Hickl GmbH: Berlin, Germany, 2008.

42. Cai, H.-H.; Zhong, X.; Yang, P.-H.; Wei, W.; Chen, J.; Cai, J. Probing site-selective binding of rhodamine B to bovine serum albumin. *Colloids and Surfaces A: Physicochemical and Engineering Aspects* **2010,** *372*, 35-40.

43. Shi, J.-h.; Zhu, Y.-Y.; Wang, J.; Chen, J.; Shen, Y.-J. Intermolecular interaction of prednisolone with bovine serum albumin: Spectroscopic and

molecular docking methods. *Spectrochimica Acta Part A: Molecular and Biomolecular Spectroscopy* **2013,** *103*, 287-294.

44. Dresselhaus, M. S.; Dresselhaus, G.; Saito, R.; Jorio, A. Raman spectroscopy of carbon nanotubes. *Physics Reports* **2005,** *409*, 47-99.

45. Heller, D. A.; Barone, P. W.; Swanson, J. P.; Mayrhofer, R. M.; Strano, M. S. Using Raman Spectroscopy to Elucidate the Aggregation State of Single-Walled Carbon Nanotubes. *Journal of Physical Chemistry B* **2004,** *108*, 6905-6909.

46. Bachilo, S. M.; Strano, M. S.; Kittrell, C.; Hauge, R. H.; Smalley, R. E.; Weisman, R. B. Structure-Assigned Optical Spectra of Single-Walled Carbon Nanotubes. *Science* **2002,** *298*, 2361-2366.

47. Koh, B.; Kim, G.; Yoon, H. K.; Park, J. B.; Kopelman, R.; Cheng, W. Fluorophore and Dye-Assisted Dispersion of Carbon Nanotubes in Aqueous Solution. *Langmuir* **2012,** *28*, 11676-11686.

48. Ahmad, A.; Kurkina, T.; Kern, K.; Balasubramanian, K. Applications of the Static Quenching of Rhodamine B by Carbon Nanotubes. *ChemPhysChem* **2009,** *10*, 2251-2255.

49. Tabakman, S. M.; Welsher, K.; Hong, G.; Dai, H. Optical Properties of Single-Walled Carbon Nanotubes Separated in a Density Gradient: Length, Bundling, and Aromatic Stacking Effects. *The Journal of Physical Chemistry C* **2010,** *114*, 19569-19575.

50. Zhu, Z.; Yang, R.; You, M.; Zhang, X.; Wu, Y.; Tan, W. Single-walled carbon nanotube as an effective quencher. *Analytical and Bioanalytical Chemistry* **2010,** *396*, 73-83.

51. Kubin, R. F.; Fletcher, A. N. Fluorescence quantum yields of some rhodamine dyes. *Journal of Luminescence* **1982,** *27*, 455-462.

52. Berezin, M. Y.; Achilefu, S. Fluorescence Lifetime Measurements and Biological Imaging. *Chemical Reviews* **2010,** *110*, 2641-2684.

53. Auret, J.; Abrahams, A.; Prince, S.; Heckmann, J. M. The effects of prednisone and steroid-sparing agents on decay accelerating factor (CD55) expression: Implications in myasthenia gravis. *Neuromuscular Disorders* **2014,** *24*, 499-508.

54. Newton, K.; Dixit, V. M. Signaling in Innate Immunity and Inflammation. *Cold Spring Harbor Perspectives in Biology* **2012,** *4*, a006049.

55. Nakamura, M.; Tahara, Y.; Ikehara, Y.; Murakami, T.; Tsuchida, K.; Iijima, S.; Waga, I.; Yudasaka, M. Single-walled carbon nanohorns as drug carriers: adsorption of prednisolone and anti-inflammatory effects on arthritis. *Nanotechnology* **2011,** *22*.

56. Li, R.; Wu, R. a.; Zhao, L.; Wu, M.; Yang, L.; Zou, H. P-Glycoprotein Antibody Functionalized Carbon Nanotube Overcomes the Multidrug Resistance of Human Leukemia Cells. *ACS Nano* **2010,** *4*, 1399-1408.

57. Dinarello, C. A. Interleukin-1 in the pathogenesis and treatment of inflammatory diseases. *Blood* **2011,** *117*, 3720-3732.

58. Dinarello, C. A.; Simon, A.; van der Meer, J. W. M. Treating inflammation by blocking interleukin-1 in a broad spectrum of diseases. *Nature Reviews Drug Discovery* **2012,** *11*, 633-652.

7 Conclusions and Future Outlook

7.1 Summary

The delivery of single wall carbon nanotubes (SWCNTs) to immune cells, including macrophages, presents tremendous opportunities to leverage the unique properties of SWCNTs for diagnosis and development of therapies related to inflammation, cancer, and regenerative medicine. Interfacing SWCNTs with cells requires functionalization to promote biocompatibility and maintain SWCNT properties. Specific cellular and subcellular applications further demand SWCNT dispersions with additional biofunctionality to control delivery and incorporate application modalities. To impart biofunctionality we considered surfactant-like proteins with structures well-suited for individually dispersing SWCNTs and associating with other biomolecules. The work presented in this thesis utilizes non-covalent protein functionalization of SWCNTs to promote cellular uptake in macrophages and to enable subcellular targeting and drug delivery within cells through structural features of proteins and cellular processing of SWCNT-protein complexes.

We first studied the impact of protein functionalization on SWCNT uptake and cellular processing in macrophages. We investigated the contribution of protein bioactivity and inflammatory activity to SWCNT uptake in macrophages. We also examined the subcellular distribution and aggregation state of SWCNT-protein complexes in macrophages taken up through different internalization mechanisms. Using Raman spectroscopy to uniquely identify and characterize

SWCNTs in cells, we quantified high cellular uptake of SWCNT-protein complexes resulting from macrophage specific subcellular processing.

Based on an initial understanding of the cellular uptake and processing of SWCNT-protein complexes, we further engineered SWCNT-protein complexes with tailored functionalities for subcellular targeting and delivery of bioactive molecules while preserving inherent SWCNT optical properties for multimodal applications. Using SWCNT near-infrared (NIR) fluorescence and fluorescence lifetime imaging microscopy, we characterized the subcellular translocations of targeted SWCNTs and the intracellular release of molecules. Overall, this thesis demonstrates that SWCNT-protein complexes are advantageous for immune cell delivery and modulation of the immune response towards applications in small molecule delivery for cellular reprogramming and antigen delivery for vaccine production.

7.2 Effects of Surface Coating Bioactivity and Macrophage Inflammatory Activity on SWCNT Uptake

In Chapter 3, we determined the contributions of SWCNT-protein complex bioactivity and cell inflammatory activity to levels of SWCNT uptake in macrophages. Internalized SWCNT concentration per cell was precisely quantified using Raman spectroscopy. These uptake measurements were then used to create a quantitative uptake model where parameters were extracted to determine the relative contributions of different SWCNT interfaces and the

cellular inflammatory response to SWCNT uptake. Simply by varying the SWCNT surface coating using non-covalent functionalization with bioactive protein or bioinert copolymer, we were able to provide quantitative uptake parameters for membrane- and receptor-mediated uptake. The uptake of SWCNT-protein complexes was enhanced ~2-fold compared to SWCNT-polymer complexes due to additional interactions with cell surface receptors. Thus, bioactive SWCNT-protein complexes not only enhanced bulk SWCNT uptake in macrophages but also resulted in altered cell morphology with localized regions of extremely high subcellular SWCNT concentrations, suggesting specific processing of SWCNT-protein complexes. Surprisingly, the inflammatory activity of cells contributed much more to levels of SWCNT uptake with ~7-fold increases compared to non-inflammatory cells. Saturation of the cell surface receptor contributions was observed above 30 μg/mL exposure doses for the inflammatory model, suggesting an optimal window below this concentration for selective delivery to inflammatory macrophages which internalized 10 times more SWCNTs than non-inflammatory macrophages and 100 times more SWCNTs than fibroblasts. The work in this chapter provides new quantitative insights into the mechanisms of inflammatory cell uptake of SWCNTs while also identifying regimes in exposure dosing that provide the best selectively for delivery to macrophages. Further, SWCNTs may be selectively delivered to inflammatory macrophages for applications in imaging, sensing, drug delivery, and thermal ablation.

7.3 Macrophage Specific Subcellular Processing and Bundling of SWCNT-Protein Complexes

In Chapter 4, we examined the subcellular processing of SWCNT-protein complexes that resulted in the extremely high subcellular concentrations observed for macrophages. Detailed subcellular Raman spectroscopy measurements were utilized to quantify intracellular SWCNT concentrations and to determine the relative dispersion state of SWCNTs (individual or bundled) within cells. For macrophages with size dependent uptake mechanisms, different SWCNT lengths were used to probe differential subcellular processing through endocytosis of short SWCNTs (< 200 nm) or phagocytosis of long SWCNTs (> 500 nm). Short SWCNTs-protein complex were found to be concentrated subcellulary into distinct regions where SWCNTs were highly bundled compared to the starting SWCNT-protein dispersion. Bundling was SWCNT length and cell type dependent as long SWCNTs-protein complexes in macrophages and short SWCNTs-protein complexes in fibroblasts did not show the same levels of cellular processing. Increased bundling of SWCNTs combined with a reduction in their NIR fluorescence properties suggested that proteins may be actively removed from SWCNTs inside the cell. Thus, for macrophages, the subcellular processing of short SWCNTs combined with increased protein digestive activity likely results in preferential SWCNT bundling. Furthermore, less bundled SWCNTs were released from fibroblasts to a greater extent than more bundled SWCNTs from macrophages, suggesting that bundling may be one mechanism

that promotes long term persistence of SWCNTs in cells. For macrophages, the retention of SWCNTs without toxicity may promote applications involving macrophages as cell-based carriers of SWCNTs to tumors or regions of inflammation for imaging, sensing, and therapy.

7.4 Subcellular Targeting of SWCNTs Using Engineered Biofunctional Proteins

In Chapter 5, we engineered a biofunctional protein for non-covalent SWCNT dispersion and specific subcellular targeting of SWCNT-protein complexes within cells. The resulting low molecular weight (~22 kDa) globular protein had an immunoglobulin (Ig)-fold with a central hydrophobic core for nanotube association and stabilization and an exposed nuclear localization sequence to promote subcellular targeting to the nucleus. Importantly, the protein maintained intrinsic SWCNT properties through non-covalent dispersion which facilitated unambiguous measurement of subcellular localization using SWCNT optical properties. Translocation to the nucleus was observed over 72 h for the engineered SWCNT-protein complexes but not for nonspecific SWCNT-protein complexes using SWCNT NIR fluorescence. The slow translocation process, despite rapid SWCNT cellular uptake and fast nuclear import rates, suggests cellular processing (including endosomal escape, intracellular trafficking, and recognition for nuclear import) is a rate limiting step for subcellular delivery. The modification of native cellular proteins as non-covalent dispersing agents to

provide specific transport opens new possibilities to utilize both SWCNT and protein properties for multifunctional subcellular targeting applications. Specifically, nuclear targeting may allow for enhanced delivery of anticancer therapies, genetic treatments, or DNA, which in turn will promote the further development of novel cellular therapies.

7.5 Multifunctional Ternary SWCNT-Protein-Molecule Complexes for Enhanced Drug Delivery

In Chapter 6, we used an understanding of the cellular uptake and processing of SWCNT-protein complexes to create a multifunctional system for the delivery of bioactive molecules while maintaining inherent SWCNT properties for multimodal applications. We developed a non-covalent ternary SWCNT-protein-molecule complex through protein interactions with both SWCNTs and molecules to enable loading and controlled cellular delivery. Modeling of the SWCNT-protein complex confirmed proteins associate with SWCNTs and molecules at different sites allowing for complex formation. Small molecules (*e.g.*, fluorophores, drugs) were loaded onto SWCNTs with proteins and delivered at increased concentrations within cells due to the bioactive cellular uptake of SWCNT-protein complexes. Fluorescence lifetime imaging microscopy measurements showed SWCNT-protein vectors facilitated the intracellular release of molecules over time *via* protein degradation. Thus, molecule delivery is a function of both SWCNT uptake and cell-specific processing as macrophages

with higher SWCNT uptake and protein digestive activity than HeLa cells showed enhanced amounts of intracellular molecule delivery and faster subcellular release rates. Delivery was also achieved with chemotherapeutic and immunosuppressive drugs resulting in enhanced anti-proliferative effect on HeLa cells and reduction in a subset of inflammatory cytokines for macrophages, respectively, compared to drug only controls. Thus, multifunctional non-covalent SWCNT-protein ternary complexes are able to maintain SWCNT properties in addition to solubilizing drugs, sequestering their bioactivity until released from the complex, and dramatically increasing the efficiency of drug delivery to cells improving therapeutic effectiveness. The generality and effectiveness of the SWCNT-protein-molecule ternary complex was demonstrated by the delivery of several different molecules including model fluorophores and drugs which may be extended to a myriad of small molecule combinations.

7.6 Future Research

Based on the results of this thesis, there are several avenues of future work that may be pursued. The high uptake of SWCNT-protein complexes into antigen presenting cells, including macrophages and dendritic cells, suggests SWCNT-protein complexes may serve as an effective vector for antigen delivery and related vaccine development.[1-2] SWCNTs already have necessary features including chemical inertness, low toxicity, high uptake, and a high surface area for functionalization with many antigen epitopes. SWCNTs may also serve as self adjuvants to stimulate a robust immune response to the delivered antigen. Initial

work in the area has used SWCNTs to deliver weakly immunogenic peptides derived from viruses;[3] peptide and protein lysates from tumors;[4-5] purified protein derivative from bacteria;[6] and low molecular weight molecules.[7]

Another area of potential investigation based on the high uptake and retention of SWCNTs in macrophages is using cells to transport SWCNTs to different tissues in the body. There is a growing interest in using immune cells as cell delivery agents as they readily localize to regions of interest in the body including regions of infection, inflammation, and wound healing, as well as in pathological regions including tumor environments and regions of atherosclerosis.[8] Specifically, monocytes and macrophages are recruited deep inside hypoxic regions of tumors to aid in the establishment of new vasculature. Additionally, immune cells are known to cross the blood-brain barrier and are capable of acting as "Trojan horses" for the delivery of nanomaterials to this notoriously difficult to target region in the body. Strategies have been successful *in vitro* using photothermal ablation of macrophages carrying gold nanoshells to breast cancer tumor spheroids[9] or Glioma spheroids.[10] However, thermal ablation strategies with SWCNTs require less laser intensity and radiation time than therapies with nanoshells.[11] It would be of fundamental interest to characterize the ability of SWCNT-laden macrophages to undergo chemotaxis or extravasation through tissue.

7.7 Conclusion and Outlook

In conclusion, this thesis focused on understanding the macrophage cellular response to SWCNT-protein complexes and engineering the SWCNT-protein complex interface to build new functionalities that preserved inherent SWCNT properties while enabling targeting and delivery applications. The scientific discoveries reveal important details about macrophage uptake and processing of SWCNTs that may be used to probe cell behavior or develop delivery approaches for therapeutic applications. The strategy developed to create excellent SWCNT dispersions with tailored functionalities for subcellular targeting and delivery of bioactive molecules through protein modifications may be used generally by other researchers to initiate new ways to modulate cellular response with nanomaterials.

7.8 References

1. Scheinberg, D. A.; McDevitt, M. R.; Dao, T.; Mulvey, J. J.; Feinberg, E.; Alidori, S. Carbon nanotubes as vaccine scaffolds. *Advanced Drug Delivery Reviews* **2013,** *65*, 2016-2022.

2. Gottardi, R.; Douradinha, B. Carbon nanotubes as a novel tool for vaccination against infectious diseases and cancer. *Journal of Nanobiotechnology* **2013,** *11*.

3. Pantarotto, D.; Partidos, C. D.; Hoebeke, J.; Brown, F.; Kramer, E.; Briand, J.-P.; Muller, S.; Prato, M.; Bianco, A. Immunization with Peptide-Functionalized Carbon Nanotubes Enhances Virus-Specific Neutralizing Antibody Responses. *Chemistry & Biology* **2003,** *10*, 961-966.

4. Meng, J.; Duan, J.; Kong, H.; Li, L.; Wang, C.; Xie, S.; Chen, S.; Gu, N.; Xu, H.; Yang, X.-D. Carbon Nanotubes Conjugated to Tumor Lysate Protein Enhance the Efficacy of an Antitumor Immunotherapy. *Small* **2008,** *4*, 1364-1370.

5. Villa, C. H.; Dao, T.; Ahearn, I.; Fehrenbacher, N.; Casey, E.; Rey, D. A.; Korontsvit, T.; Zakhaleva, V.; Batt, C. A.; Philips, M. R.; Scheinberg, D. A. Single-Walled Carbon Nanotubes Deliver Peptide Antigen into Dendritic Cells and Enhance IgG Responses to Tumor-Associated Antigens. *ACS Nano* **2011,** *5*, 5300-5311.

6. Zeinali, M.; Jammalan, M.; Ardestani, S. K.; Mosaveri, N. Immunological and cytotoxicological characterization of tuberculin purified protein derivative (PPD) conjugated to single-walled carbon nanotubes. *Immunology Letters* **2009,** *126*, 48-53.

7. Parra, J.; Abad-Somovilla, A.; Mercader, J. V.; Taton, T. A.; Abad-Fuentes, A. Carbon nanotube-protein carriers enhance size-dependent self-adjuvant antibody response to haptens. *Journal of Controlled Release* **2013,** *170*, 242-251.

8. Batrakova, E. V.; Gendelman, H. E.; Kabanov, A. V. Cell-mediated drug delivery. *Expert Opinion on Drug Delivery* **2011,** *8*, 415-433.

9. Choi, M.-R.; Stanton-Maxey, K. J.; Stanley, J. K.; Levin, C. S.; Bardhan, R.; Akin, D.; Badve, S.; Sturgis, J.; Robinson, J. P.; Bashir, R.; Halas, N. J.; Clare, S. E. A Cellular Trojan Horse for Delivery of Therapeutic Nanoparticles into Tumors. *Nano Letters* **2007,** *7*, 3759-3765.

10. Madsen, S.; Baek, S.-K.; Makkouk, A.; Krasieva, T.; Hirschberg, H. Macrophages as Cell-Based Delivery Systems for Nanoshells in Photothermal Therapy. *Annals of Biomedical Engineering* **2012,** *40,* 507-515.

11. Kam, N. W. S.; O'Connell, M.; Wisdom, J. A.; Dai, H. Carbon nanotubes as multifunctional biological transporters and near-infrared agents for selective cancer cell destruction. *Proceedings of the National Academy of Sciences of the United States of America* **2005,** *102,* 11600-11605.

Appendix A: Quantification of Single Wall Carbon Nanotube Uptake in Primary Immune Cells

A.1 Methods

A.1.1 Purification of Human Monocytes from Peripherial Blood

Human peripherial buffy coat was obtained from the Central Blood Bank (Green Tree, PA). The buffy coat was transported back to lab and diluted 1:2 with Roswell Park Memorial Institute (RMPI)-1640 media. The resulting suspension was carefully layered on top of Ficoll-Paque PLUS (Ge Healthcare Life Sciences), and spun down at 2000 RPM (IEC Centra-CL2) for 30 min at room temperature. The mononuclear cell layer was gently pipetted off and washed 3 times with RPMI to remove the Ficoll-Paque separation media and residual platelets. Monocytes were purified through negative selection using magnetic beads (Miltenyi Biotech). Non-monocytes were magnetically labeled using a cocktail of biotin-conjugated antibodies with Anti-Biotin MicroBeads. The cell suspension was gravity fed through a magnetic column to extract non-monocytes while the flow-through containing enriched untouched monocytes was collected.

Monocytes were resuspended and cultured in RPMI (20% v/v fetal bovine serum (FBS), 1% v/v penicillin-streptomycin (P/S)) with 100 ng/mL macrophage colony stimulating factor (M-CSF) for 6-8 days to produce macrophages (M0). After 7 days, macrophages were stimulated for 24 h with either 20 ng/mL INF-γ and 100 ng/mL lipopolysaccharide (LPS) to produce pro-inflammatory M1

macrophages or 20 ng/mL IL-4 to produce anti-inflammatory M2 macrophages. ~500,000 cells/well were seeded into 24-well plates pre-coated with serum to limit macrophage activation. Cells were allowed to adhere for 30 min and were then exposed to SWCNTs at the indicated concentration for 48 h. Quantification of SWCNT uptake per cell was performed using Raman spectroscopy of cell lysates after imaging to normalize for cell number, as described in more detail within the main text.

A.1.2 Isolation of Mouse Splenocytes

Excised mouse spleens were macerated and pressed through a cell strainer using the plunger end of a syringe. Cells were washed through the strainer with PBS and the cell suspension was collected and pelleted. Typically splenocytes were pooled from spleens of 2 – 4 mice. Splenocytes were resuspended in red cell lysis buffer for ~2 min. The cell suspension was diluted in PBS and centrifuged to remove red blood cells. Splenocytes were resuspended in Dulbecco's Modified Eagle's Medium (DMEM), supplemented with 10% v/v FBS and 1% v/v P/S. Splenocytes were seeded into 6-well plates at ~10^6 cells/mL

SWCNT Uptake: Splenocytes seeded into 6-well were maintained in culture for 24 h. Subsequently, SWCNTs-BSA was diluted to a final concentration of 1 or 10 μg/mL in fresh media and cells were exposed for 24 h. Afterwards, the media containing SWCNTs was removed. Cells were then gently washed once with PBS. Cells were lifted off of the surface using a cell scraper

and washed 1 time in PBS. Cell suspensions were stained with fluorochrome conjugated antibodies (BD Biosciences) against surface markers F4/80 (to identify macrophages) and CD11c (to identify dendritic cells) for 25 min at room temperature in the dark followed by two washes in PBS and subsequent incubation in cell fixation buffer. Flow cytometry and cell sorting were performed on a FACSAria device (BD Biosciences). Populations of macrophages, dendritic cells, and unlabeled cells (mostly lymphocytes) were collected and pelleted to concentrate cells for further analysis. Quantification of SWCNT uptake per cell was performed using Raman spectroscopy of cell lysates after normalization for cell number, as described in more detail within the main text. Cell number was determined using flow cytometry cell counts of the concentrated post-sorted suspension using a hemocytometer.

Subcellular SWCNT Imaging: For imaging experiments, splenocytes were split into two suspensions for differential cell activation. One suspension was stimulated with 10 ng/mL LPS, while the other was not stimulated. Splenocyte suspensions were seeded directly onto sterilized #1.5 22 × 22 mm glass coverslips which had been functionalized with either poly-L-lysine or fibronectin to promote cell attachment. Cells were allowed to adhere overnight and were maintained in culture for 48 h with one wash step in between to remove non-adhered cells. Afterwards, cells were exposed to 1 μg/mL SWCNTs-BSA diluted in fresh media for 24 h. After 24h, the media containing SWCNTs was removed. Cells were then gently washed three times in PBS and subsequently fixed with 3.7% v/v formaldehyde (Sigma-Aldrich) for 15 min. Confocal Raman spectroscopy

imaging and NIR fluorescence imaging were used to determine SWCNT subcellular localization and concentration, as described in greater detail within the main text.

A.2 Results

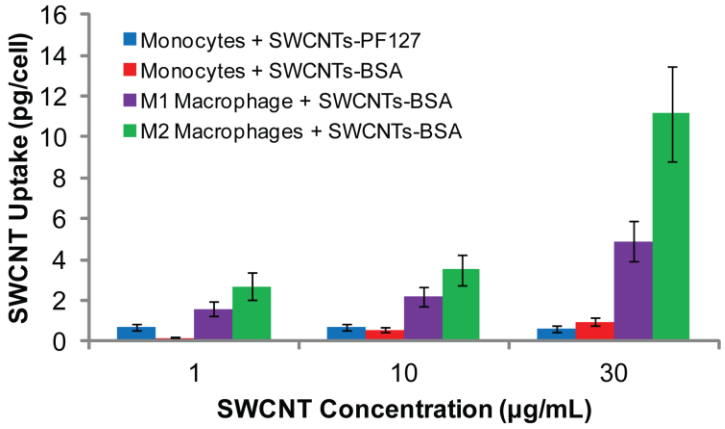

Figure A 1: Preliminary results quantifying SWCNT uptake in primary human monocytes and macrophages. Data = mean ± SD, n = 1 patient. Human monocytes and classically activated (M1; pro-inflammatory) and alternatively activated (M2; anti-inflammatory) monocyte derived macrophages isolated from a single patient's cells. Macrophages show increased SWCNT uptake compared to monocytes, particularly in the M2 phenotype. M2 cell uptake was on average ~11 times greater than monocytes and ~1.9 times greater than M1 cell uptake. We hypothesize that increased M2 uptake is the result of increased nonspecific interaction with scavenger and mannose receptors which are known to be overexpressed in M2 macrophages. J774A.1 cell line uptake values were approximately in between those for M1 and M2. *In collaboration with Dr. Jeremy Kelly and Prof. Stephen Badylak (University of Pittsburgh).

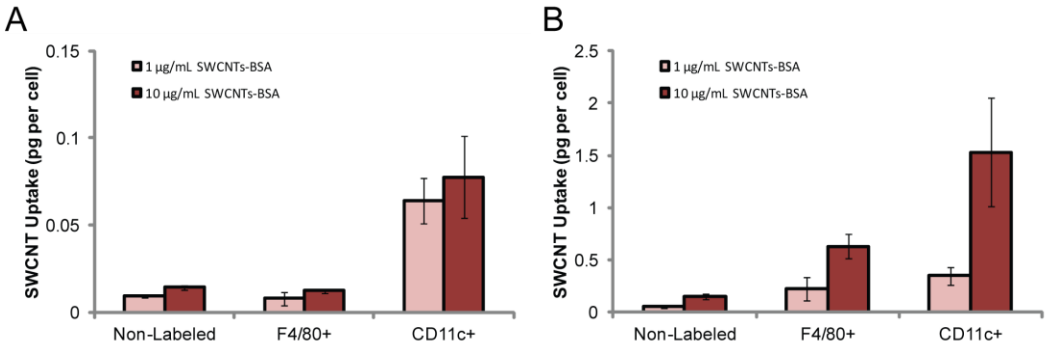

Figure A 2: Preliminary results quantifying SWCNT uptake in cell sorted mouse splenocytes. Mixed mouse splenocytes were labeled with anti-F4/80 for macrophages and anti-CD11c for dendritic cells. (A) Mixed mouse splenocyte uptake was normalized to cell count given from flow cytometry. (B) Mixed mouse splenocyte uptake was normalized to manual cell suspense count after cell sorting. On average just ~10% of flowed cells were detected by manual count afterwards. Data = mean ± uncertainty propagated from Raman spectroscopy measurement and cell count. Non-labeled cells are a mixture of lymphocytes and granulocytes. Dendritic cells show consistently increased uptake compared to macrophages at both concentrations tested. Since dendritic cells are antigen presenting cells, this suggests SWCNTs may show increased effectiveness for antigen delivery or may possess a self adjuvant effect. *In collaboration with Joshua Michel and Prof. Abbe de Vallejo (Children's Hospital of Pittsburgh of UPMC).

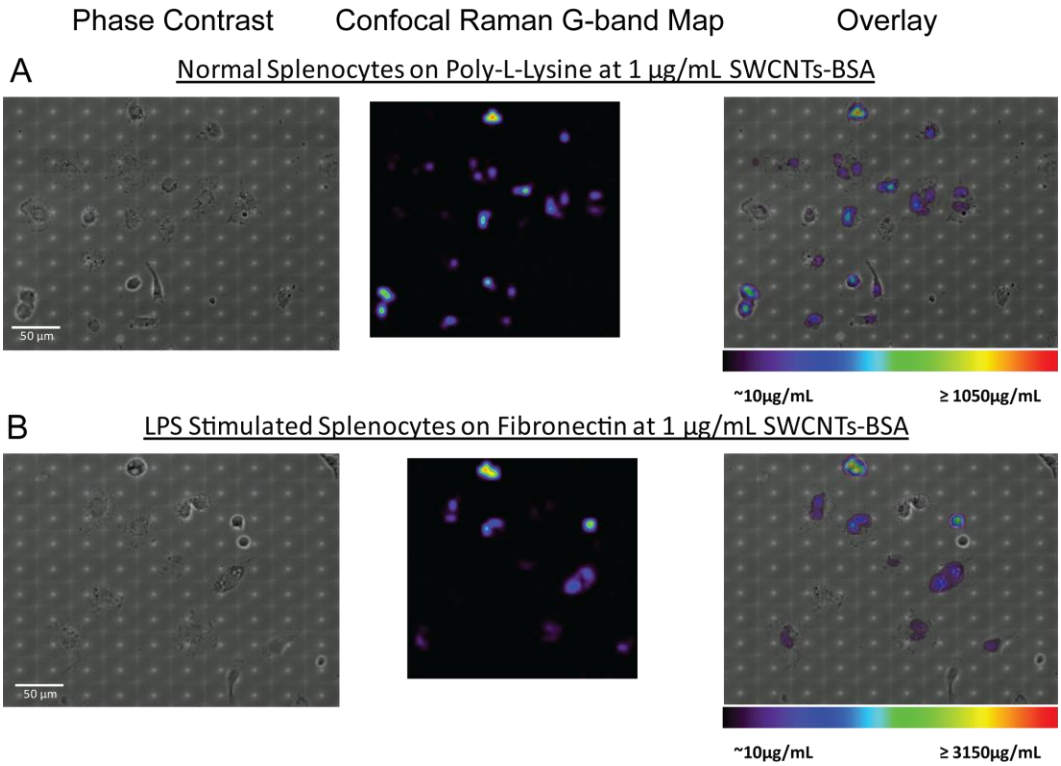

Figure A 3: Confocal Raman maps of mixed mouse splenocytes seeded onto functionalized surfaces exposed to SWCNTs-BSA for 24 h. (A) Mixed mouse splenocytes were seeded onto poly-L-lysine functionalized glass coverslips. SWCNT concentration range shows ~1000-fold increased intracellular concentration compared to the exposure concentration. (B) Mixed mouse splenocytes were seeded onto fibronectin functionalized glass coverslips and stimulated with 10 ng/mL LPS during the experiment. SWCNT concentration range shows ~3-fold increased intracellular concentration compared to non-LPS treatment. Confocal Raman mapping experiments show much higher cell uptake than flow cytometry sorted cells. *In collaboration with Joshua Michel and Prof. Abbe de Vallejo (Children's Hospital of Pittsburgh of UPMC).

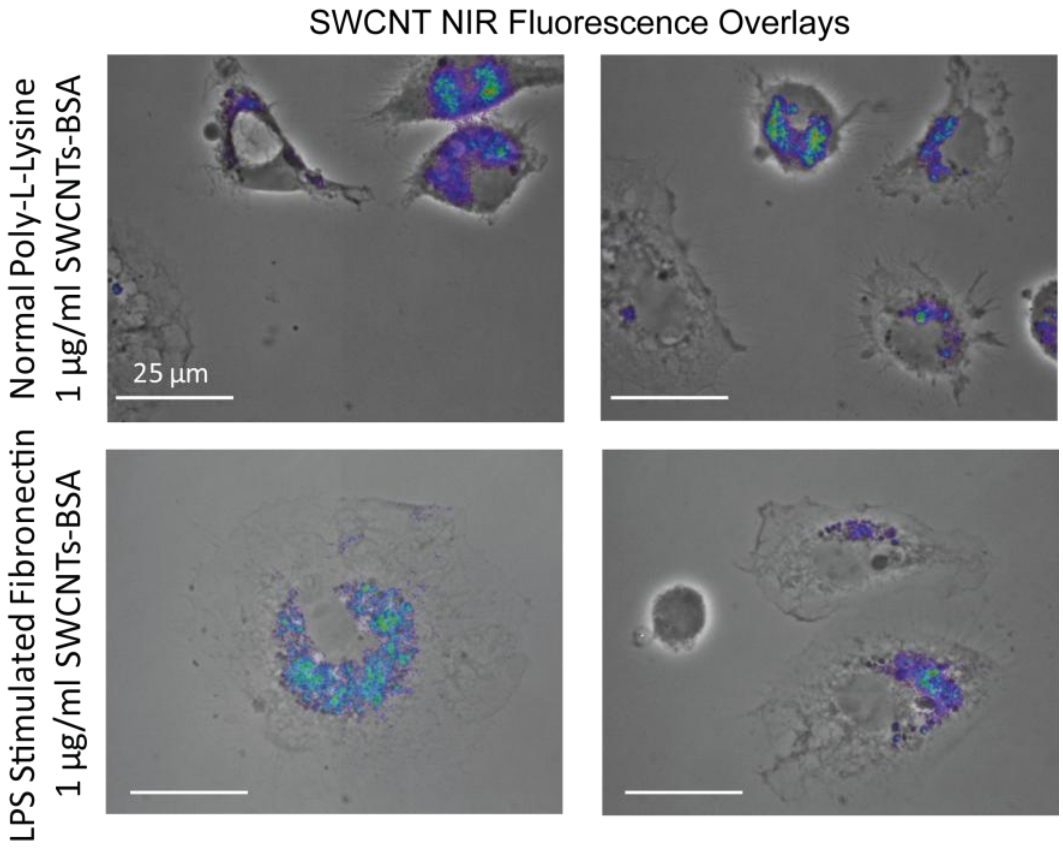

Figure A 4: Widefield NIR fluorescence overlays of SWCNT NIR fluorescence in mixed mouse splenocytes seeded onto functionalized surfaces exposed to SWCNTs-BSA for 24 h. (A) Mixed mouse splenocytes were seeded onto poly-L-lysine functionalized glass coverslips. SWCNT concentration shown as heatmap of NIR fluorescence intensity above noise. (B) Mixed mouse splenocytes were seeded onto fibronectin functionalized glass coverslips and stimulated with 10 ng/mL LPS during the experiment. SWCNT concentration shown as heatmap of NIR fluorescence intensity above noise. *In collaboration with Joshua Michel and Prof. Abbe de Vallejo (Children's Hospital of Pittsburgh of UPMC).

Appendix B: Quantification Single Wall Carbon Nanotubes Uptake Dispersed in Immune Proteins to Target Macrophages

B.1 Methods

B.1.1 Immune Protein SWCNT Dispersions

SWCNT dispersions with PF127 or BSA were prepared according to the main text. Mouse and goat immunoglobulin G (IgG) proteins (~150 kDa) were also used at 10:1 IgG:SWCNT ratios. Fragment crystallizable (Fc) protein domains were used at 4:1 Fc:SWCNT ratio, while lipopolysaccharide (LPS) was used at 5:1 LPS:SWCNT ratio. All dispersions were probe-tip sonicated (Fisher Scientific, Model 100; 3 mm tip diameter) at 6 W and centrifuged at 21,000×*g* for 7 minutes (Beckman Coulter Allegra 25R Centrifuge with a TA-15-1.5 rotor). J774A.1 macrophages were cultured and used as described in the main text. Cells were exposed to SWCNTs in fresh media for 48 h. Quantification of SWCNT uptake per cell was performed using Raman spectroscopy of cell lysates after normalization for cell number, as described in more detail within the main text.

B.2 Results

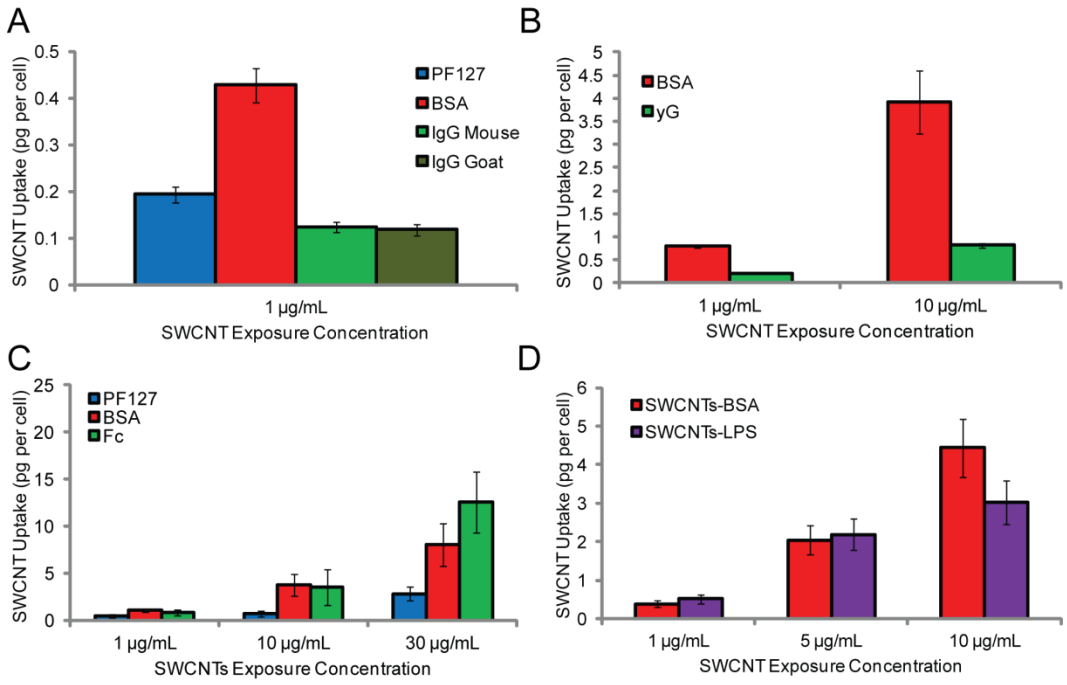

Figure B 1: Quantified SWCNT uptake per cell in J774A.1 after 48 h exposure determined with Raman spectroscopy. (A) Whole immunoglobulin dispersions from both mouse and goat at 1 µg/mL did not significantly enhance uptake relative to BSA (B) Dispersion from mixed γG was not effective at enhancing uptake compared to BSA at 1 or 10 µg/mL. (C) Fc domain dispersions showed a slight increase in SWCNT uptake compared to BSA, but only at 30 µg/mL exposure. (D) SWCNT dispersions directly in LPS had no significant uptake enhancements for 1 – 10 µg/mL.

It appears larger whole immunoglobulin molecules may be forced to interact with the surface of SWCNTs in largely non-preferred orientations for targeting receptors on the cell surface. Fc domains, on the other hand, are smaller and likely able to adopt more arrangements with the SWCNT surface resulting in slightly enhanced uptake but only at high concentrations. For LPS, adsorption of the lipid component to coat SWCNTs may prevent robust interaction with toll-like receptors on the macrophage surface.

Appendix C: Publications and Conference Proceedings Resulting from Thesis

C.1 Publications

5. **P.D. Boyer** *et al.,* "Non-covalent Ternary Dispersions of Single Wall Carbon Nanotubes for Controlled Cellular Delivery," *In Preparation for Submission.*

4. **P.D. Boyer** *et al.,* "Length Selective Delivery and Altered Subcellular Processing of Protein Stabilized Single Wall Carbon Nanotubes in Macrophages," *In Preparation for Submission.*

3. **P.D. Boyer**, S. Ganesh, B.D. Holt, M.F. Islam, K.N. Dahl, "Delivering Single-Wall Carbon Nanotubes to the Nucleus Using Engineered Nuclear Protein Moieties," *In Review* (2015).

2. **P.D. Boyer**, B.D. Holt, M.F. Islam, K.N. Dahl, "Decoding membrane-*versus* receptor-mediated delivery of single-walled carbon nanotubes into macrophages using modifications of nanotube surface coatings and cell activity," *Soft Matter,* 9(3), 758-764 (2013).

1. B.D. Holt, M.C. McCorry, **P.D. Boyer**, K.N. Dahl, M.F. Islam, "Not all protein-mediated single-wall carbon nanotube dispersions are equally bioactive," *Nanoscale,* 4(23), 7425-7434 (2012).

C.2 Conference Proceedings

8. **P.D. Boyer**, S.L. Baker, H. Shams, M.M.K. Mofrad, M.F. Islam, K.N. Dahl, "Non-covalent Dispersions of Single Wall Carbon Nanotubes for Enhanced Drug Delivery to Metabolically Active Cells," *Biomedical Engineering Society*, 2015 Annual Meeting, Tampa, FL, Oct. 2015.

7. **P.D. Boyer**, S. Ganesh, M.F. Islam, K.N. Dahl, "Targeting Single Wall Carbon Nanotubes to the Nucleus using Dispersion with Nuclear Protein Fragments," *American Institute of Chemical Engineers*, 2014 Annual Meeting, Atlanta, GA, Nov. 20, 2014.

6. **P.D. Boyer**, G.Z. Lu, B.D. Holt, M.F. Islam, K.N. Dahl, "Noncovalent Ternary Dispersions of Single Wall Carbon Nanotubes for Controlled Cellular Delivery," *American Institute of Chemical Engineers,* 2014 Annual Meeting, Atlanta, GA, Nov. 19, 2014. (Poster)

5. **P.D. Boyer**, K.N. Dahl, M.F. Islam, "Length Selective Delivery and Altered Subcellular Processing of Protein Stabilized Single Wall Carbon Nanotubes," *American Institute of Chemical Engineers*, 2014 Annual Meeting, Atlanta, GA, Nov. 17, 2014.

4. B.D. Holt, **P.D. Boyer**, K.N. Dahl, M.F. Islam, "Controlling the Single Wall Carbon Nanotube Dispersing Agent for Bioactive Molecule Delivery," *Biomedical Engineering Society*, 2014 Annual Meeting, San Antonio, TX, Oct. 24, 2014.

3. **P.D. Boyer**, B.D. Holt, M.F. Islam, K.N. Dahl, "Increasing Single Wall Carbon Nanotube Delivery to Macrophages by Independent Modifications of the Material and Cellular Activity," *American Institute of Chemical Engineers*, 2012 Annual Meeting, Pittsburgh, PA, Oct. 30, 2012.

2. B.D. Holt, **P.D. Boyer**, K.N. Dahl, M.F. Islam, "Engineering Single Wall Carbon Nanotubes for Sub-Cellular Delivery," *American Institute of Chemical Engineers,* 2012 Annual Meeting, Pittsburgh, PA, Oct. 30, 2012.

1. B.D. Holt, M.C. McCorry, **P.D. Boyer**, K.N. Dahl, M.F. Islam, "Characterizing Protein Single Wall Carbon Nanotubes Dispersions and Rates of Cellular Uptake and Recovery, *American Institute of Chemical Engineers*, 2012 Annual Meeting, Pittsburgh, PA, Oct. 29, 2012.